ABSTRACT

TANNEERU, AKHILESH. Smart ALD Metal-Oxide E-Noses: Designing Low-Power, Highly Sensitive, Selective Gas Sensors. (Under the direction of Veena Misra and Bongmook Lee).

A single wearable platform to continuously monitor our immediate environment as well as the biomarkers from our exhaled breath will lead to a paradigm shift in our personal health care. This would require a gas sensor array or an Electronic-Nose(E-Nose) with high sensitivities and resolutions, to identify these gases in the parts per billion(ppb) range and tell them apart. Challenges that remain to adopt any existing technology are their bulkiness and high power consumptions in several hundreds of milliwatt(mW) range. In overcoming these challenges, this work starts from an efficient single atomic layer deposited(ALD) SnO_2 sensor and builds towards developing a highly sensitive, energy efficient ALD E-Nose.

The sensitivity limits of SnO_2 sensors under a low power consumption are tested against oxidizing and reducing analyte gases. Films with thicknesses in the order of a fraction of Debye length range of SnO_2 are deposited. Sensitivities amplified to over two orders of magnitude and power consumption as low as 30 nW are seen, without an assisted sensor recovery mechanism. Experiments are done to explore assembling an E-Nose with CuO, ZnO and SnO_2-ZnO composites, and the first E-Nose data with discrete sensor components is characterized and evaluated. Over 98% of variance with just two components of PCA is observed from the tests. Additionally, the effects of variables like the sensing layer deposition, annealing and operating temperatures and its mole-fraction, are assessed.

Towards further miniaturizing the form factor and lowering sensor fabrication and assembling costs, a novel idea of a monolithic sensor array is presented. Using the technique of on-chip

annealing, it is shown that the sensor array could now be fabricated on a single silicon wafer eliminating the need of a separate fabrication and assembling process, which as evaluated from COMSOL FEM simulations will bring down the power consumption for the E-Nose to under 10 mW, while also cutting down on the costs associated with assembling discrete sensors into an array. Characterizing the array components against ozone, acetone and humidity is seen to yield over 99.4% of variance with the first three components of PCA. E-Nose performance of a representative few in-house built sensor array components against ozone, acetone, ethanol, toluene, formaldehyde and carbon monoxide is evaluated. Sensors are seen to be reactive at low operating temperatures to the former three target gases while they are seen to be non-reactive with the later three.

Finally the SnO_2 sensors are wirebonded for system level integration with systems designed by collaborating groups and field tested at EPA labs in UNC Chapel Hill, with supporting in-lab characterization wherever necessary. An adaptive current controlled AFE system operating at power of 88.6 nW integrated with a monolithic ALD sensor array - with sensitivities and resolutions in ppb range, itself operating under a total power of 10 mW due to inherent design advantages while also reducing fabrication and assembling costs is determined as the best way forward to meet the desired objective of making a single platform wearable device.

© Copyright 2021 by Akhilesh Tanneeru

All Rights Reserved

Smart ALD Metal-Oxide E-Noses: Designing Low-Power, Highly Sensitive, Selective Gas Sensors

by
Akhilesh Tanneeru

A dissertation submitted to the Graduate Faculty of
North Carolina State University
in partial fulfillment of the
requirements for the Degree of
Doctor of Philosophy

Electrical Engineering

Raleigh, North Carolina
2021

APPROVED BY:

Veena Misra Co-chair of Advisory Committee	Bongmook Lee Co-chair of Advisory Committee
Troy Nagle	Douglas Irving

Ömer Oralkan

BIOGRAPHY

The author was born in Hyderabad, India. From the same place, he picked his bachelors in Electrical and Electronics Engineering in Jawaharlal Nehru Technological University in 2012 and then worked for the software consulting firm, Tata Consultancy Services until June 2014. He then joined NC State University for his master's program and converted to his PhD when he got an opportunity with Dr. Veena Misra's group. During his PhD he worked on AlGaN/GaN wide-band gap semiconductors for almost 18 months and then joined ASSIST team to build semiconductor based gas sensors. Post his PhD, the author would be joining Intel Corporation at Portland, Oregon.

Publications:

1. Agarwala R, Wang P, Tanneeru A, Lee B, Misra V, Calhoun BH. An 88.6 nW ozone pollutant sensing interface IC with a 159 dB dynamic range. InProceedings of the ACM/IEEE International Symposium on Low Power Electronics and Design 2020 Aug 10 (pp. 31-36).

2. Mohaddes F, da Silva RL, Akbulut FP, Zhou Y, Tanneeru A, Lobaton E, Lee B, Misra V. A Pipeline for Adaptive Filtering and Transformation of Noisy Left-Arm ECG to Its Surrogate Chest Signal. Electronics. 2020 May;9(5):866.

3. Azam F, Tanneeru A, Lee B, Misra V. Engineering a unified dielectric solution for AlGaN/GaN MOS-HFET gate and access regions. IEEE Transactions on Electron Devices. 2020 Feb 21;67(3):881-7.

4. Tanneeru A, Akbulut FP, Lee B, Misra V. A novel monolithic array of multiple metal oxide sensors for E-Nose applications via selective on-chip annealing of nanolayered ALD stacks. In2019 IEEE SENSORS 2019 Oct 27 (pp. 1-4). IEEE.

5. Akbulut FP, Lawless K, Tanneeru A, Rao S, Lee B, Misra V. Estimation of Beat-to-Beat Interval from Wearable Photoplethysmography Sensor on Different Measurement Sites During Daily Activities. In2018 IEEE SENSORS 2018 Oct 28 (pp. 1-4). IEEE.

6. Tanneeru A, Lee B, Misra V. Building Blocks of a New ALD E-Nose-A First Step: N-Type and P-Type ALD Sensors. In2018 IEEE SENSORS 2018 Oct 28 (pp. 1-3). IEEE.

7. Tanneeru A, Taylor Z, Lee B, Misra V. Highly Sensitive ALD SnO2 Sensors and the Role of its Thickness in Gas Sensing Capabilities. In2018 IEEE SENSORS 2018 Oct 28 (pp. 1-3). IEEE.

8. Tanneeru A, Lee B, Misra V. ALD and Nanocellulose Based Sensors for Ultra-Low Power, Room Temperature Ozone Gas Monitoring for Respiratory Ailments and Wellness Management, ALD Conference, 2018

9. Tanneeru A, Mills S, Lim M, Mahmud MM, Dieffenderfer J, Bozkurt A, Nagle T, Lee B, Misra V. Room temperature sensing of VOCs by atomic layer deposition of metal oxide. In2016 IEEE SENSORS 2016 (pp. 1-3). IEEE.

Invention Disclosures:

1. Tanneeru A, Lee B, Misra V, Daniele M, 2018, "Conducting metal oxide materials on flexible and stretchable substrates"

2. Tanneeru A, Lee B, Misra V, 2018, "Nano-layered ALD Metal Oxide Electronic-Nose Systems"

ACKNOWLEDGEMENTS

PhD has been a good mix of fun, some hectic and some very hectic phases! Nevertheless, it has become a well-rounded journey opening perspectives which never crossed my path before and leaving much to build on. All along, many people in various forms played integral roles in bringing this work to a finish line, I wish to express my heartfelt thanks to all of them below!

First has been my advisor Dr. Veena Misra by her support and guidance during my PhD that was beyond transactional. Since the beginning, she would always uncomplicate the problems I took to her at a great pace and with a certain quality of gentleness, wisdom to her follow-up questions/suggestions, which were pleasantly devoid of presumptions about us. The outlook and enthusiasm she shared about work made conference deadlines, busy lab days more enjoyable and less stressful. Towards the last leg of my PhD through 2020, it was her especially thoughtful support that was pivotal for this work to reach this point. I feel deeply indebted to her!

Dr. Bongmook Lee has been a very resourceful co-advisor. Over the years I learnt much from him on fabrication, device physics and data analysis. In essence, sessions with him varied in styles and were good in information. His feedback on packing content and story, along with Dr. Misra's take on presentations helped me curate better presentations over time.

My committee members, Dr. Douglas Irving, Dr. Troy Nagle and Dr. Omer Oralkan have all given critical suggestions/directions for this work. Dr. Irving's work on density functional theory, Dr. Nagle's on E-Noses , E-Tongues have fueled inspiration during this work. Dr. Oralkan's gas generation systems along with Dr. Erdem Sennik, Dr. Marzana Mahmud quick trainings have been very helpful to take some time-sensitive measurements.

Collaborations with Dr. Alper Bozkurt, Dr. Michael Daniele, Dr. Shekhar Bhansali, Dr. Ayse

Belger and Dr. Ben Calhoun groups always brought new learnings in various directions.

I will never forget Dr. Rajinder and Linda Khoslas' support in the months leading up to my defense. They have got to be among the coolest old people in town! Dr. Elena Veety was kind to give a great TA experience.

Dr. Faisal Azam and Dr. Narayanan Ramanan patiently explained about all research groups in MRC on my first day on campus. In the years to come I would continue to enjoy my many discussions with Faisal and benefit from his objective viewpoints. I also wish to acknowledge the support of my past and current group members. With Dr. Michael Lim, Kevin Lawless and Dr. Biplab Sarkar, I shared many interesting exchanges. Michael, Dr. Xiangyu Yang, Dr. Steven Mills passed on heavy information on Sputter, ALD, gas testing tools. Special thanks to Sydney Richmond for her hardwork and sincerity in spending countless hours in helping me with sensor characterization. Dr. Farzad Mohaddes aid with PCA during the time-crunch months before my defense deserves special appreciation and Dr. Fatma Akbulut's, in the years before that.

Staff at Nanoelectronic Fabrication Facility (NNF), Analytical Instrumentation Facility (AIF) at NCSU, Shared Materials Instrumentation Facility (SMIF) at Duke University, Chapel Hill Analytical and Nanofabrication Laboratory (CHANL) at UNC Chapel Hill, Dr. Jan Genzer, Yeongun Ko (NCSU) all of whose facilities and tools were crucial for my device fabrications and analytical characterizations. Sincere thanks to Dr. Steve Lipa for all the wire bonds he did for our group.

I would also like to acknowledge National Science Foundation Nanoscience Engineering Research Center for Advanced Self-Powered Systems of Integrated Sensors and Technologies (EEC-1160483) for funding this work.

All the good talks and times with friends made stay at Raleigh pleasurable. I cherished my time with with Vivek Nair, George Mathew, Nandakishore Manoore, Tory Gordon, Shashank Pulimamidi, Amruthkiran Hegde, Mayank Vaish and calls with Uday Goteti, Chaithanya Ammeneni.

I would like to express my gratitude to my uncle Tagore Kalidas for financing my first semester at NC State! Without his generous offer to support, my path would not have been the same. I'm lucky and grateful to have grown up with kind, loving parents and sister. Nothing in me can thank my parents enough for going above and beyond to provide for our educational needs. Prasad's friendship and my nephews' fun adds to the bond with my sister.

TABLE OF CONTENTS

List of Tables . . . . . **ix**

List of Figures . . . . . **x**

Chapter 1 Introduction **1**
1.1 Motivation and Key Requirements 1
1.2 Why an ALD Metal Oxide E-Nose? 2
1.3 Atomic Layer Deposition 7
1.4 Thesis outline 9

Chapter 2 ALD Gas Sensing - Case for a Better MOx Gas Sensing Technology . . **11**
2.1 Room temperature sensing of VOCs with ALD SnO_2 sensor 12
2.1.1 Introduction 12
2.1.2 Experimental Methods 13
2.1.3 Results and Discussion 16
2.1.4 Conclusion 19
2.2 Varying Sensor Thickness 20
2.2.1 Sensor Fabrication 20
2.2.2 Gas Generation and Sensor Testing 21
2.2.3 Thickness Effect - Response to ozone 22
2.3 ALD and nanocellulose - thin film MOx and high surface area substrates 24
2.4 Building Blocks: n-type and p-type MOx sensors 27
2.4.1 Sensor Fabrication 28
2.4.2 Gas Generation and Sensor Testing 29
2.4.3 Response with ozone and acetone 29
2.4.4 Conclusion 35
2.5 Summary 36

Chapter 3 From ALD Sensors to E-nose: Novel Monolithic Sensor Array Platform **37**
3.1 Introduction 38
3.1.1 Experimental Methods 39
3.1.2 Gas Testing Setup 40
3.1.3 Results and Discussion 42
3.2 FEM Design simulations MEMS heater array 49
3.3 Microheater fabrication 71
3.4 Optimization and E-Nose performance of ALD sensors 76
3.5 Optimization of constituent sensors 78
3.6 E-Nose Performance Testing 80
3.6.1 Gas Mixtures - Acetone and Ethanol 82
3.6.2 Interference Tests - Toluene, Formaldehyde and Carbon monoxide . . . 85

3.6.3 Breath Analysis - Acetone and Ethanol . . . 87
3.7 Summary . . . 90

Chapter 4 System Integration and Field Testing . . . 92
4.1 Integration: HET . . . 92
4.1.1 Simulated Field Testing . . . 94
4.2 An 88.6nW Ozone Pollutant Sensing Interface IC with a 159 dB Dynamic Range 96
4.2.1 Introduction . . . 97
4.2.2 System Architecture . . . 100
4.2.3 Resistance Range Tracking . . . 101
4.2.4 Measurement Results . . . 105
4.2.5 Conclusion . . . 109

Chapter 5 Conclusions and Future Work . . . 111
5.1 Conclusions . . . 111
5.1.1 Testing the power and sensitivity limits of ALD SnO_2 sensor . . . 111
5.1.2 Building Blocks of E-Nose with ALD sensing layers . . . 112
5.1.3 Designing a novel monolithic sensor array . . . 113
5.1.4 System Integration . . . 114
5.2 Future Work . . . 115

References . . . 116

APPENDICES . . . 121
Appendix A Estimation of Beat-to-Beat Interval from Wearable Photoplethysmography Sensor on Different Measurement Sites During Daily Activities . . . 122
A.1 Introduction . . . 123
A.2 Method . . . 125
A.3 Results . . . 128
A.4 Conclusion . . . 132
Appendix B Measurement of ECG signal from left-arm . . . 133
B.1 Introduction . . . 133
B.2 Hardware . . . 134
B.3 ECG Data Acquisitions and Conclusions . . . 138

LIST OF TABLES

Table 1.1 Advantages and disadvantages of various sensor technologies [15] [16] [17] 6

Table 3.1 Atomic % values vs anneal condition as obtained from the XPS survey . 43
Table 3.2 List of Silicon material parameters used in simulations 52
Table 3.3 List of Silicon Dioxide material parameters used in simulations 52
Table 3.4 List of Silicon Nitride material parameters used in simulations 53
Table 3.5 List of Platinum material parameters used in simulations 53
Table 3.6 Voltage applied and power consumed to reach 400°C for both microheater designs 70
Table 3.7 Temperature, Voltage and Power numbers comparison for microheater design (a) 71
Table 3.8 Concentrations of gas mixtures used for testing 83

Table 4.1 Performance Summary and State-of-Art Comparison 107

Table A.1 Means and standard deviations of proposed beat-to-beat interval algorithm (b2bint) and empatica's (emp.). hr in bpm and ibi counts (rest position) where fs=64Hz 131
Table A.2 Proposed algorithm (b2bint) and empatica's (emp.) means and standard deviations of mse between ecg and ppg 132

LIST OF FIGURES

Figure 1.1 (a) A commerically available Cyranose 320 handheld chemical vapor sensing E-nose (b) NASA JPL Enose to monitor any chemical analytes (c) Response with two analytes - toluene and benzene, from 16 sensors of a NASA JPL ENose [14][13] 4

Figure 1.2 (a) ENose size envisioned at the beginning of this work - the size of a wrist watch (b) Watch board designed by ASSIST HET Team housing, for physiological health signals [9] 5

Figure 1.3 Typical ALD process using TMA precursor and H_2O oxidant. Hydrogen (blue), carbon (red), aluminum(purple), oxygen (yellow). Figure courtesy of Cambridge Nanotech Inc. 8

Figure 2.1 STEM-EDS image of fabricated sensor device 14

Figure 2.2 Grazing Angle X-ray Diffraction image of film before and after 600°Cpost dielectric anneal 14

Figure 2.3 Gas sensor testing setup with bubbler to produce VOC vapor on the left and Teledyne to produce T700U, along with measurement setup of Keithley-4200SCS on the right. 15

Figure 2.4 Sensor response to acetone when operated at room temperature 17

Figure 2.5 Varying response with repeated exposure of various concentrations of acetone and without any targeted recovery 18

Figure 2.6 Sensor response with humidity alone and humid-acetone with same RH% 18

Figure 2.7 a) Fabricated sensor structure b,c) Cross-sectional TEM images on 12 nm SnO_2 film with 600°CPDA 21

Figure 2.8 Response of 4 nm, 6.5 nm, 12 nm ALD SnO_2 sensing layer with 25 to 100 ppb of dry ozone 22

Figure 2.9 A comparison of the relative response of all three sensors plotted on log scale, where $\Delta R/R\% = (R_{gas} - R_{air})/R_{air} \times 100\%$ 23

Figure 2.10 a) Optical, microscopic and SEM image of nanocellulose before ALD metal oxide deposition b) SEM image of nanocellulose post ALD deposition c) Images demonstrating the flexible nature of nanocellulose . . . 26

Figure 2.11 Response from Si-sensor (w/o PDA) (left) and Nanocellulose sensor(right) with 25 to 100 ppb of Ozone 27

Figure 2.12 Response and first derivative curves of SnO_2 sensor with ozone 31

Figure 2.13 Response and first derivative curves of CuO sensor with ozone 32

Figure 2.14 Peak response of SnO_2 and CuO after 2 mins of exposure at various ozone concentrations 32

Figure 2.15 Peak response of SnO_2 and CuO after 2 mins of exposure at various acetone concentrations 33

Figure 2.16 Peak response of SnO_2 and CuO after 2 mins of exposure at various humidity concentrations 33

Figure 2.17 PCA with ozone and acetone with SnO_2, CuO and ZnO sensors 35

Figure 3.1 Concept of on-chip annealing of sensor surfaces 40
Figure 3.2 First design of a fully fabricated monolithic sensor array 41
Figure 3.3 A 3D waterfall plot of XPS survey spectrum obtained on all the samples. The atomic % values are tabulated in Table 1 43
Figure 3.4 Grazing Incidence X-Ray Diffraction peaks of samples annealed at 600°C, 900°Cand 1200°C, with relevant peaks from metal oxides labelled 44
Figure 3.5 Selected electron microscopy of the SnO_2-ZnO composites across the annealed temperature ranges of RT to 900 °C 44
Figure 3.6 HAADF images at mid-temperature range where the Sn concentration relatively peaks. The intensity counts of elements (b) Sn (c) Zn (d) Si . . 45
Figure 3.7 Room temperature response with ozone from sensor annealed at 600 °C 45
Figure 3.8 Responses with ozone from sensors annealed at various temperatures obtained at an operating temperature of 200 °C 46
Figure 3.9 Responses with acetone from sensors annealed at various temperatures obtained at an operating temperature of 200 °C 47
Figure 3.10 PCA obtained from all composite sensor components with ozone and acetone. 99.4% of variance accounted with first 3 components 48
Figure 3.11 3D view of simulated design with constrictions 53
Figure 3.12 2D view of simulated design with constrictions 54
Figure 3.13 Horizontal and vertical sweeps of heat profiles across the heater strips . 54
Figure 3.14 Design with asymmetrical strips and a just a center constriction with an unetched membrane 56
Figure 3.15 Design with just a center constriction with a rectangular hole etched around the constriction in the membrane 57
Figure 3.16 Design with just a center constriction with a circular hole etched around the constriction in the membrane 58
Figure 3.17 Design with just a center constriction with a circular hole etched around the constriction in the membrane, plus a tapered constriction 59
Figure 3.18 Horizontal and vertical temperature profile sweep across the membrane 60
Figure 3.19 Design with membrane being rectangular sections etched around the entire heater strip, with central constriction 61
Figure 3.20 Design with membrane being rectangular sections etched around the entire heater strip, without central constriction 62
Figure 3.21 Horizontal and vertical temperature profile sweep across the membrane 63
Figure 3.22 Reducing the voltage bias applied to 2.5 V instead of 4 V. The temperature at the center of strip reached upto 900°C as could be seen in 3.23 below 64
Figure 3.23 Horizontal and vertical temperature profile sweep across the membrane of 3.22 65

Figure 3.24 Heating and cooling times for various points across the membrane. The blue line is at the center of constriction on top of heater, green line is for the center of bottom strip and red line is for the center of bottom strip. We can see the heating an cooling times are under 5 ms. 66
Figure 3.25 Reducing the voltage bias applied to 1.4 V instead of 4 V. The temperature at the center of strip reached upto 945°C as could be seen in 3.27 below 67
Figure 3.26 Horizontal and vertical temperature profile sweep across the membrane of 3.25 68
Figure 3.27 Heating and cooling times for various points across the membrane. The blue line is at the center of constriction on top of heater, green line is for the center of bottom strip and red line is for the center of bottom strip. . 69
Figure 3.28 Fig.3.22 & Fig.3.25 have been modified to increase the number of sensors per membrane 70
Figure 3.29 Heater Layer 72
Figure 3.30 Protection Layer 72
Figure 3.31 Etching Mask 73
Figure 3.32 Etching process 73
Figure 3.33 Heater electrode uncover 74
Figure 3.34 Characterization of sensor with microheater 74
Figure 3.35 IR Camera image of microheater 75
Figure 3.36 Design mask showing different heater designs currently being fabricated 76
Figure 3.37 Baseline Resistance vs Anneal Temperature and Sensor Thickness, plotted for an operating temperature of 200°C 78
Figure 3.38 Response vs Operating Temperature and Sensor Thickness, plotted at an ozone conc. of 75 ppb and for all sensors annealed at 300°C 79
Figure 3.39 Gas generation setup for simultaneous multiple gas generation 81
Figure 3.40 Control interface for Fig 3.39 82
Figure 3.41 PCA response of acetone-ethanol gas mixture 84
Figure 3.42 Representative response of sensor SnO_2 (50 cycles - 6 nm) with various concentrations of toluene 85
Figure 3.43 Representative response of CuO sensor (1200 cyles - 40 nm) with various concentrations of formaldehyde 86
Figure 3.44 Representative response of SnO_2 sensor (4 nm, 6.5 nm and 12 nm) with various concentrations of carbon monoxide 87
Figure 3.45 Design mask showing different heater designs currently being fabricated 88
Figure 3.46 Design mask showing different heater designs currently being fabricated 89
Figure 3.47 Design mask showing different heater designs currently being fabricated 90

Figure 4.1 First Generation HET 93
Figure 4.2 Voltage divider circuit designed to read out SnO_2 sensor data 94
Figure 4.3 EPA Labs at UNC Chapel Hill 95

Figure 4.4 Ozone field testing at EPA labs 96
Figure 4.5 R-V conversion of the proposed sensor interface IC, compared to previous gas sensing interfaces [4],[5]. 98
Figure 4.6 Proposed ozone sensing sensor interface IC along with the test setup. . . 99
Figure 4.7 Flowchart of the RRT and associated timing diagram. 102
Figure 4.8 Flowchart of the conversion from resistance to ozone concentration. . . 104
Figure 4.9 Transistor level schematic of the chopper-stabilized differential amplifier. 104
Figure 4.10 Annotated die photo of the proposed sensor interface IC. 106
Figure 4.11 Measured analog output voltage (left) and IDAC current (right) of the sensor interface as a function of resistance (R_{sen}). 107
Figure 4.12 Measured input-referred noise density of the sensor interface. 107
Figure 4.13 Measured resistance change (left) and corresponding O_3 concentration (right) observed by the sensor interface IC for O_3 sensors with thicknesses 6.5nm (a) and 12nm (b). 108
Figure 4.14 Measured sensitivity of the sensor interface IC when tested with O_3 sensors with thicknesses of 6.5 nm (diamond) and 12 nm (circle) across ozone concentrations from 100 ppb to 900 ppb. The R^2 values show the measured concentration linearity when tested with 6.5nm (orange) and 12 nm (red) sensors. 109
Figure 4.15 Comparison to the state of the art showing a 300x power reduction in sensor interfaces for gas sensing. 110

Figure A.1 Characteristic points of PPG with 1st and 2nd derivatives, showing typical time-points of systolic points (sp) at maxima of PPG, maxima of 1st derivative, and diastolic points (dp) at minima of PPG and maxima of 2nd derivative 127
Figure A.2 Measurement site of PPG signal on human body (measured in resting position) 130

Figure B.1 ECG armband (left); arm and chest electrode positions (middle); system hardware (right). 136
Figure B.2 Block diagram of the biometric armband. 137
Figure B.3 ECG signals simultaneously obtained from the chest and left arm. . . . 138

CHAPTER

ONE

INTRODUCTION

1.1 Motivation and Key Requirements

The World Health Organization (WHO) has documented Ozone (O_3), nitrogen dioxide (NO_2), sulfur dioxide (SO_2) to have strong correlation with adverse health effects seen[1]. Many of these gases like NO_2, VOC, and O_3 are emitted as by-products from combustion engines and industrial facilities, while gases like NO_2 also additionally aid O_3 formation with atmospheric oxygen by photocatalysis at ground level[2] [3]. For example with Ozone (O_3), the National Ambient Air Quality Standards (NAAQS) has quantified that expsoures to it, in concentrations as low as 70 ppb for over 8 hours exacerbates COPDs and asthma[4]. Approximately 38 million Americans, or 12% of the population, are affected by either chronic obstructive pulmonary

disease (COPD) or asthma [5].

On the other hand, literature points to an extensive list of biomarkers in our exhaled breath which will allow non-invasive monitoring to detect several health conditions from chronic diseases to life threatening illnesses [6]. For example, the presence of over 80 ppb of formaldehyde in our exhaled breath could give early indications for lung cancer. Similarly people suffering from type II diabetes have exhaled breath concentrations of over 1.8 ppm [6]. Global report on diabetes by WHO in 2016 shows that there are 422 million adults who have diabetes and there are 1.5 million deaths each year who cause could be directly attributed to diabetes [7][8].

The solutions to both the above problems could be addressed by portable, wearable mobile health technology where an integrated platform can be created with sensors that have sensitivities to accurately sense such low concentrations in tens of ppb range and have high resolution so they can quantify the biomarkers to discern the healthy scenarios from the unhealthy ones. Incorporating this technology into self-powered wearables as envisioned by Advanced Self-Powered Systems of Integrated Sensors and Technologies (ASSIST) for a continuous and real-time health monitoring, imposes a critical constraint of making these sensors operational under ultra low power consumption, aspiring to power numbers as low as a few 100 μW to under 5 mW for an array [9].

1.2 Why an ALD Metal Oxide E-Nose?

E-Nose is an array of sensors broadly tuned to respond to a wide catalog of gases, with each sensor not specifically tailored to any one target gas. Inspired by mammalian olfaction where all receptors respond to multiple gas analytes and the brain uses pattern recognition to identify

the nature and strength of the odors, synthetic noses or E-noses are similarly designed to sense gases in the ppb range and have high resolutions with machine learning algorithms helping to recognize the patterns [10] [11][12]. E-Noses have been in use for sensing chemical mixtures that constitute aromas, odors, fragrances, formulations, spills and leaks well used in petrochemical, chemical, food and beverage, packaging materials, medical research industries etc[13][14]. A major roadblock in adopting these sensor arrays to meet our objective comes primarily from the power consumption, size and cost of these devices (Fig.1.1). Typically handheld devices, these have a volume greater than $800cm^3$, and power consumption per sensor in the order of tens of milliwatts, taking the total power consumed by the sensor array/e-nose to hundreds of milliwatts. Also, currently employed fabrication and integration techniques drive the costs of these e-noses to well over $7000 per system. These current form factors, operating conditions and costs far exceed the prerequisites of wearability for long-term, continuous, real-time health monitoring as laid out in the objectives (Fig.1.2).

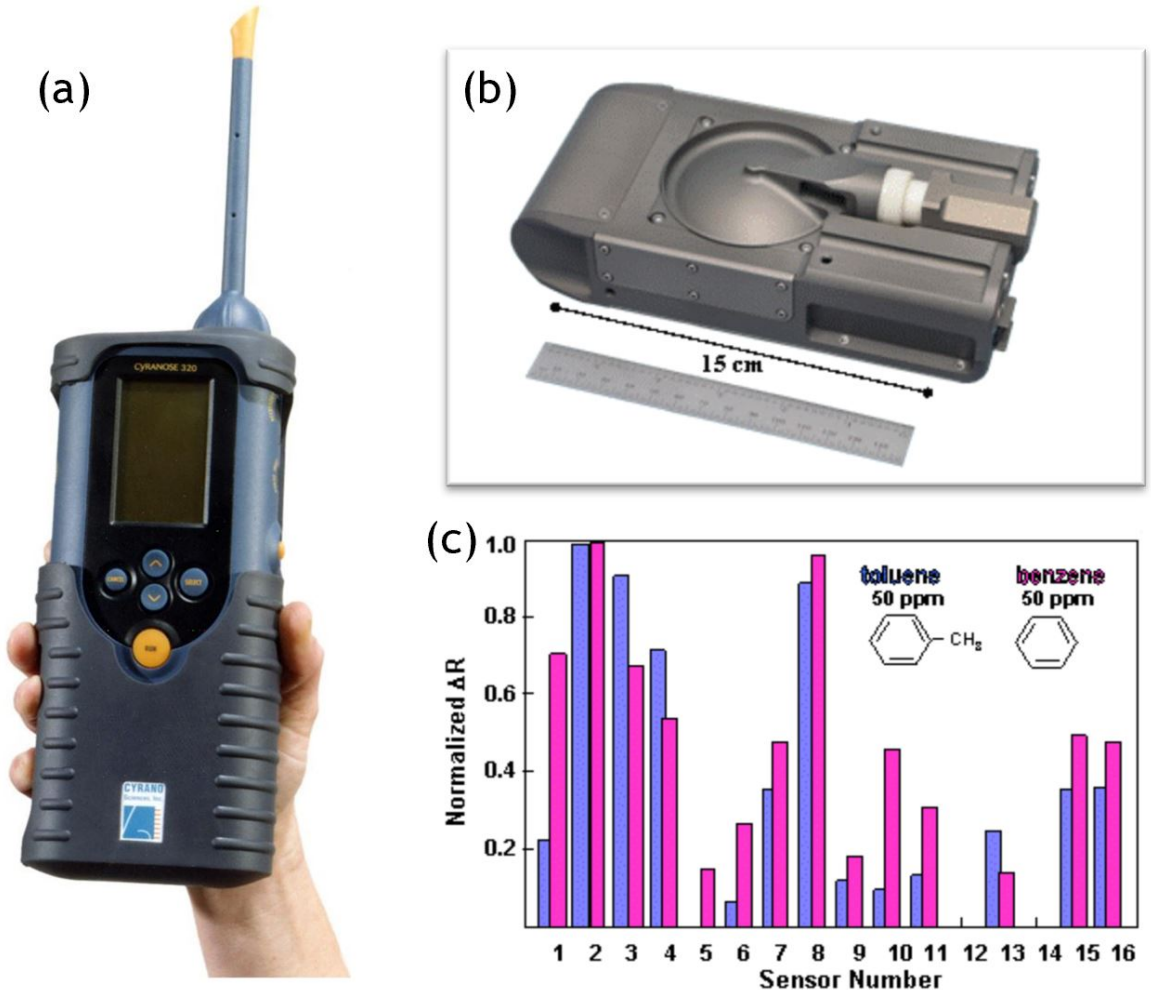

Figure 1.1: (a) A commerically available Cyranose 320 handheld chemical vapor sensing E-nose (b) NASA JPL Enose to monitor any chemical analytes (c) Response with two analytes - toluene and benzene, from 16 sensors of a NASA JPL ENose [14][13]

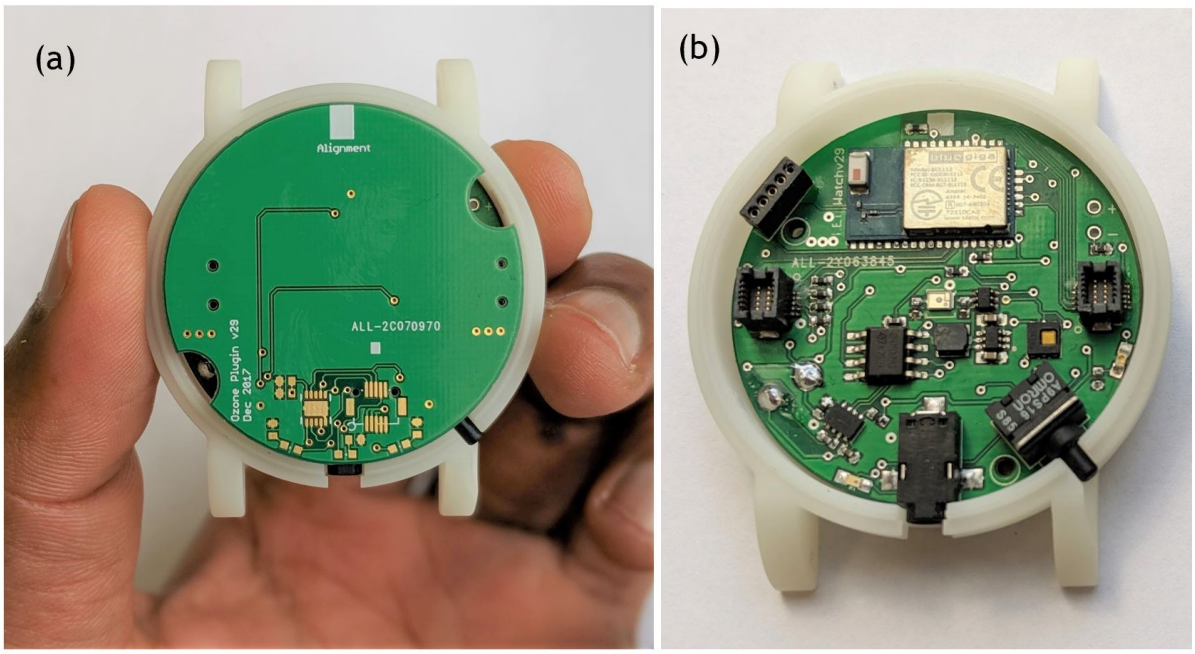

Figure 1.2: (a) ENose size envisioned at the beginning of this work - the size of a wrist watch (b) Watch board designed by ASSIST HET Team housing, for physiological health signals [9]

In order to design an E-Nose overcoming the constraints described before, a survey of the existing sensor technologies, which includes conducting polymers, optical, electrochemical, piezoelectric, and metal oxides, was done. Their advantages and disadvantages are listed in the below table

Electrochemical sensors are highly selective because of the porous membrane that allow gas diffusion. The membrane pore size can control the size of the analyte gas that diffuses through it and start an electrochemical reaction. Then the current in the circuit is correlated to the concentration of the analyte gas. The drawback is electrochemical sensors being usually large making a sensor array bulky and as such usually used in stationary systems. Photonic gas sensors work by emitting specific wavelengths that are absorbed by a gas in their specific bandwidths. By comparing the intensities in the bandwidths to the one outside, the concentration

Table 1.1: Advantages and disadvantages of various sensor technologies [15] [16] [17]

Sensor Type	Advantages	Disadvantages
Polymer based	Room temperature operation Low power High sensitivity Fast response Small size	Lifetime/reliability/reversibility issues Drift/calibration problems Broad selectivity High humidity sensitivity Degrades under UV and ozone exposure
Optical	Very fast response time Room temperature operation Good selectivity	Large size Short lifetime Complex driving circuit and high cost Expensive
Electrochemical	Low power Linear output Good repeatability	Difficult to achieve ppb sensitivity Slower response Poor lifetime/stability
Piezoelectric	High sensitivity Fast response time	Temperature and humidity dependence Variability in sensor coating Difficult to replace sensors
Metal Oxide	High sensitivity Fast response/recovery times Low cost manufacturing Small size Long term stability/lifetime	High temperature (power) operation Broad selectivity Humidity sensitivity

of the gas could be extracted. The active emission of photons make these systems consume very high power making it ineffective to reach our envisioned objective. Polymer based sensors which are widely used have long-term reliability and recovery issues in the presence of ambient humidity [15] [16].

Semiconductor sensors detect gases by their adsorption to its surface. The resistance of the semiconductor sensing layer changes upon gas adsorption due to the charge transfer with the sensing layer or due to a change the electronic structure. While the existing metal oxide (MOx) semiconductor sensors have operating temperatures well above 400°Cwhich increase their operating power budgets to the tens of milliwatt range per sensor, the advanced fabrication technologies that have become available by pushing the limits of Moore's law, can

allow miniaturization, low temperature and thereby low power operation with the appropriate innovations [18] [19]. One such tool which helps with depositing ultra-thin films is an Atomic Layer Deposition (ALD) tool. Depositing ultra-thin metal oxide films, as explained in Chapter 2, can allow the sensors to operate around their charge depletion widths thereby amplifying the sensor response or the sensitivity of the films while operating at relatively low temperatures when compared to the commerical MOx sensors [20][21].

1.3 Atomic Layer Deposition

Atomic Layer Deposition (ALD) is a film deposition method based on the principle of self-limiting growth by chemisorption of reactant gases. Since the 1990's ALD has been extensively used in the microelectronic industry for the ultrathin high-k gate dielectric and its ability for a high aspect ratio deposition.

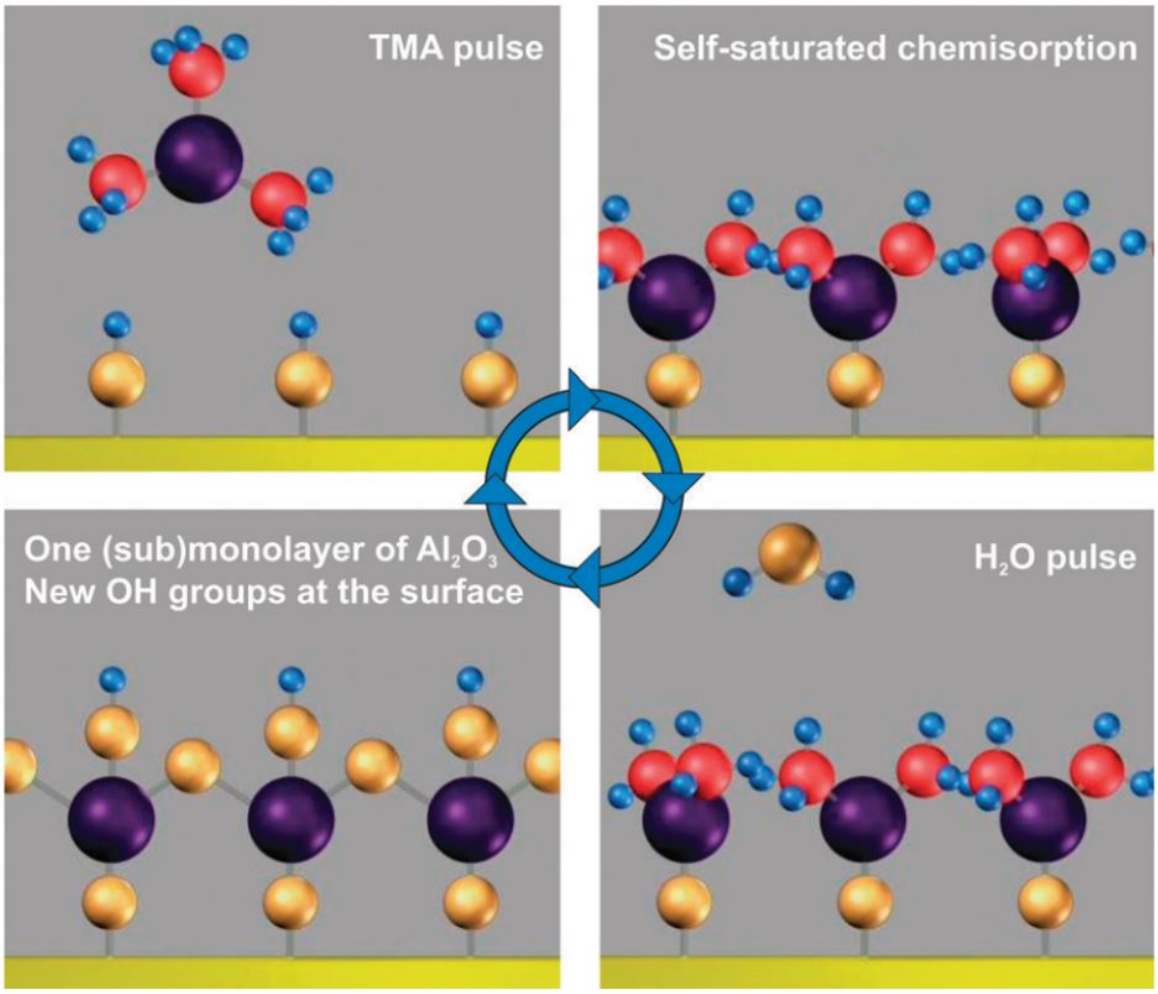

Figure 1.3: Typical ALD process using TMA precursor and H_2O oxidant. Hydrogen (blue), carbon (red), aluminum(purple), oxygen (yellow). Figure courtesy of Cambridge Nanotech Inc.

As an example, Fig.1.3 shows the typical ALD Al_2O_3 formation process using Trimethyl Aluminum (TMA) and water as a precursor as described in [22]. When Al precursor is pulsed into the reaction chamber, TMA reacts with the adsorbed hydroxyl (O-H) groups at surface producing methane (CH_4) as the reaction product. Excess TMA precursor and methane are purged out. Next, water vapor (H_2O) is pulsed into the reaction chamber so that H_2O molecules

react with the dangling methyl group on the surface forming Al-O bridges with hydroxyl terminated surface resulting in one monolayer of the desired film. The two reactions are:

$$Al(CH_3)_3(g) + Si{-}O{-}H \longrightarrow Si{-}O{-}Al(CH_3)_2(s) + CH_4$$

$$2\,H_2O + O{-}Al(CH_3)_2(s) \longrightarrow Al{-}O{-}Al(OH)_2(s) + {}_2CH_4$$

Such self-limiting chemisorption is what enables the precise thickness and uniformity control of film growth which is required for ultrathin dielectric films and high aspect ratio structures.

In this work various metal oxide sensing films - SnO_2, ZnO, SnO_2-ZnO composites, CuO films of varying thicknesses and compositions have been deposited. The ALD deposition has been done at Cambridge Nanotech Savanah 100 system at North Carolina State University and a Cambridge Nanotech Savannah 200 system UNC CHANL. The full fabrication process has been detailed in each experiment.

1.4 Thesis outline

Chapter 1 discussed the motivation, key requirements and the reason for the chosen direction for developing a novel low power consuming E-Nose with capabilities to sense a large catalog of gases.

Chapter 2 goes through the initial ALD fabrications and characterizations done with ozone and acetone, to explore the power and sensitivity limits of SnO_2 sensors. This chapter also discusses the beginnings of building a sensor array and explores the available variables to fine-tune the sensitivity, variation in sensor response to different gas analytes and power budgets of the sensor elements.

Chapter 3 takesup the evolution of a novel sensor array design from its building blocks, its break-up into several modules and subsequent developments till date. Extensive characterization done with ozone, acetone, ethanol, toluene, formaldehyde with multiple sensor elements and data processing using principal component analysis are discussed. Human breath tests done on five sensor surfaces post-fasting to produce acetone and under the influence of alcohol are also discussed.

Chapter 4 discusses the integration of our in-house fabricated SnO_2 sensors with two different system platforms and EPA testing.

Chapter 5 provides a summary of the work done and the possible future pathways from this work.

The appendices discusses work the author was involved with, where wearable physiological health monitors like the electrocardiogram (ECG), photoplethysmogram (PPG), electrodermal activity (EDA) have been developed and tested.

CHAPTER

TWO

ALD GAS SENSING - CASE FOR A BETTER MOX GAS SENSING TECHNOLOGY

This chapter discusses key experiments demonstrating the advantages of ALD MOx (metal oxide) gas sensors over traditional MOx gas sensors. Starting with ALD SnO_2, the relative sensitivity of ALD MOx sensor and its low power operation is discussed. Later its uniquely available knobs to fine-tune senstivity with film thickness and with the choice of substrate are explored. Finally the building blocks of an ALD sensor array are put together and tested with oxidizing and reducing gas to build towards an E-Nose operation.

2.1 Room temperature sensing of VOCs with ALD SnO_2 sensor

This section originally appeared as Tanneeru, Akhilesh, et al. "Room temperature sensing of VOCs by atomic layer deposition of metal oxide." 2016 IEEE SENSORS. IEEE, 2016.

This work demonstrates room temperature sensing of volatile organic compound (VOC) – acetone via an ultrathin film metal oxide sensing layer. We see here that atomic layer deposition (ALD) enables a high quality ultrathin film with precise thickness control. The 14 nm ultrathin SnO_2 thin film was deposited by ALD resulting in VOCs sensing at room temperature. The ultra-low power consumption (less than 50 nW) and the room temperature operation of these devices make them compatible with wearable devices for real-time health and environment monitoring

2.1.1 Introduction

Efficient and accurate sensing of volatile organic compounds (VOCs) at room temperature is sought after, as some VOCs are identified as bio-markers for diseases like diabetes, lung cancer etc., [23]. These sensors can also sense the environment to prevent exposure to harmful carcinogenic agents like benzene, formaldehyde, percholoroetheylene and styrene. While long term exposure to VOCs has reported to cause damage to liver, kidneys, central nervous system, short-term exposure can cause eye and respiratory tract irritation, headaches, dizziness, visual disorders, fatigue, loss of coordination, allergic skin reactions, nausea, and memory impairment. A non-invasive technique of detection of these bio-markers in human breath/environment, combined with advantages of ultra-low power nano-scale devices operating at room temperature (RT)

would help the inclusion of these sensors into wearable devices for long-term and continuous health-monitoring [24]. While many developments in various types of VOC sensing have been reported, low power operation is still a challenge [25]. Low power operation can significantly increase the battery life and enable long term monitoring of VOCs. As compared to the existing fabrication techniques of advanced chemi-resistive sensors, ALD can provide ultra-thin and highly sensitive metal oxide sensors. Its unique advantages of being relatively simple to fabricate, consistent and economical as compared to the nanowire, multi-wall carbon nano-tube based sensors make it more suitable for a mass production [25]. We have previously reported that ALD SnO_2 sensors can detect low concentration levels of inorganic gases like Ozone (O_3) and Nitrogen Dioxide (NO_2) at RT with sensitivity range in parts per billion (ppb) and ultra-low power levels [26] [27]. In this paper, we explore the feasibility of using ultra-low power SnO_2 devices deposited by Atomic Layer Deposition (ALD) for detection of VOC-acetone at RT

2.1.2 Experimental Methods

A. Sensor Fabrication

Thermal oxidation of Si (100) was done to obtain a 500 nm thick SiO_2 layer to electrically isolate devices from the substrate. The metal oxide sensing layer SnO_2 was then deposited in an ALD system (Cambridge Nanotech Savannah 100 model) with Tetrakis ($Sn[N(CH_3)_2]_4$) precursor and O_3 oxidizer at 200°C. Post deposition anneal was done at 600°Cin air ambient for 120 minutes to ensure a desired crystalline phase. Titanium/Gold electrodes were deposited with 10 nm of titanium adhesion layer, followed by 250 nm of gold. ALD film thickness was verified by aberration corrected Scanning Tunneling Electron Microscopy (STEM) with Energy Dispersive X-ray Spectrometry (EDS) and the crystallinity of film was confirmed by the X-ray

diffraction (XRD) patterns (Fig.2.1 and Fig.2.2).

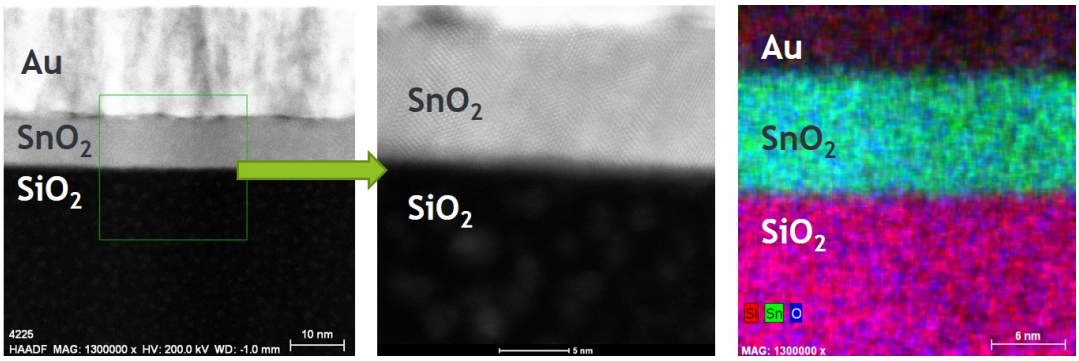

Figure 2.1: STEM-EDS image of fabricated sensor device

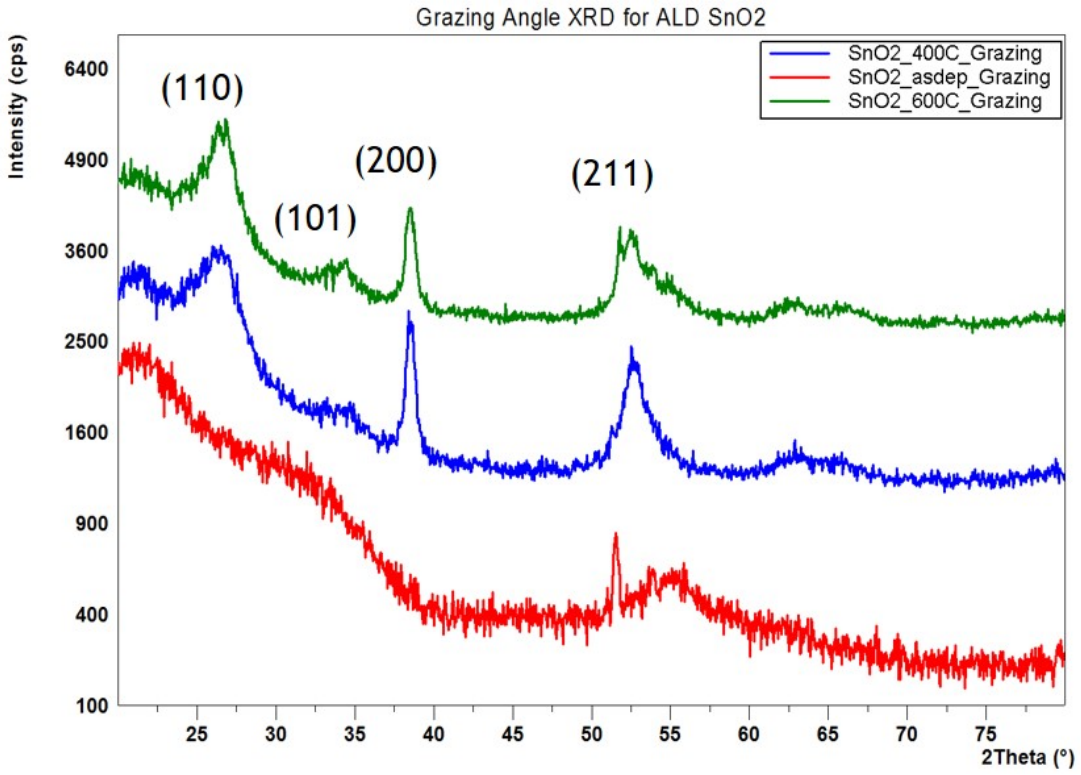

Figure 2.2: Grazing Angle X-ray Diffraction image of film before and after 600°Cpost dielectric anneal

B. Vapor Generation and Sensor Testing Chamber

A custom made bubbler set-up was used to generate the VOCs in the ppm range (Fig.2.3). Nitrogen was used as both carrier and bubbler gas with two mass flow controllers (MFCs) in the range of 5SLM and 2SLM respectively. The temperature bath was maintained at a temperature of about 10°C. The constant flow rate maintained through MFC-2 was low enough to generate a stable concentration of the VOC vapor. Transient response of sensor was monitored by measuring sensor resistance using a Keithley 4200-SCS parameter analyzer under a constant voltage bias of 50 mV.

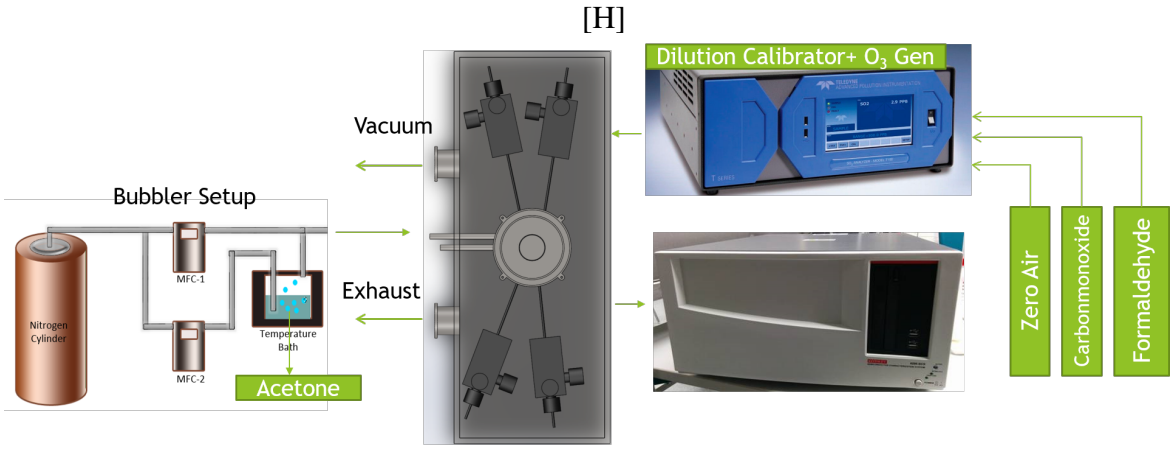

Figure 2.3: Gas sensor testing setup with bubbler to produce VOC vapor on the left and Teledyne to produce T700U, along with measurement setup of Keithley-4200SCS on the right.

2.1.3 Results and Discussion

The physical thickness of ALD SnO_2 film was verified through the Ellipsometry as well as the STEM analysis (Fig.2.1). Since the sensitivity and response time is related to the Debye length of the sensing material [28], Debye length (L_D) was calculated so that the thickness could be adjusted accordingly Eq.2.1

$$L_D = \sqrt{\frac{\varepsilon_0 \varepsilon_r k_b T}{q^2 N_{D/A}}} \tag{2.1}$$

Where

- relative dielectric constant $\varepsilon_r = 13.5\varepsilon_0$ for SnO_2, with $\varepsilon_0 = 8.85 \times 10^{-12}$ F/cm
- Boltzmann's constant, $k_b = 8.614 \times 10^{-5} eV/K$,
- $q = 1.6 \times 10^{-19} C$
- $T = 450K$
- electron carrier concentration, $N_D = 3.6 \times 10^{18} cm^{-3}$ for SnO_2

This gives L_D = 3 nm. Though the exact carrier concentration at RT is not known, it would be less than $N_D = 3.6 \times 10^{18} cm^{-3}$ which is at 250°C[28]. Both T and N_D decrease in the ratio (of L_D) at RT, but since decrease in n_c might be at least in one order of magnitude, we approximate a thickness (L_D) to 14 nm to maximize the sensitivity.

The post deposition annealing (PDA) was done at 600°Cfor 30 minutes to ensure the metal oxide in crystalline phase. The grazing angle X-ray diffraction patterns of the ALD SnO_2 film shows the presence of the main (110) peak confirming the rutile phase. The nanocrystalline

nature of the ultrathin metal oxide obtained after PDA gives higher thermal stability compared to amorphous films by preventing coalescing of any grain like structures. This effect may occur with variation of temperature either in the ambient atmosphere or due to the Joule heating during the electrical measurements [29].

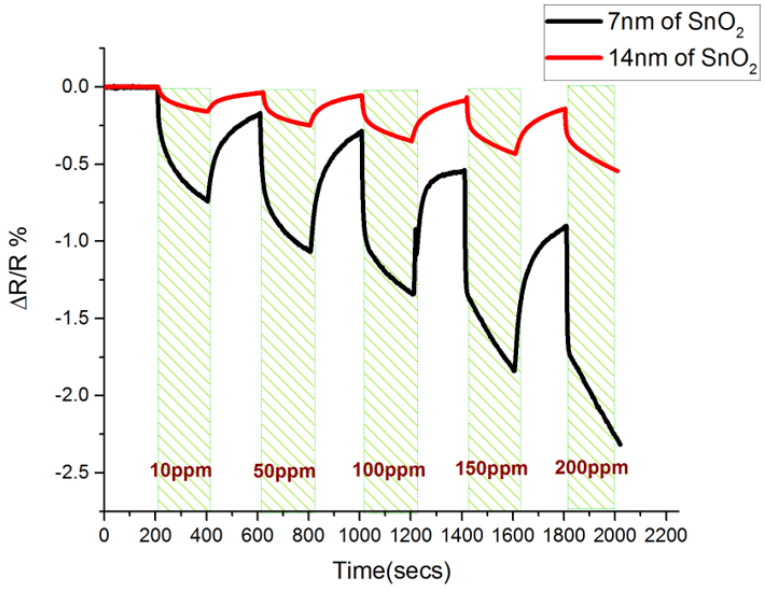

Figure 2.4: Sensor response to acetone when operated at room temperature

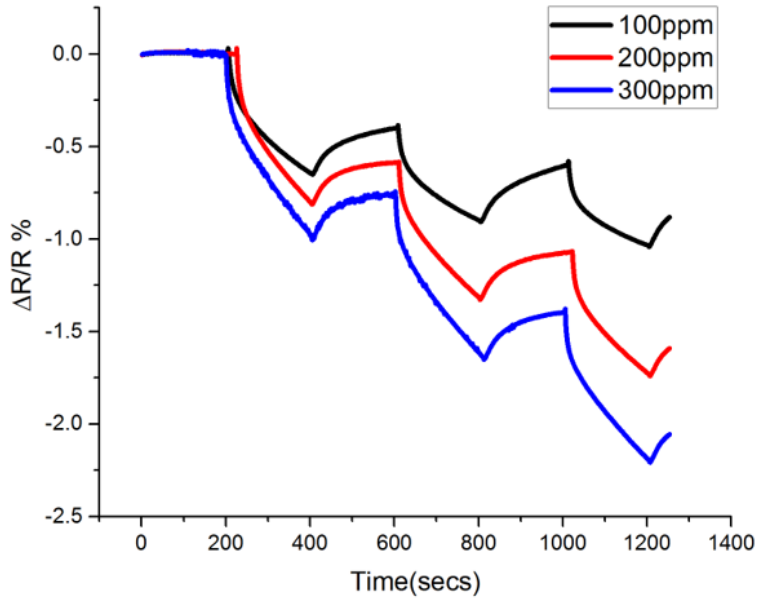

Figure 2.5: Varying response with repeated exposure of various concentrations of acetone and without any targeted recovery

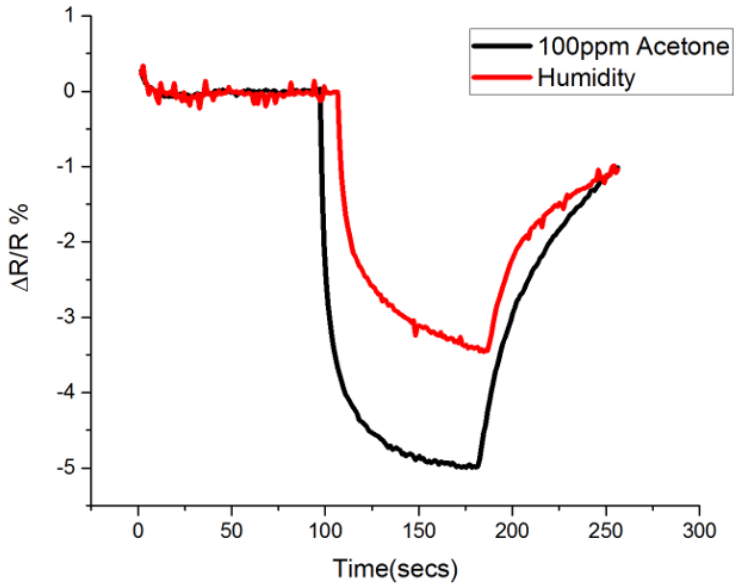

Figure 2.6: Sensor response with humidity alone and humid-acetone with same RH%

The fabricated sensors were tested for response to acetone in the range of 100 ppm to 300 ppm to verify the response of the sensors towards VOCs. The acetone vapor was produced with the setup as described in the Figure 2. The high volatility of acetone meant that the vapor in the 100-300ppm range could be generated only at colder temperature of 10°C, with acetone diluted to 1% by volume with water. The generated acetone vapor concentration was confirmed with a commercial ppbRAE wireless handheld VOC monitor before actual sensor testing. Since the testing chamber is isolated from the vapor generation setup, the electrical characterization was still done at RT. The sensors showed a decrease in resistivity (Fig 3, 4) during acetone exposure cycles. The decrease in resistivity is attributed to the reducing effect of acetone on the metal oxide layer as opposed to the oxidation process, where the resistivity increases as with O_3 and NO_2 [26] [27]. The sensitivity for reducing gases is given by Sensitivity (S) = R_a/R_g where Ra is the resistance of nitrogen and R_g is the resistance of humid acetone). It was observed that the sensitivity increased with the acetone concentration into the testing chamber. Resistance was also measured with dry and humid nitrogen(Fig 5) to exclude the effect of humid nitrogen on the result while calculating the sensitivity. The ratio of Ra/Rg gives the relative change of resistance during SnO_2 exposure cycles with respect to the humid and dry nitrogen exposure cycles. It is noted that the power dissipated by the sensor was less than 50nW. This low power operation is attributed to the ultra-thin ALD SnO_2 films that have high sensitivity. These sensors can lead to long term monitoring of VOCs in our environment

2.1.4 Conclusion

In summary, we have reported on the fabrication of low power ultrathin atomic layer deposited (ALD) SnO_2 gas sensors capable of detecting VOC- acetone in the concentration range of 100–300 ppm at room temperature. The encouraging positive result of sensor's response at

room temperature towards VOCs mean that these sensors could potentially work in the ppb range as well. The sensitivity in the ppb range can be adjusted by controlling the thickness of the ALD deposited metal oxide film. Further detection of other VOCs and improving the selectivity of the sensors towards these VOCs would help to monitor a variety of diseases via human breath. The power consumption for the 14 nm SnO_2 film was as low as 200 nW without any assisted recovery, compared to the tens of milliwatts of power consumption by commercial MOx sensors.

2.2 Varying Sensor Thickness

This section originally appeared as Tanneeru, Akhilesh, et al. "Highly Sensitive ALD SnO2 Sensors and the Role of its Thickness in Gas Sensing Capabilities." 2018 IEEE SENSORS. IEEE, 2018.

ALD films thinner than Debye length by an order have shown higher sensitivity than films comparable to Debye length. Below experiment demonstrates the response of different thickness of ALD SnO_2 film with ozone gas.

2.2.1 Sensor Fabrication

Three Si (100) wafers were thermally oxidized to obtain a 300 nm thick SiO_2 layer which electrically isolates the active sensing area from the substrate. Metal oxide sensing layers of 25 cycles, 50 cycles and 100 cycles of SnO_2 were then deposited in an ALD Cambridge Nanotech Savannah 100 system, at 200°C, using Tetrakis (dimethylamino) tin precursor and O3 oxidant,

on three different wafers which were thermally oxidized. Post deposition anneal was done at 600°Cin air ambient for 120 minutes to ensure a desired crystalline phase. 20 nm of Titanium followed by 250 nm Gold were evaporated in high vacuum at 10-6 Torr as electrode stack. ALD film thickness as measured by a VASE Ellipsometer was 4 nm, 6.5 nm and 12 nm for the 25 cycles, 50 cycles and 100 cycles films respectively. The typical cross-sectional view of the fabricated structure looks as shown in Fig.2.7.

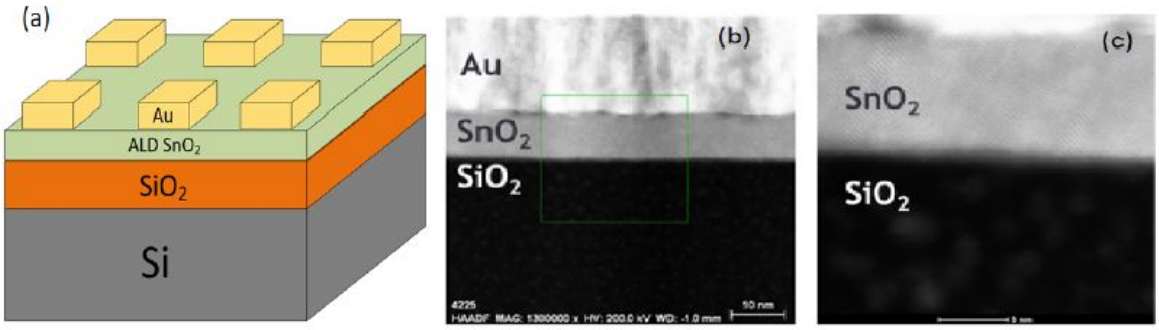

Figure 2.7: a) Fabricated sensor structure b,c) Cross-sectional TEM images on 12 nm SnO_2 film with 600°CPDA

2.2.2 Gas Generation and Sensor Testing

The ozone testing was done using custom built testing chamber and a Teledyne T700U gas calibration system equipped with a UV ozone generator and photometer feedback for precision concentrations. Resistance measurements were made during gas exposure using a Keithley 4200 semiconductor parameter analyzer. The setup was same as shown in Fig.2.3.

2.2.3 Thickness Effect - Response to ozone

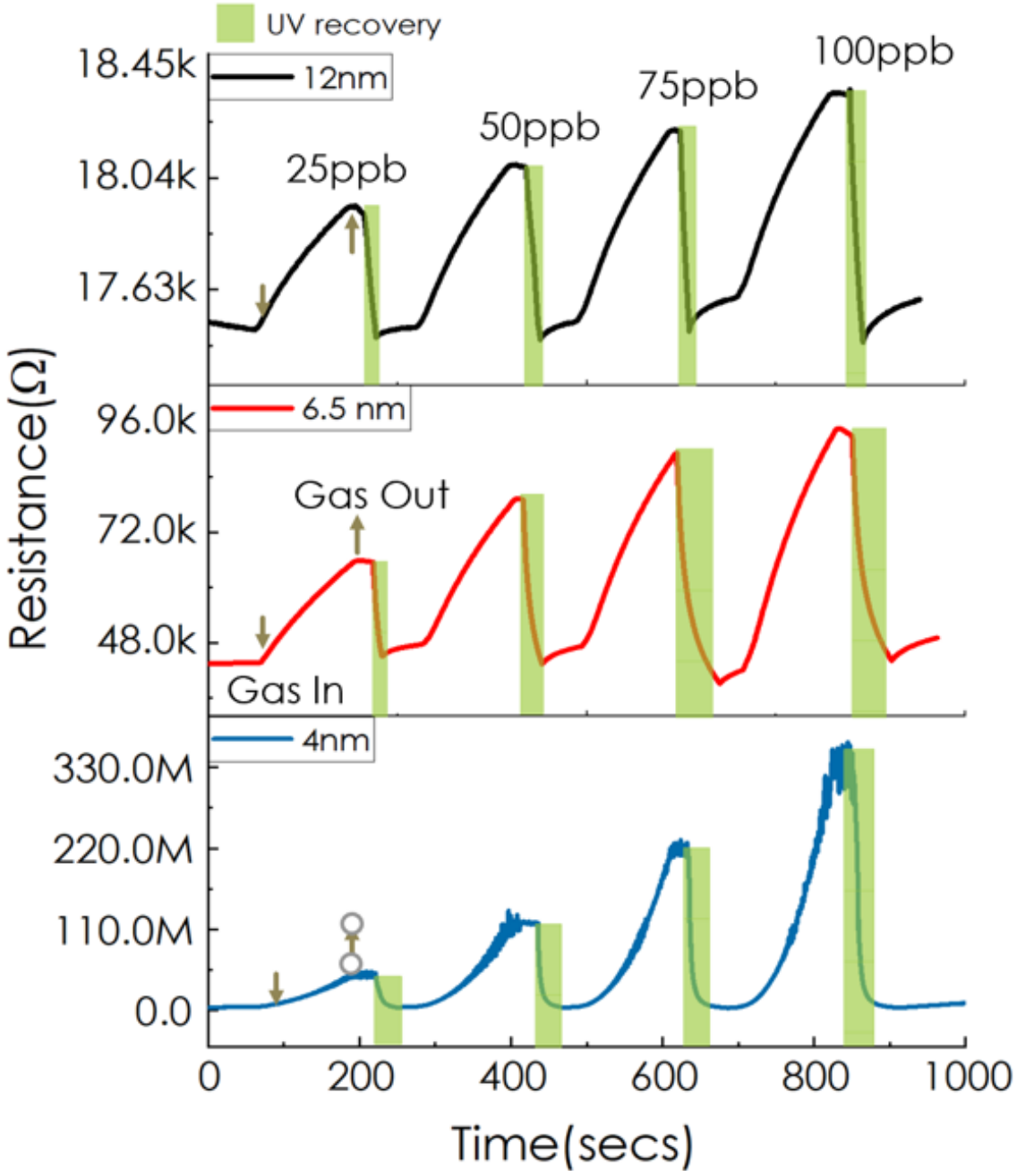

Figure 2.8: Response of 4 nm, 6.5 nm, 12 nm ALD SnO_2 sensing layer with 25 to 100 ppb of dry ozone

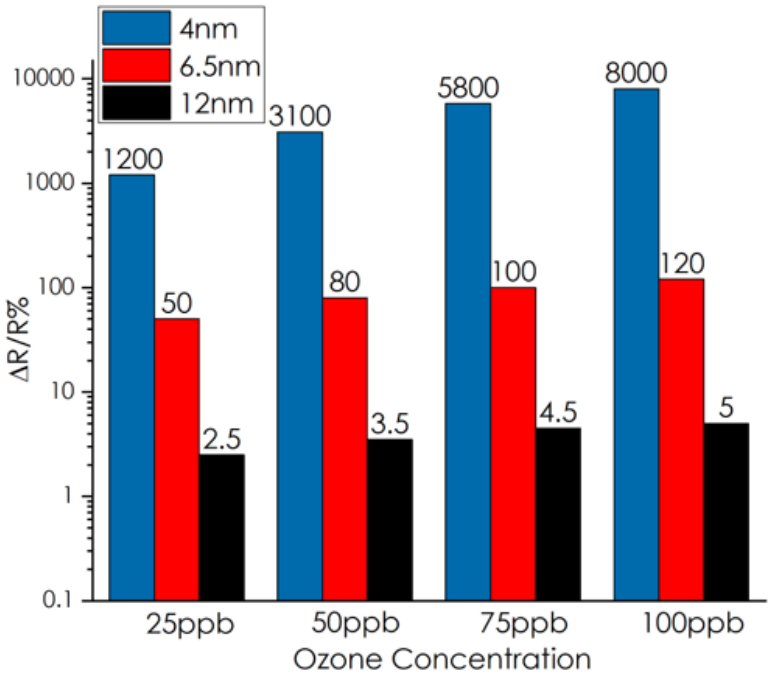

Figure 2.9: A comparison of the relative response of all three sensors plotted on log scale, where $\Delta R/R\% = (R_{gas} - R_{air})/R_{air} \times 100\%$

Fig.2.8 shows the response of freshly fabricated SnO_2 sensors of different thicknesses with ozone. Since the baseline resistances of the sensors vary in the kilo-ohm to mega-ohm range, fractional baseline transformation was used for the comparison of sensor responses from different sensors, where response . Evaluating the sensor response in ozone concentration range of 75 ppb, at which the studies by Environmental Protection Agency's, National Ambient Air Quality Standards suggest pose significant risk in aggravating lung diseases like Asthma, we see remarkable increase in sensitivity by 22 times, with the 50 cycles ALD SnO_2 film over the 100 cycles film and an increase of 58 times, with the 25 cycles film over the 50 cycles film. Since the sensor was operated at room temperature without heat, a 385 nm wavelength UV LED was used to reset the sensor resistance baseline values. The operating power per sensor was under 200 μW including the power consumed by the UV. Using Eq(2.1) and using a carrier

concentration, $N_D = 3 \times 10^{19} cm^{-3}$, as measured from hall measurement for a 100 cycles SnO_2 film. Carrier concentration values for a 12 nm film were obtained from hall concentration in our other work as published in [17]. This gives L_D = 0.8 nm for 100 cycles SnO_2 film. Extrapolating the carrier concentrations for 50 cycles and 25 cycles film using the baseline resistance values in and , assuming change in mobility to be less than an order in magnitude and a linear change in oxygen vacancies in the tin oxide film, the carrier concentrations (nc) were approximated to be $2 \times 10^{18} cm^{-3}$ for 6.5 nm film and $5 \times 10^{15} cm^{-3}$ for 4 nm SnO_2 film. Which give the Debye lengths as 3 nm and 60 nm respectively. The trend of Debye lengths of 0.8 nm, 3 nm and 60 nm for 12 nm, 6.5 nm, 4 nm films respectively indicate that an increasing magnitude in response is seen when the deposited thickness of the ALD films is in the same order or lower than the Debye length at that given thickness. The film which is relatively more depleted of the majority carriers in the sensing layer is thus showing a higher response magnitude.

By designing the thickness of the sensing films to be comparable or lower than the Debye length of the sensing layer would thus yield very high sensitivity to analyte gases even the ppb concentration range.

2.3 ALD and nanocellulose - thin film MOx and high surface area substrates

This section originally appeared as Tanneeru, A., et al., "ALD and Nanocellulose Based Sensors for Ultra-Low Power, Room Temperature Ozone Gas Monitoring for Respiratory Ailments and Wellness Management", ALD Conference, 2018

In this work we report ultra-low power room temperature sensing of ozone gas, by atomic

layer deposited (ALD) tin oxide sensing layer and with a naturally degradable and recyclable substrate-nanocellulose.

Ultra low-powered gas sensors for environment and breath monitoring, can help us tackle health conditions like asthma, emphysema, chronic bronchitis by monitoring for permissible levels of gases like ozone in the atmosphere. The sensitivity of these sensors should be in the 50-100 ppb concentration range to detect ozone in the atmosphere so as to avoid exacerbating these chronic conditions. Traditional sensing methods of high temperature heating of the substrate (200°C-450°C), consume high-power and are therefore not compatible with wearable technology for long-term gas monitoring. We at ASSIST (Advanced Self-Powered Systems of Integrated Sensors and Technologies), met the challenge of making such highly sensitive, selective sensors with low power consumption and room-temperature operation, by depositing nanoscale thick metal oxide layers by ALD technique. Nanocellulose was used as a substrate in this work for its bio-compatibility, high mechanical ruggedness, high surface area, thermal stability and flexibility. It also has a conformal adherence to epidermal surfaces without adhesives via Vanderwaals forces and is less susceptible to degradation due to mechanical stress.

The sensor fabrication started with a nanocellulose substrate produced by oven drying cultured bacteria over glass slides. A 6.5 nm or 100 cycles of SnO_2 sensing layer was deposited by atomic layer deposition (Cambridge Nanotech Savannah 100 model) with Tetrakis (dimethylamino tin (IV) – $Sn[N(CH_3)_2]_4$) precursor at 200°C, with a 20 nm ALD Al_2O_3 interlayer to ensure electrical isolation with substrate. Titanium (20 nm)/Gold (250 nm) electrodes were deposited by e-beam evaporation. The sensors were tested for response to ozone in 25 to 100 ppb concentration range in a humidity and temperature controlled testing chamber. UV LED with a 5-10% duty cycle was used to reset the resistance to the baseline value keeping the total power consumption under 200 μW. As shown in the supplementary attachment the sensor shows

comparable response against a sensor fabricated under similar conditions on a silicon substrate. This sensor therefore integrates the capabilities of an ultra-low power, highly selective and sensitive nano-scale thick ALD deposited sensing layer with a highly bio-functional nanocellulose substrate. Combined with the body powered, battery-free and wearable health monitoring systems as developed at ASSIST, this has a potential to play a key role in management of respiratory ailments.

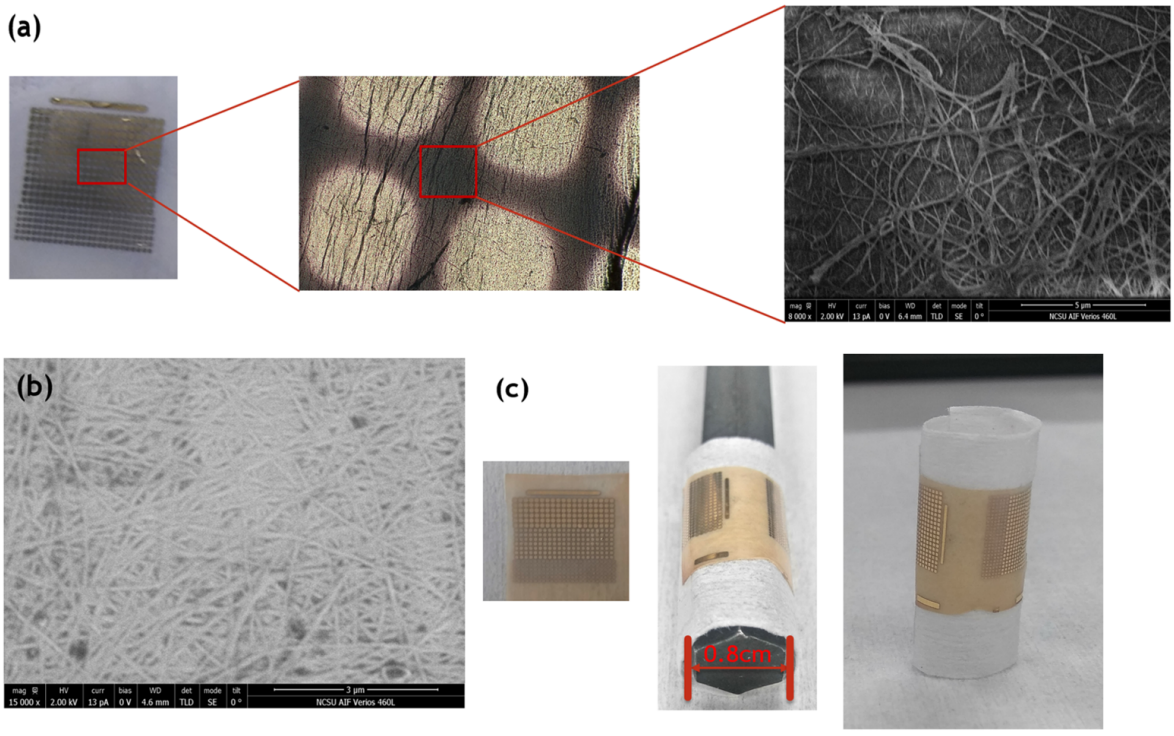

Figure 2.10: a) Optical, microscopic and SEM image of nanocellulose before ALD metal oxide deposition b) SEM image of nanocellulose post ALD deposition c) Images demonstrating the flexible nature of nanocellulose

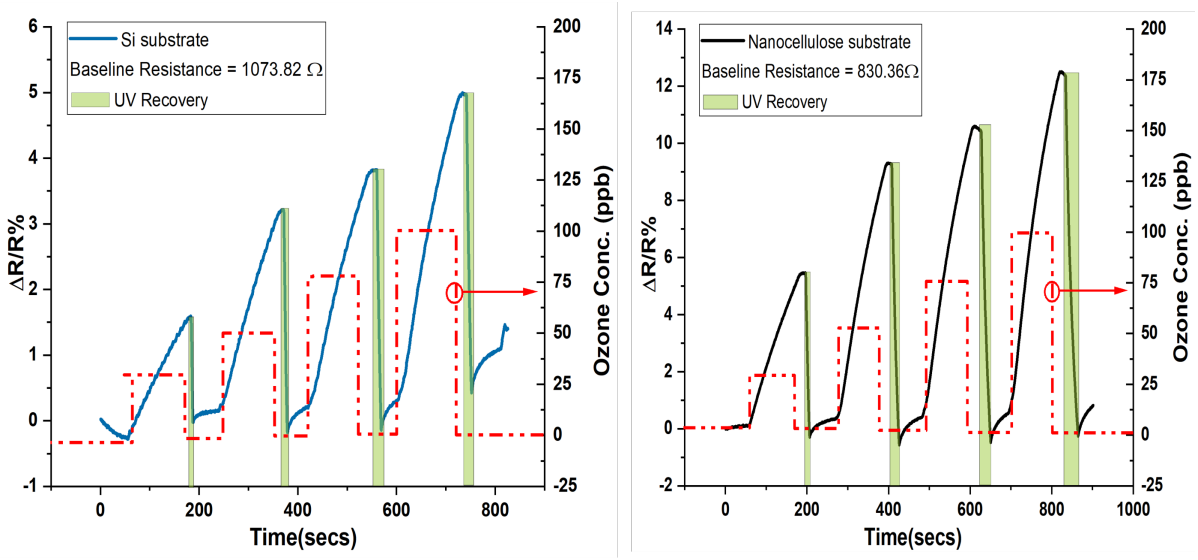

Figure 2.11: Response from Si-sensor (w/o PDA) (left) and Nanocellulose sensor(right) with 25 to 100 ppb of Ozone

2.4 Building Blocks: n-type and p-type MOx sensors

This section originally appeared as Tanneeru, Akhilesh, Bongmook Lee, and Veena Misra. "Building Blocks of a New ALD E-Nose-A First Step: N-Type and P-Type ALD Sensors." 2018 IEEE SENSORS. IEEE, 2018.

The conventional method for chemical sensing is to use a “lock and key” approach, so that each sensor (receptor) is highly selective towards a chosen analyte. While this approach would work well under controlled gas-generating environments and interfering gases, it wouldn’t be easy to scale the sensing capabilities to a larger catalog of gases and to deal with new interfering gases. Therefore, an alternative approach, inspired by mammalian olfactory system was conceived in designing a new architecture of sensor arrays - “E-noses”. Here the working principle is to “not” have perfect “lock and key” pairs, rather each receptor would react with

multiple analyte gases with inevitable cross-sensitivity but diverse response magnitudes. Each sensor unit selectivity could here be broadly designed to narrow down analytes basing on reactivity rate, similarities in polarity or in structures of analyte molecules[12].

Under one such classification of analyte gases into oxidizing and reducing gases, p-type and n-type sensors give an opposite and unique response magnitude owing to their hole and electron conduction mechanisms respectively. These sensors could therefore be considered as the "building blocks" of a new type of sensor array which could be fabricated with the help of ALD technique. In this section we discuss the response characteristics of such p-type and n-type sensors tested in response to analyte gases - ozone, acetone and humidity.

2.4.1 Sensor Fabrication

Two Si (100) wafers were thermally oxidized to obtain a 300 nm thick SiO2 layer for electrical isolation. Metal oxide sensing layer of 50 cycles (6.5 nm thick film) of Tin oxide (SnO_2), was then deposited in an ALD Cambridge Nanotech Savannah 100 system, at 200°C, at NC State University, using Tetrakis (dimethylamino) tin precursor and O3 oxidant. On another thermally oxidized Si substrate, 600 cycles (20 nm thick film) of Copper oxide (CuO) was deposited with Cambridge Nanotech Savannah 200 system, at 190°C, at UNC CHANL facility using Bis(dimethylamino-2-propoxy) Cu(II) precursor and water pulse. Post deposition anneal was done at 600°Cin air ambient for 120 minutes to obtain a crystalline phase. Electrodes with 20 nm of Titanium followed by 250 nm Gold were deposited by E-beam evaporation.

2.4.2 Gas Generation and Sensor Testing

The ozone testing was done using our custom built testing chamber and a Teledyne T700U gas calibration system equipped with a UV ozone generator. Acetone and humidity were generated with a bubbler setup to generate the gas into our testing chamber. The gas concentration of acetone was verified using ppbRAE PGM 7240 - a handheld volatile organic compound (VOC) monitor. Relative humidity values that were generated were verified using a Honeywell HIH4010 sensor. Keithley 4200 semiconductor parameter analyzer was used for electrical characterization under gas exposure. The experimental setup is same as Fig.2.3.

2.4.3 Response with ozone and acetone

The response of the n-type SnO_2 and p-type CuO with ozone is shown in Fig.2.12 and Fig.2.13 respectively. The baseline resistances of the SnO_2 and CuO sensor were in the 50 kΩand 100 MΩrange respectively at room temperature. So, a fractional baseline transformation was used to obtain a comparable relative response from the two sensors. Also, since the high baseline resistance of CuO at room temperature would mean very low current and more noise while measuring response, the response curves in Fig.1 were obtained at a temperature of 150°Cat which, the baseline resistance of SnO_2 and CuO were in the order of 10 kΩand 10 MΩrespectively. By using a thicker film of CuO with ALD, higher hole carrier concentration could be obtained. That will enable to run the sensors at room temperature and with under $200\mu W$ power operation. In the case of SnO_2 where room temperature operation was possible our results show ultra-low power operation [30][31]. Ozone and Acetone were selected to be representative of oxidizing and reducing gases. Selected concentration range of ozone was relevant to avoid aggravating conditions like Asthma, while for acetone, custom gas generating

setup is needed to reach a relevant range in the order of 1.8 ppm, helpful to detect diabetes. High humidity in human breath, environment and its interference were the reasons to choose humidity as another ambient. The sensor response amplification of thin films could be explained by its correlation with the Debye length (L_D) of the sensing material [28], which is calculated as

$$L_D = \sqrt{\frac{\varepsilon_0 \varepsilon_r k_b T}{q^2 N_{D/A}}} \tag{2.2}$$

Where

- relative dielectric constant $\varepsilon_r = 13.5\varepsilon_0$ for SnO_2 and $18.1\varepsilon_0$ for CuO with ε_0 = 8.85×10^{-12} F/cm,
- Boltzmann's constant, $k_b = 8.614 \times 10^{-5} eV/K$,
- $q = 1.6 \times 10^{-19} C$, $T = 450K$ and electron carrier concentration,
- $N_D = 2 \times 10^{18} cm^{-3}$ for SnO_2 and hole carrier concentration, $N_A = 1 \times 10^{16} cm^{-3}$ for CuO (extrapolated values from [17] using $R = \rho l/A$ and $\rho = 1/\rho q \mu$).

This gives Debye length of 3.8 nm for SnO_2 and 62 nm. By fabricating a thin sensing film with thickness in the order or lower than Debye length we operate the sensor in the depletion phase of the sensor ensuring a high response magnitude than thick film sensors at a given temperature. First derivative curves obtained from resistance curves shows a linear relation of adsorption and desorption peaks with varying gas concentration. A 10-point FFT smoothing was done with these derivative curves. The relation between dR/dt versus concentration for n-type and p-type for oxidizing gas like ozone is given below [32]. The conductivity is given by $\sigma_n = nq\mu_n$, where n, μ_n are the electron carrier concentration and mobility, if an analyte concentration 'C' in introduced in time 't', then the conductivity would be $\sigma_n = (n - \alpha Ct)q\mu_n$,

where α is the absorption coefficient. Taking an inverse and derivative, we have $\frac{d\rho}{dt} = \frac{\alpha C}{(n-\alpha Ct)^2 q\mu_n}$. Taking 'n' to be much larger than the rate of resistivity would be $\frac{d\rho}{dt} = \frac{\alpha C}{n^2 q\mu_n}$. Since Resistance, $R = \rho l/A$ it implies $\frac{dR}{dt} \propto \alpha C$. Similarly, for desorption we would have $\frac{dR}{dt} \propto -\alpha C$.

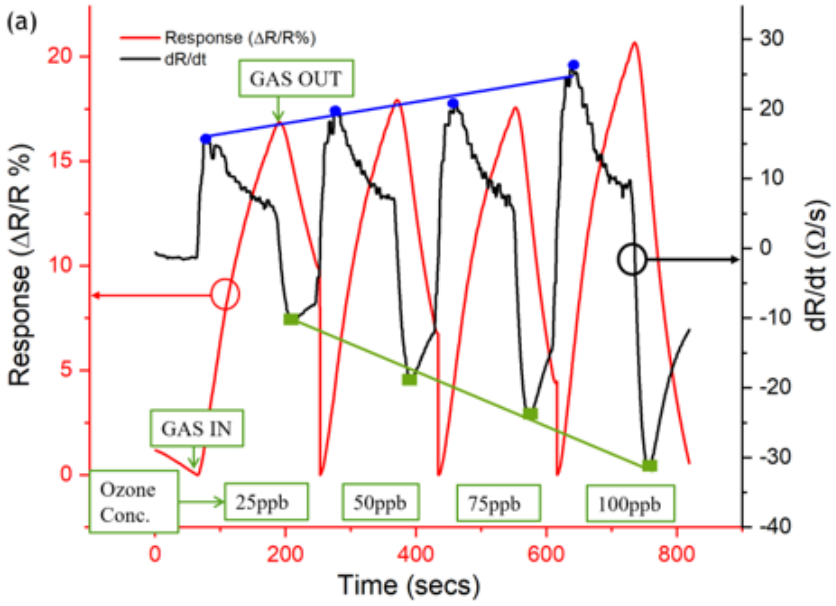

Figure 2.12: Response and first derivative curves of SnO_2 sensor with ozone

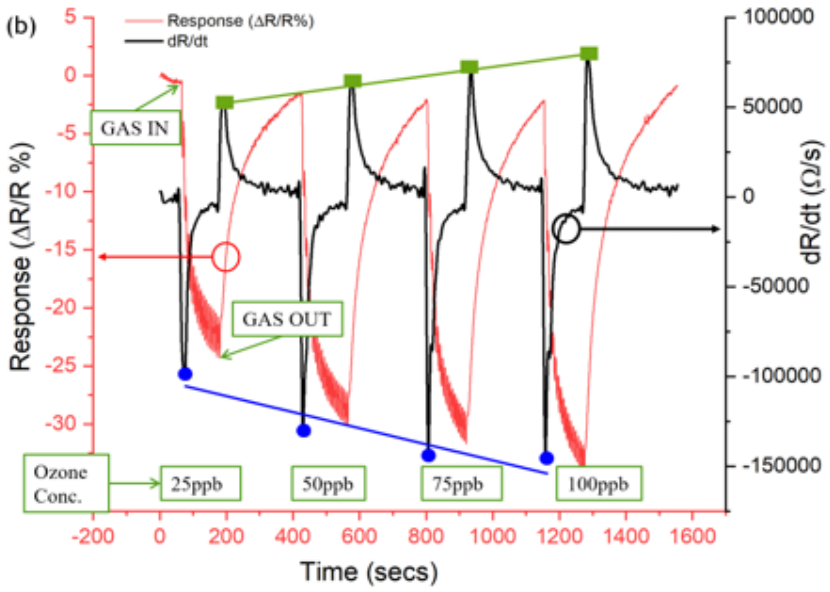

Figure 2.13: Response and first derivative curves of CuO sensor with ozone

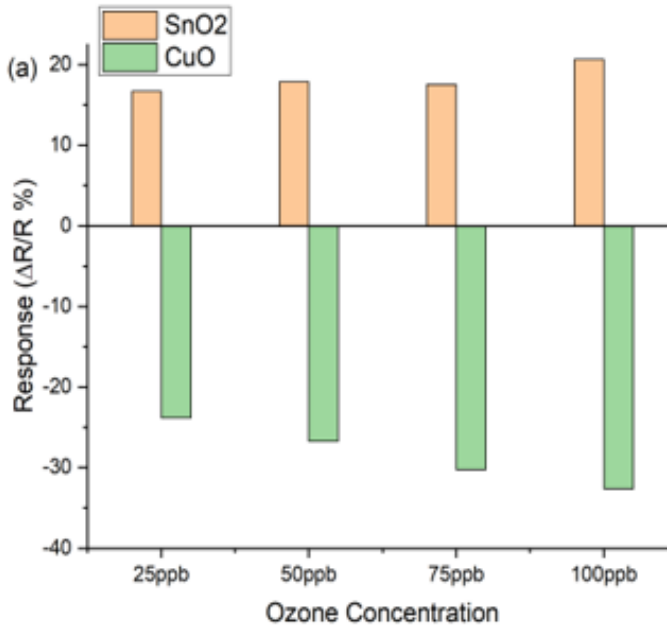

Figure 2.14: Peak response of SnO_2 and CuO after 2 mins of exposure at various ozone concentrations

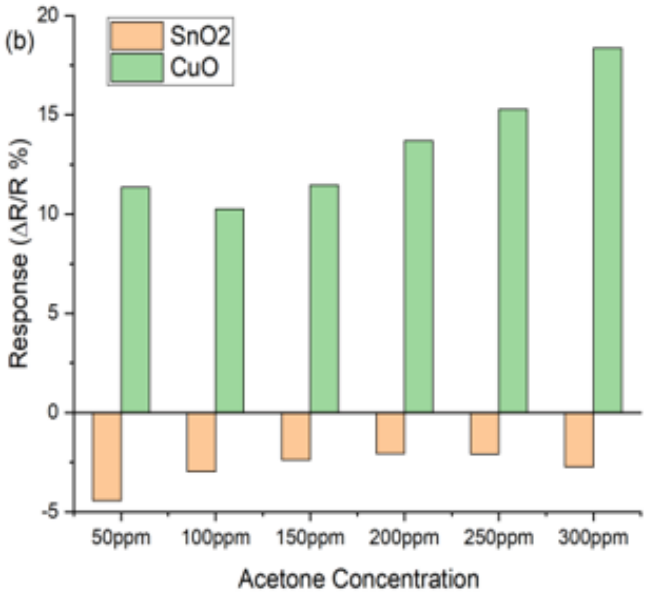

Figure 2.15: Peak response of SnO_2 and CuO after 2 mins of exposure at various acetone concentrations

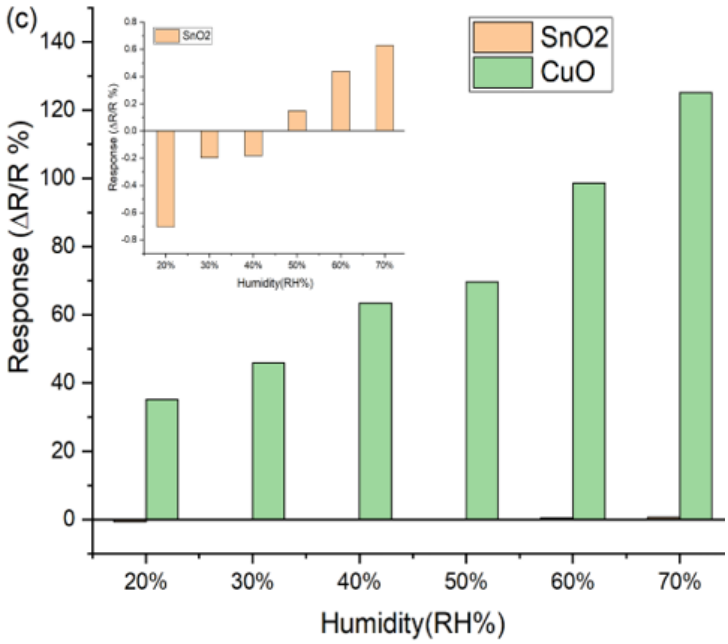

Figure 2.16: Peak response of SnO_2 and CuO after 2 mins of exposure at various humidity concentrations

From Fig.2.12 we can see that adsorption (blue line) and desorption peaks (green line) from the derivative curve vary linearly with the concentration with a positive and negative slope respectively as also seen from the equations above. We can proceed similarly for holes but introducing ozone would increase the holes concentration here, so the equation looks like $\sigma_p = (p + \alpha Ct)q\mu_p$ with $\frac{dR}{dt} \propto -\alpha C$, which could be seen from Fig.2.13 where the blue line for adsorption has a negative slope and desorption given by $\frac{dR}{dt} \propto \alpha C$ has a positive slope as depicted with the green line. The quick rise times of first derivative curves from baseline to peak as seen would help to quickly gauge the analyte concentration and therefore this serves as an important metric for e-noses pattern recognition techniques. From Fig.2.14, Fig.2.15 and Fig.2.16, the unique response of the sensors with ozone, acetone and humidity respectively are seen. By introducing the acetone, reducing type analyte, the opposite response magnitudes to that of ozone are seen. With humidity alone, see the SnO_2 (6.5 nm) film is seen to be less responsive with absolute response values < 1% and CuO is more selective towards it.

Along with above sensors another n-type sensor 100 cycles (8 nm) of ZnO was also deposited along the same fabrication method as in Section 2.4.1 and tested with ozone and acetone. Principal Component Analysis (PCA) with all three sensors tested against ozone and acetone is plotted in Fig.2.17. Features extracted from pre-processed data were max and min settling times, ΔR between local maxima and minima, standard deviation, mean cycle of peaks and peak response values in gas-on and gas-off cycles. Over 98% of variance with just two components of PCA is observed from the tests.

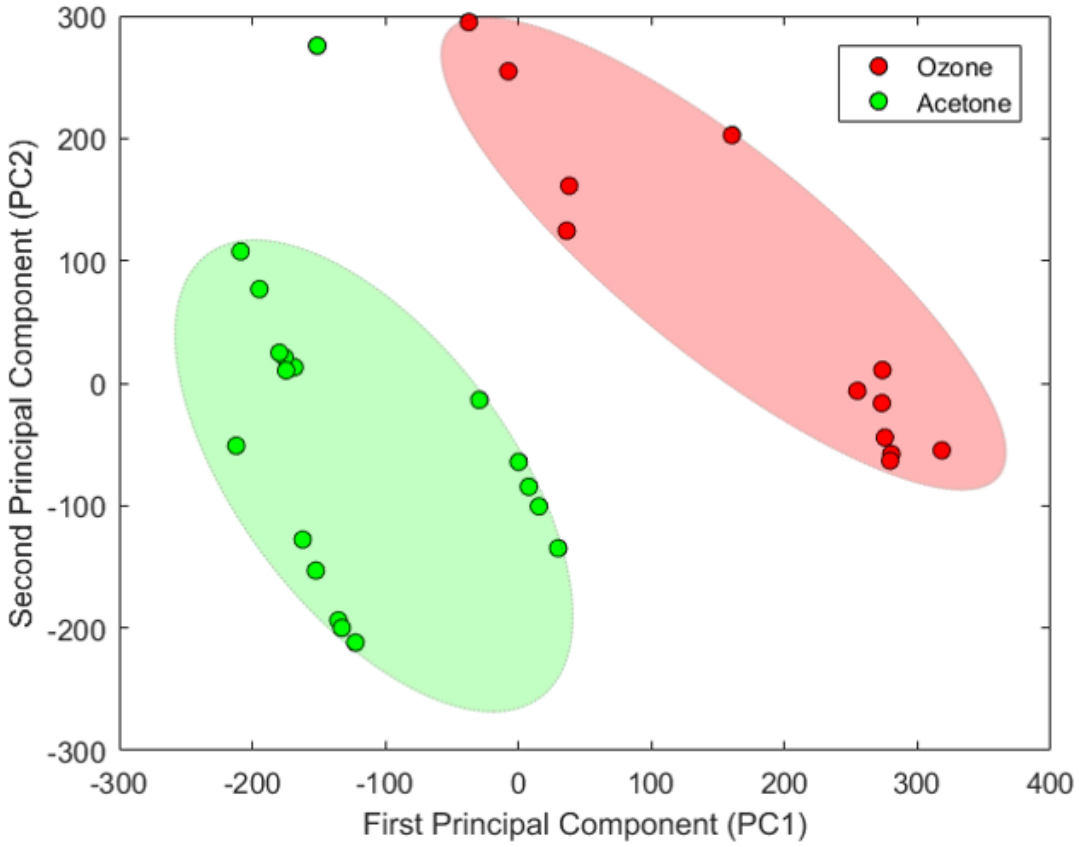

Figure 2.17: PCA with ozone and acetone with SnO_2, CuO and ZnO sensors

2.4.4 Conclusion

These basic building blocks lay the foundations to a sensor array or an E-Nose, which can now be broadly designed to narrow down analytes basing on reactivity rate, similarities in polarity or in structures of analyte molecules rather than being highly selective to each analyte gas.

2.5 Summary

By classifying the properties of the gas and combining this with machine learning algorithms to narrow down analytes basing on the adsorption mechanism a new type of E-Nose from ALD deposited films could be developed. We see that the thickness of the ALD film can help fine tune sensitivity of the film. While by combining the various elements of ALD sensor array we can proceed to build it though one challenge remains. The traditional path to integrating these sensors into an array is to combine various elements here by separate fabrication, anneal, dicing, bonding which configures it into one big array of sensors. We address that problem in work discussed through the next chapter.

CHAPTER

THREE

FROM ALD SENSORS TO E-NOSE: NOVEL MONOLITHIC SENSOR ARRAY PLATFORM

This chapter discusses the evolution of a novel monolithic sensor array design from its discrete building blocks. Its break-up into several modules, simultaneous development, optimization and fabrication is discussed. Characterization was done with ozone, acetone, ethanol, toluene, formaldehyde with multiple sensor elements and data processing using principal component analysis are shown. Finally some testing for a real life tests are done with five sensor from the exhaled breath of a human subject, post-fasting to produce acetone and under the influence of alcohol.

3.1 Introduction

This section originally appeared as Tanneeru, Akhilesh, et al. "A novel monolithic array of multiple metal oxide sensors for E-Nose applications via selective on-chip annealing of nanolayered ALD stacks." 2019 IEEE SENSORS. IEEE, 2019.

The development of ultra-low power, high density, sensitive, reliable, selective and scalable gas sensor technology is critically needed for internet of things (IoT), wearable electronics, smart phones, and medical devices. Adapting these sensors for environment and breath monitoring, can help us tackle health conditions like asthma, diabetes, lung cancer, kidney failure by monitoring for permissible levels of the pertinent gases [33]. All commercially available sensor technologies suffer from drawbacks that limit their seamless implementation. One good example are electrochemical sensors - relatively accurate and reasonably selective but suffer from large size, surface poisoning and long-term stability. Miniaturized form factors and high-volume production are essential to lower sensor costs. Plus, expanding sensing capabilities to include a larger catalog of gases requires e-nose approaches. Here, metal oxide-based sensors integrated with microelectromechanical (MEMS) micro-hotplates is a very attractive option [34]. However high temperature operation typically 400°C, widely used to improve sensor operation, is not compatible with wearable and continuous use [21][20].

In our work previously at Advanced Self-Powered Systems of Integrated Sensors and Technologies (ASSIST), we overcame few such drawbacks and demonstrated high sensitivity and room temperature operable sensors by depositing nanolayered ALD metal oxide films [35][36]. By assembling these discrete ALD sensors post fabrication, we could achieve a highly functional ALD E-Nose. This process can get cumbersome with an increase in the number of sensor elements in the array, giving us a compelling call to simplify the fabrication process for

an E-Nose.

In this work, we thus propose a novel method to address this issue in these two steps: (i) Depositing ALD ultra-thin metal oxides that have demonstrated sensor power levels < 200μW owing to their nano-layer thicknesses and (ii) On-Chip selective annealing through thin membrane heater arrays that can convert ALD multilayer arrays into different sensing surfaces by a thermally driven intermixing. This novel approach allows for monolithic fabrication of multiple sensing surfaces using only a single ALD process step. The same thin-film heaters utilized for on-chip selective heating can be used at lower temperatures to facilitate reliable and low power sensor operation. This can thus enable an ultra-low power metal oxide sensor-array consisting of multiple sensing materials combined with heating elements from the existing CMOS/MEMS technology- providing a disruptive E-nose platform for quick and economical adoption into wearable/IoT electronics. In this paper we demonstrate the proof of concept of our proposed idea.

3.1.1 Experimental Methods

A. Sensor Fabrication

A Si (100) wafer thermally oxidized to obtain a 300 nm thick electrically insulating SiO_2 layer was used as the substrate for atomic layer deposition of metal oxides. Two metal oxide sensing layers: 12 nm of SnO_2 followed by 4 nm of ZnO were deposited using ALD. To simulate the proposed MEMS/SOI based on-chip annealing, ALD stacks were annealed at 300°C, 600°C, 900°C, 1200°Cin N2 ambient for just 1 min each. 20/250 nm of Ti/Au contacts were deposited using E-beam evaporation.

B. Analytical Methods

XPS (mono-chromated Al X-ray source with - photon energy 1486.6 eV, emission current of 10 mA, 30° incidence, 90° take-off angle) was used to get the survey of atomic composition. Grazing incidence XRD (2-theta geometry, step mode with a 0.05 step) was used to obtain diffraction patterns of our thin metal oxide films. FEI Talos F200X was used for electron microscopy imaging.

3.1.2 Gas Testing Setup

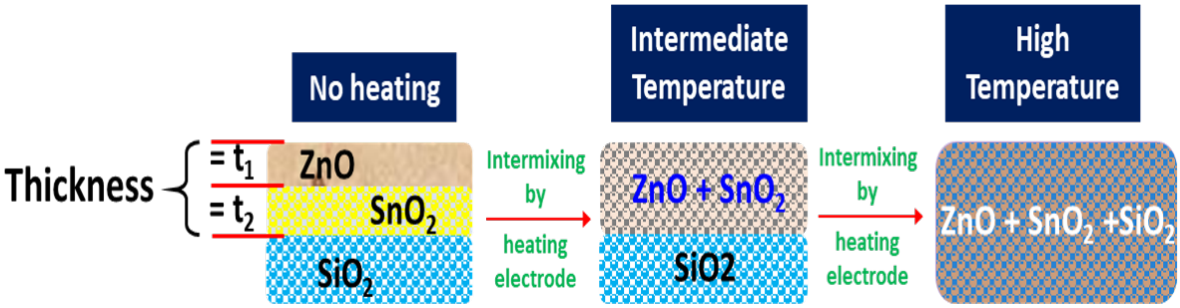

Figure 3.1: Concept of on-chip annealing of sensor surfaces

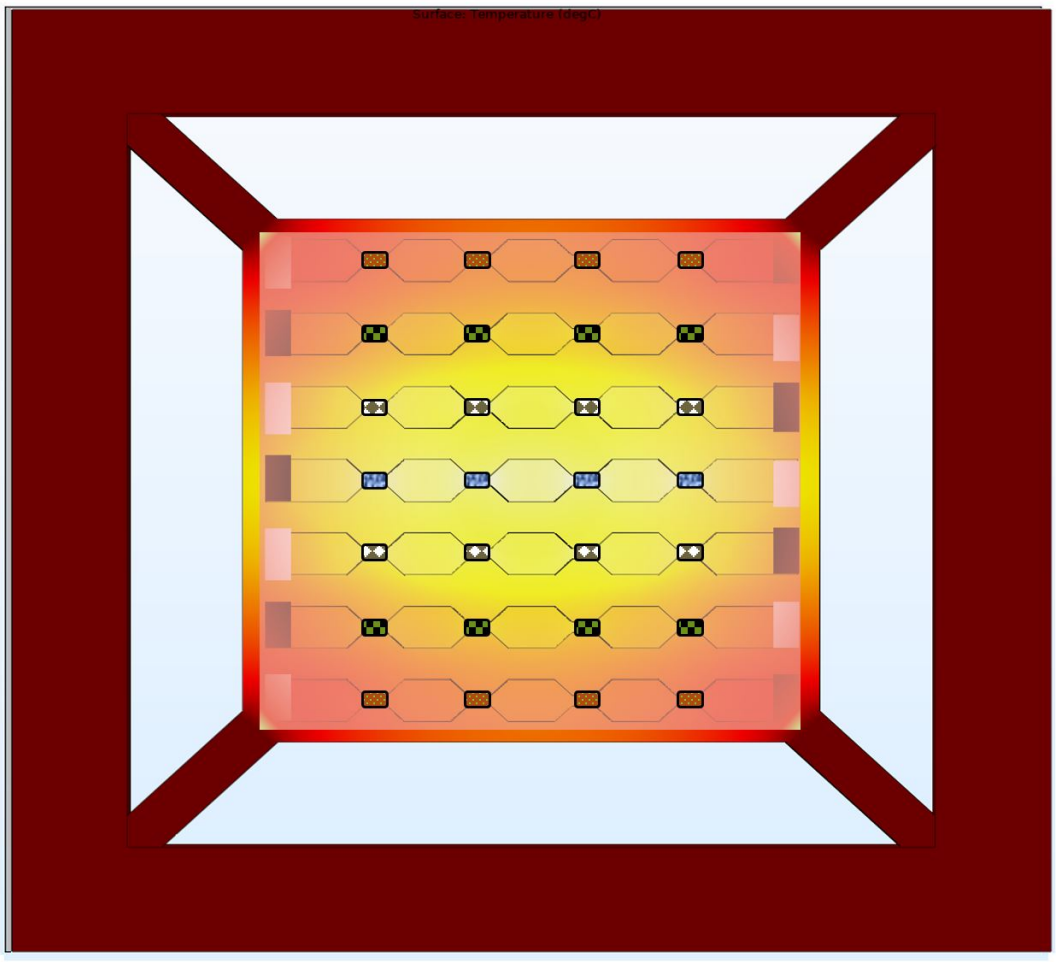

Figure 3.2: First design of a fully fabricated monolithic sensor array

Gas testing was performed in a custom-built testing chamber. Ozone gas for testing was generated using a Teledyne T700U gas calibration system equipped with a UV ozone generator. Acetone was generated with a bubbler setup and diluted to right concentration with Zero Air in a mixing chamber. The gas concentration of acetone was verified using ppbRAE PGM 7240 - a handheld VOC monitor. Keithley 4200 semiconductor parameter analyzer was used for electrical characterization under gas exposure. The testing setup is same as shown in Fig.2.3.

3.1.3 Results and Discussion

Fig.3.1 and Fig.3.2, shows the simplicity of our proposed fabrication process over the conventional sensor array fabrication process where such selective annealing isn't possible, under the same stack deposition conditions. As seen in the TEM Images (Fig.3.5 and Fig.3.6), with rise in anneal temperature our ALD metal oxide system appears to be progressively diffusing, first among the two metal oxide layers at lower temperatures and then into the SiO_2 layer at higher temperatures. An XPS survey of the samples' surface in % atomic values as seen in Table.3.1, corroborate the inter-mixing of oxide stack as seen from the TEM images. XPS used in this experiment picks the signal from the top 10 nm from the sample's surface, so gives a good picture of the inter-diffusion going on in the ALD metal oxide layers, as the total ALD stack thickness is 16 nm. Samples annealed in 600°C-900°Crange were more crystalline than samples outside that temperature window (Fig.3.4). Upwards 900°Cit appears that the resistance to the diffusion of Sn-O-Zn in SiO_2 decreases and we see a greater surface concentration of Si.

Table 3.1: Atomic % values vs anneal condition as obtained from the XPS survey

Atomic % Anneal Cond.	*Sn*	*Zn*	*O*	*Si*
As-deposited	24	11	65	0
300°C Anneal	24	10	66	0
600°C Anneal	33	1	66	0
900°C Anneal	19	0	65	16
1200°C Anneal	1	0	61	38

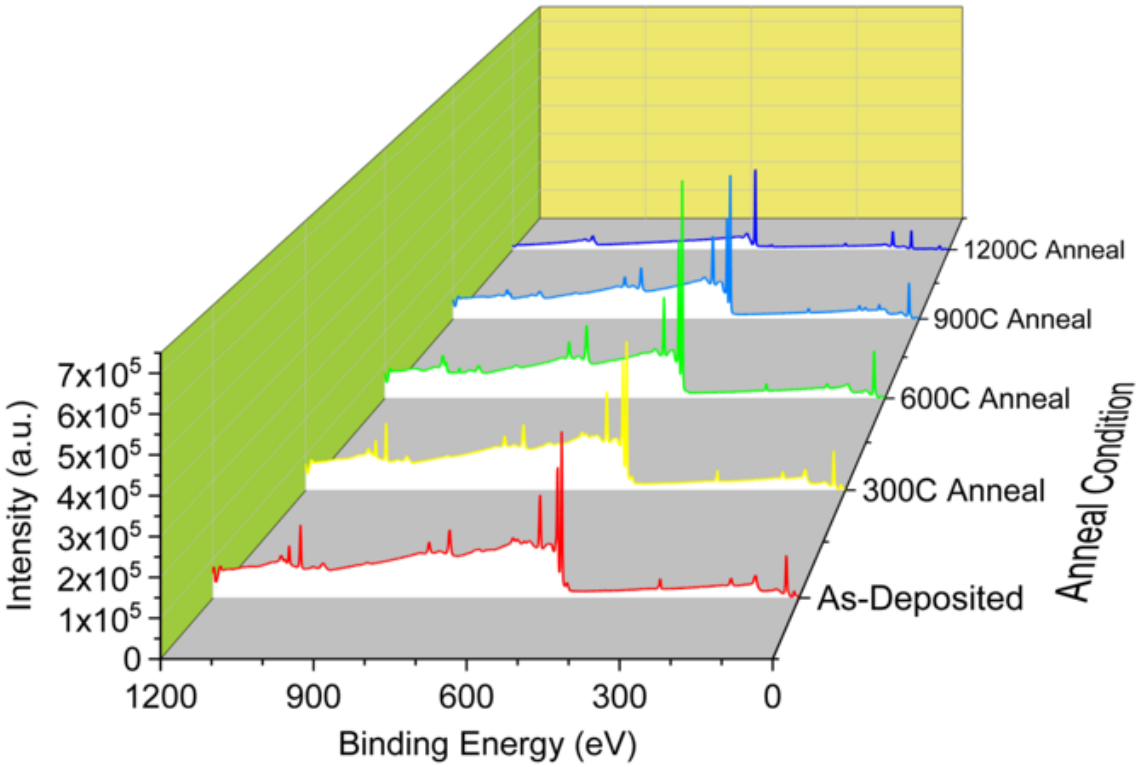

Figure 3.3: A 3D waterfall plot of XPS survey spectrum obtained on all the samples. The atomic % values are tabulated in Table 1

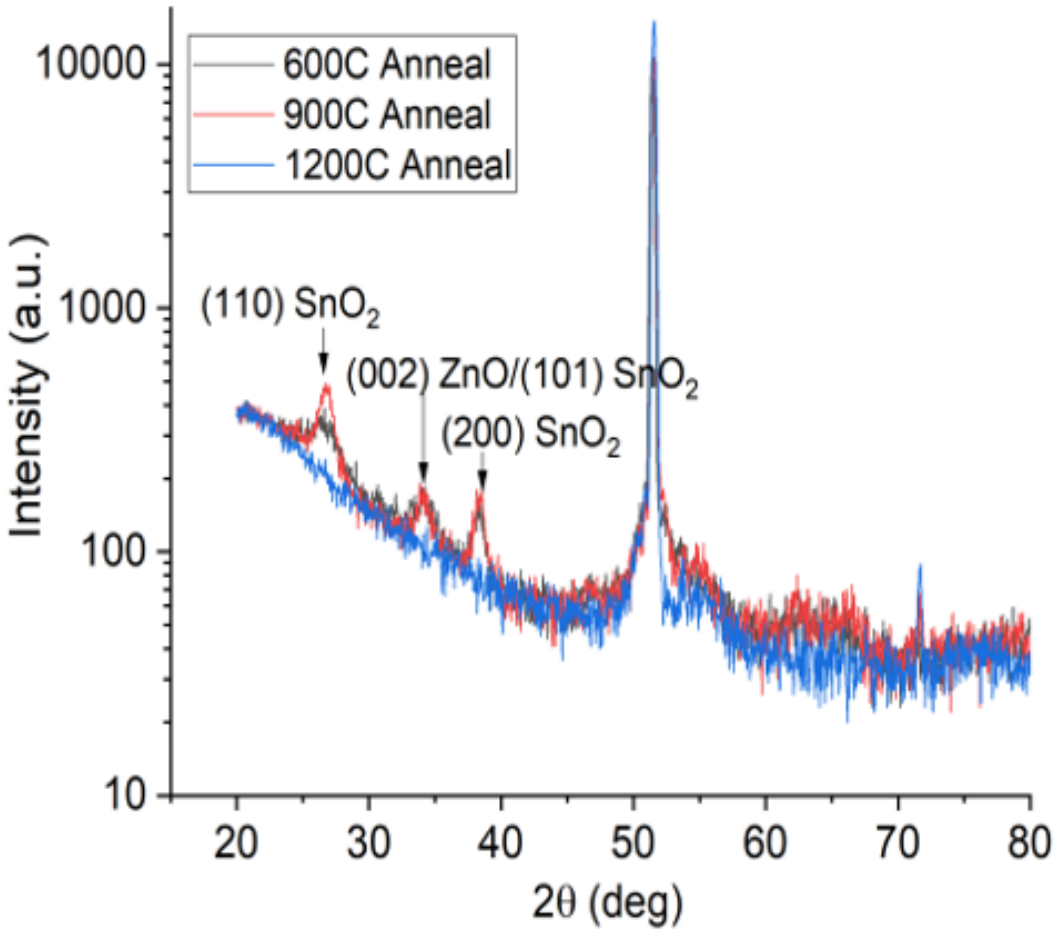

Figure 3.4: Grazing Incidence X-Ray Diffraction peaks of samples annealed at 600°C, 900°Cand 1200°C, with relevant peaks from metal oxides labelled

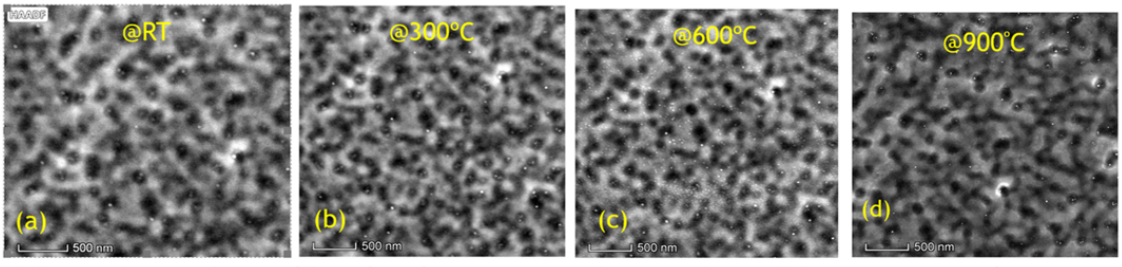

Selected electron microscopy images of the surface of SnO_2-ZnO composites across the annealed temperature range of RT to 900°C.

Figure 3.5: Selected electron microscopy of the SnO_2-ZnO composites across the annealed temperature ranges of RT to 900 °C

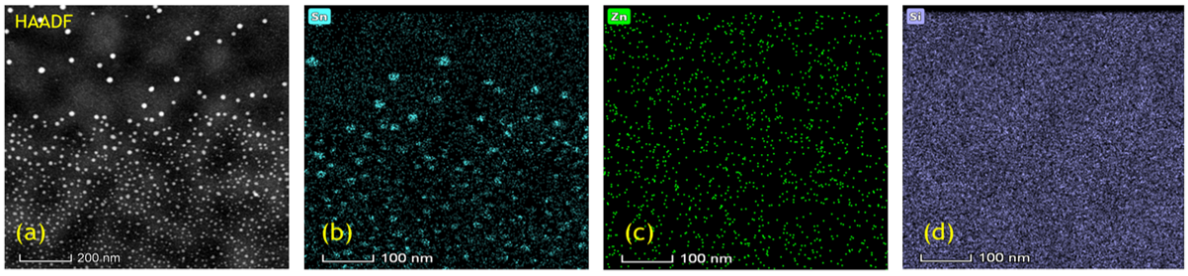

(a) HAADF image at mid-temperature range where the Sn concentration relatively peaks. The intensity counts of elements (b) Sn (c) Zn (d) Si

Figure 3.6: HAADF images at mid-temperature range where the Sn concentration relatively peaks. The intensity counts of elements (b) Sn (c) Zn (d) Si

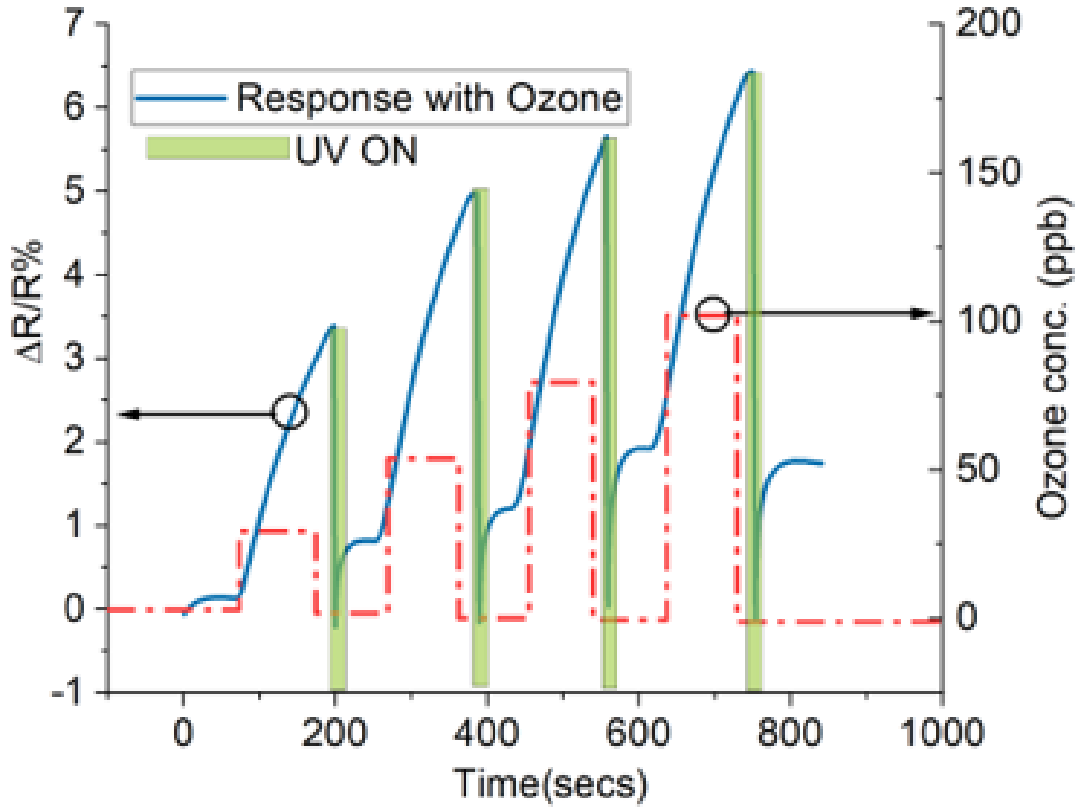

Figure 3.7: Room temperature response with ozone from sensor annealed at 600 °C

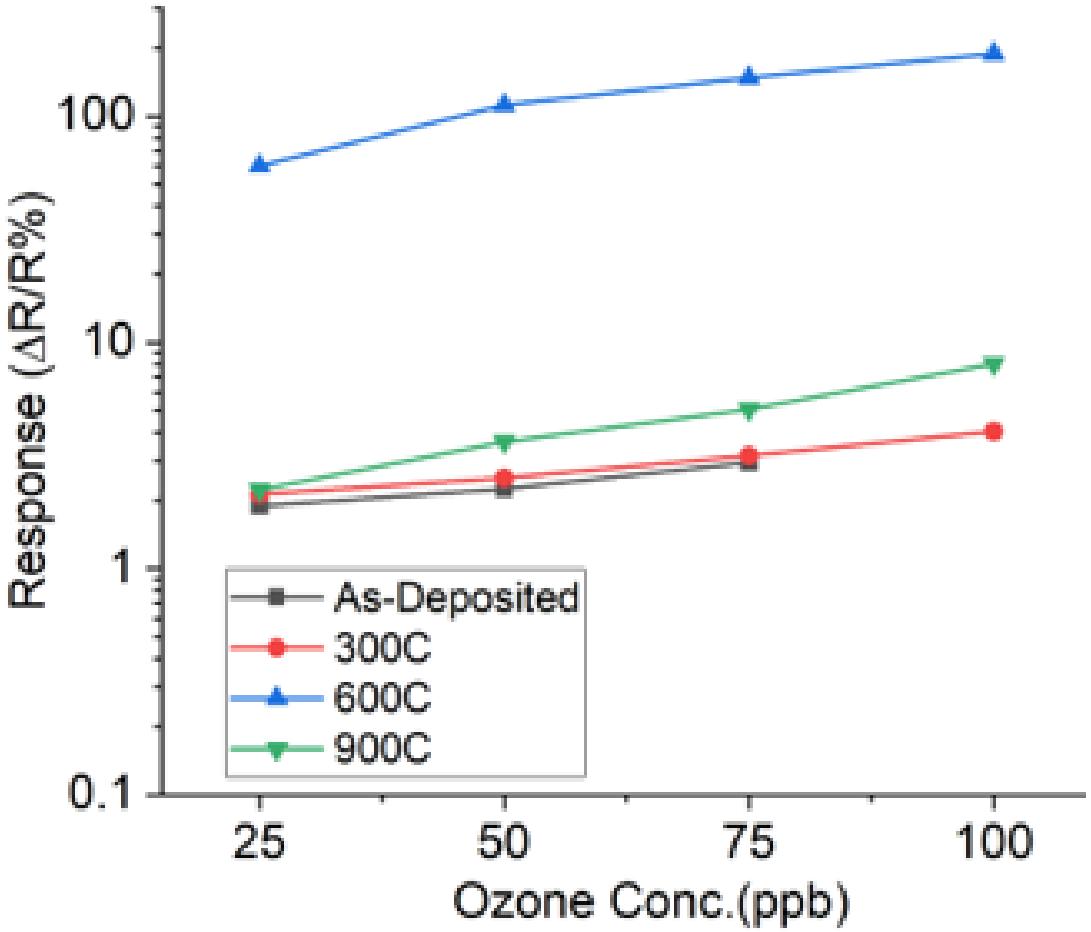

Figure 3.8: Responses with ozone from sensors annealed at various temperatures obtained at an operating temperature of 200 °C

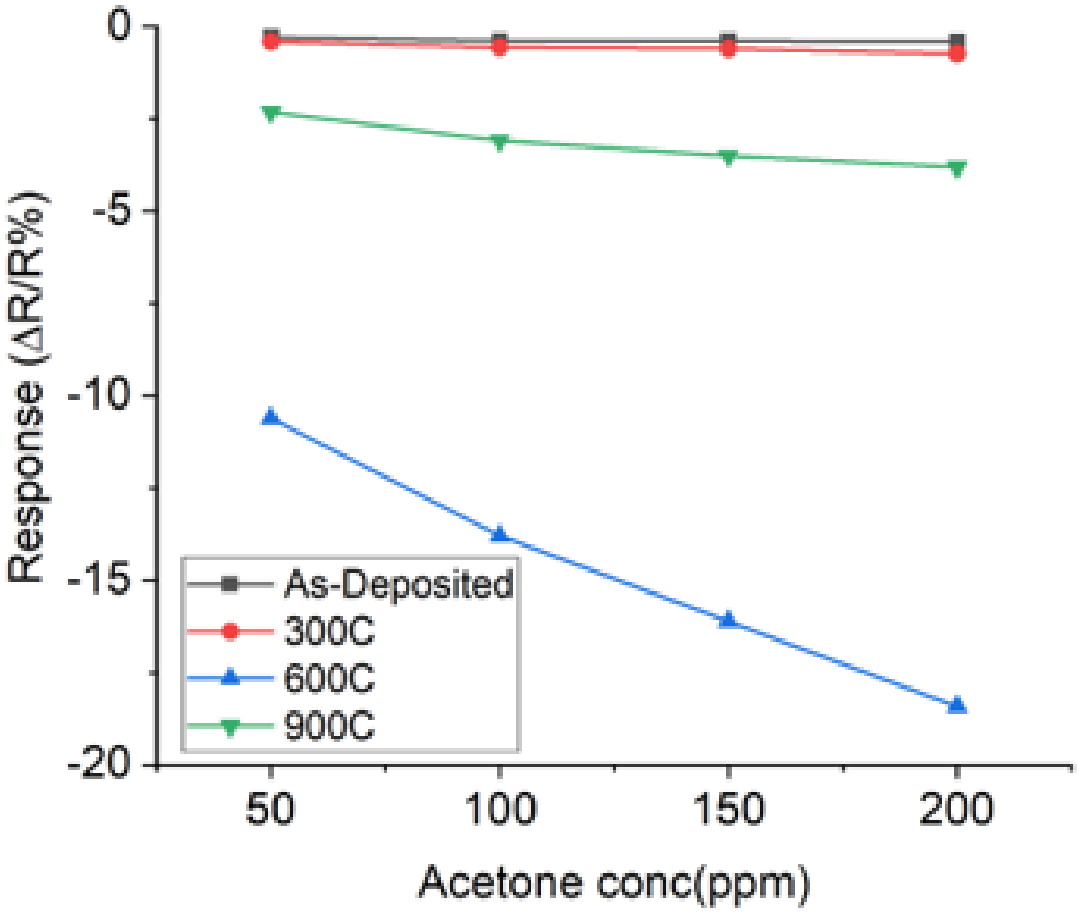

Figure 3.9: Responses with acetone from sensors annealed at various temperatures obtained at an operating temperature of 200 °C

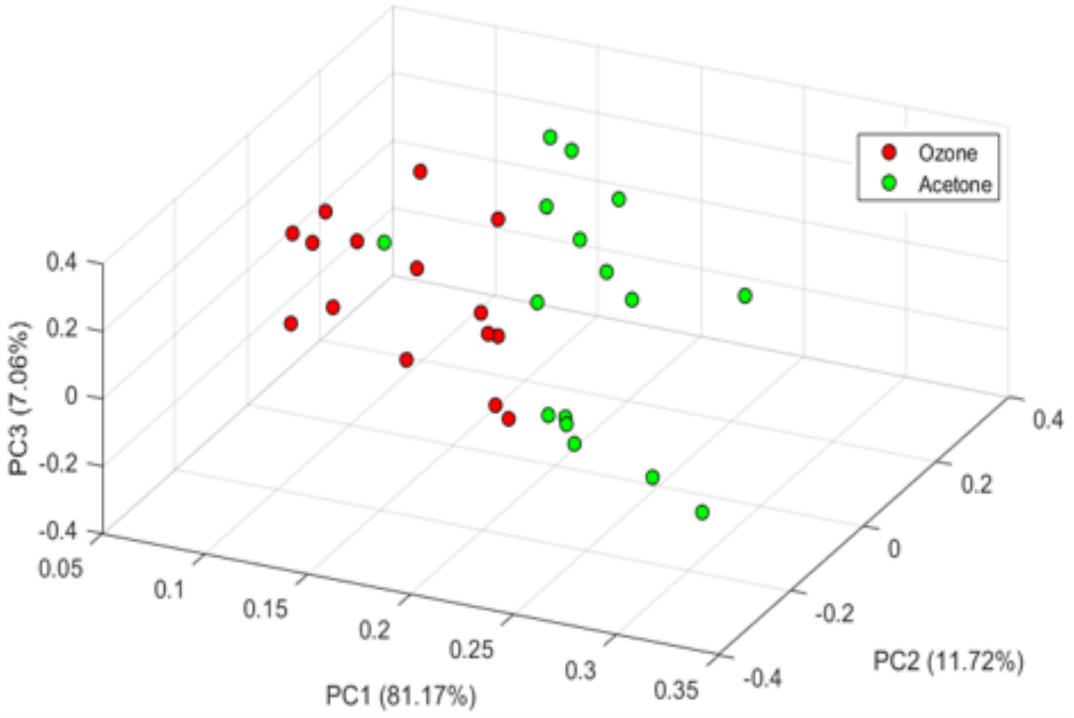

Figure 3.10: PCA obtained from all composite sensor components with ozone and acetone. 99.4% of variance accounted with first 3 components

As-Deposited, 300°C, 600°C, 900°C- annealed samples were tested with Ozone and Acetone at a temperature of 200°C(Fig.3.8 and Fig.3.9). This operating temperature of our sensors can further be reduced to room temperature by optimizing the thickness of the composite film, to the thickness range of Debye length as demonstrated in our previous work [35]. At 200°C, varying response magnitudes with change in gas and their concentrations were seen as desired from a typical sensor array. Typical response as obtained with ozone with 600°Cannealed sample is shown in Fig.3.7. Sensors annealed at 600°C, 900°Cshowed higher response magnitude which could be attributed to crystallinity and lower Si concentration as seen from Fig.3.3 and Table.3.1 respectively. Using Principal Component Analysis (PCA) the feature combinations with maximum variance from the vast uncorrelated information could be identified. To extract

the features of the gases, the response curve is smoothed, and the baseline is subtracted. From each segment, 28 distinctive features were extracted. 8 features extracted from pre-processed data were max and min settling times, ΔR between local maxima and minima, standard deviation, mean cycle of peaks and peak response values in gas-on and gas-off cycles. Another 20 features were extracted from the first and second order FFT derivatives of resistance. Three-dimensional components calculated from PCA (Fig.3.10) present well-separated clusters of the two gases with a very low mean square error (MSE) value of 1.25. The sum of the first three components accounted to 99.94% of the data, demonstrating the effectiveness of the used method.

3.2 FEM Design simulations MEMS heater array

As discussed in the previous section, the heating membrane in the monolithic sensor array needs to meet two primary objectives:
i) Increase ΔT to atleast 200°C in-between two adjacent strips with annealing, to achieve a wide range of crystallinity within the composites
ii) Enable continuous low power sensor operation of under 10 mW for heated sensor array operation of upto 200°C

In this study, detailed finite element models were used to design a heater membrane that meets the above two objectives. COMSOL Multiphysics was used for the FEM simulations. Simulations began by applying a voltage bias across a strip, which would then begin the Joule heating. The heat spreads from the strip to the rest of the chip via conduction, while the heat transfer from the strip to its ambient happens through convection and radiation. Models, equations and material parameters used for simulations are as described below where the

simulation iteratively solves for the heat, q and temperature, T.

The stationary state equation for heat transfer through conduction that was taken in the simulation was:

$$\rho C_p \frac{\partial T}{\partial t} + \rho C_p \boldsymbol{u}.\nabla T + \nabla.\boldsymbol{q} = Q \tag{3.1}$$

$$\boldsymbol{q} = -k\nabla T \tag{3.2}$$

Where

- ρ (SI unit: kg/m3) is the solid density.
- C_p (SI unit: J/(kg·K)) is the solid heat capacity at constant pressure.
- k (SI unit: W/(m·K)) is the solid thermal conductivity (a scalar or a tensor if the thermal conductivity is anisotropic).
- u (SI unit: m/s) is the velocity field defined by the Translational Motion subnode when parts of the model are moving in the material frame.
- Q (SI unit: W/m3) is the heat source (or sink).

For Convective heat flux across the boundaries of the microheater an external natural convection model was used which was given by

$$-\boldsymbol{n}.\boldsymbol{q} = q_0 \tag{3.3}$$

$$q_0 = h.(T_{ext} - T) \tag{3.4}$$

where

- q_0 is the heat flux
- h is the heat transfer coefficient

For surface to ambient radiation from all boundaries, the stationary equation used was

$$-\boldsymbol{n}.\boldsymbol{q} = \varepsilon\sigma(T_{amb}^4 - T^4) \tag{3.5}$$

where

- ε is the surface emissivity
- σ is the Stefan-Boltzmann constant
- T_{amb} is the ambient temperature

Ambient temperature and temperature at silicon base were defined to be at 293.15K. Absolute pressure was 1 atm.

Initial simulation:

The structure that was constructed started with a silicon base, followed by layers of silicon oxide, nitride and oxide again as for both electric and thermal insulation. The heater layer was of platinum. The material parameters for all the materials are as in Table 3.2 through Table 3.5

Table 3.2: List of Silicon material parameters used in simulations

Property	Variable	Unit	Value
Heat capacity at constant pressure	C_p	$J/(kg*K)$	700
Density	ρ	kg/m^3	2329
Thermal conductivity	k	$W/(m*K)$	130
Electrical conductivity	σ	S/m	1000
Coefficient of thermal expansion	α	$1/K$	2.6e-6
Relative permittivity	ε_r	1	11.7
Young's modulus	E	Pa	170e9
Poisson's ratio	nu	1	0.28

Table 3.3: List of Silicon Dioxide material parameters used in simulations

Property	Variable	Unit	Value
Heat capacity at constant pressure	C_p	$J/(kg*K)$	730
Density	ρ	kg/m^3	2200
Thermal conductivity	k	$W/(m*K)$	1.4
Electrical conductivity	σ	S/m	1
Coefficient of thermal expansion	α	$1/K$	0.5e-6
Relative permittivity	ε_r	1	4.2
Young's modulus	E	Pa	70e9
Poisson's ratio	nu	1	0.17

A bias of 4V has been applied across the central strip and the simulations ran until they reached steady state. The 3D view simulated surface temperature profile is shown in 3.11, 2D view showing variation across the heater membrane only is presented in 3.12 with an horizontal and vertical sweep as displayed by the green and blue lines in 3.12 are shown in 3.13.

Table 3.4: List of Silicon Nitride material parameters used in simulations

Property	Variable	Unit	Value
Heat capacity at constant pressure	C_p	$J/(kg*K)$	700
Density	ρ	kg/m^3	3100
Thermal conductivity	k	$W/(m*K)$	20
Electrical conductivity	σ	S/m	1
Coefficient of thermal expansion	α	$1/K$	2.3e-6
Relative permittivity	ε_r	1	9.7
Young's modulus	E	Pa	250e9
Poisson's ratio	nu	1	0.23

Table 3.5: List of Platinum material parameters used in simulations

Property	Variable	Unit	Value
Heat capacity at constant pressure	C_p	$J/(kg*K)$	133
Density	ρ	kg/m^3	21450
Thermal conductivity	k	$W/(m*K)$	71.6
Electrical conductivity	σ	S/m	8.9e4
Coefficient of thermal expansion	α	$1/K$	8.8e-6
Relative permittivity	ε_r	1	1.49
Young's modulus	E	Pa	168e9
Poisson's ratio	nu	1	0.38

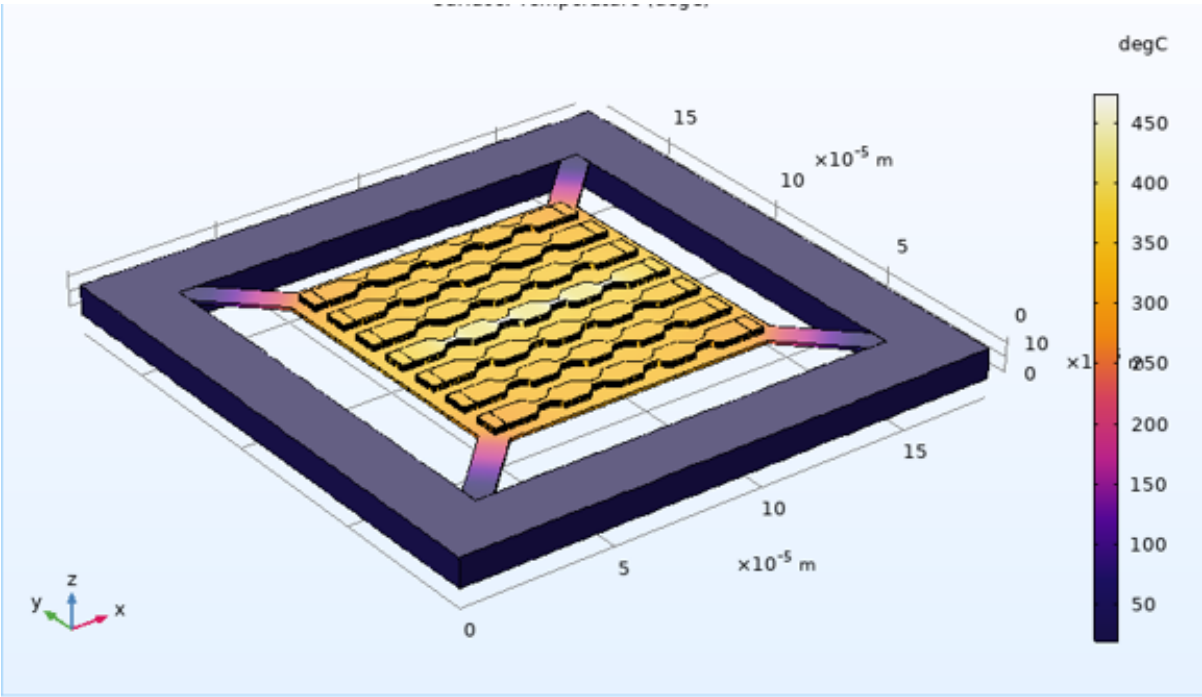

Figure 3.11: 3D view of simulated design with constrictions

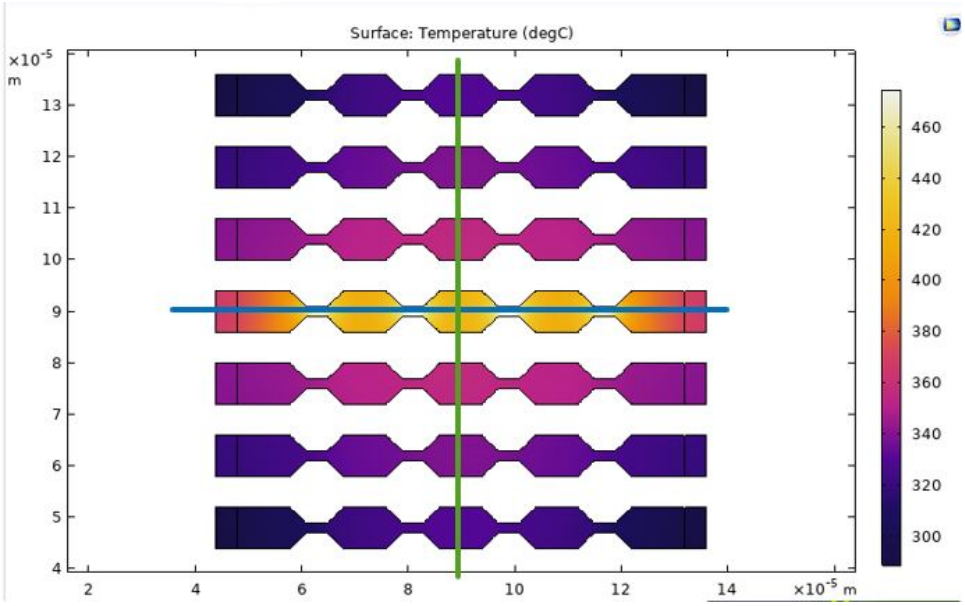

Figure 3.12: 2D view of simulated design with constrictions

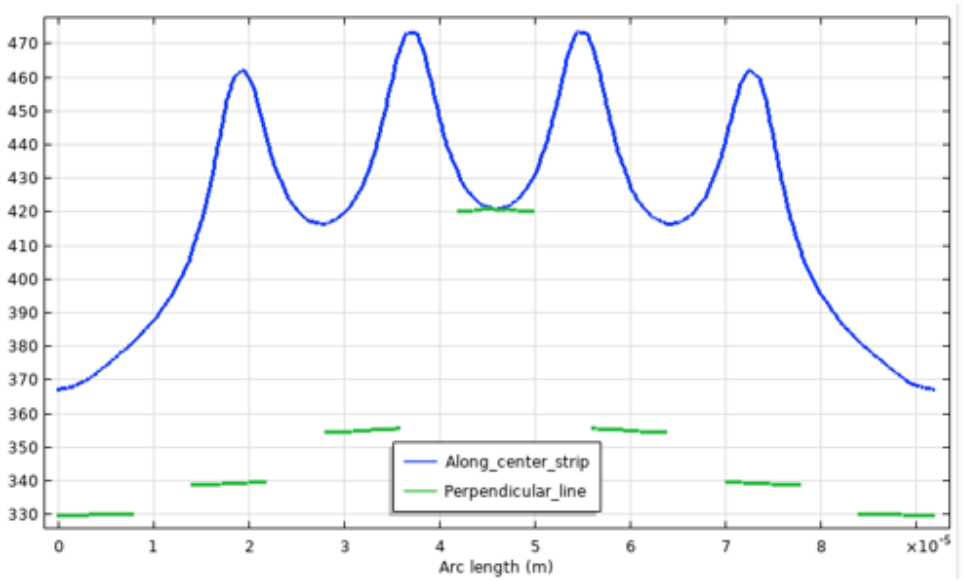

Figure 3.13: Horizontal and vertical sweeps of heat profiles across the heater strips

For further simulations until mentioned, just the same simulation conditions as above for comparing with a reference and design changes were made incrementally by changing various elements to produce a temperature profile and power numbers as laid out in the objectives before.

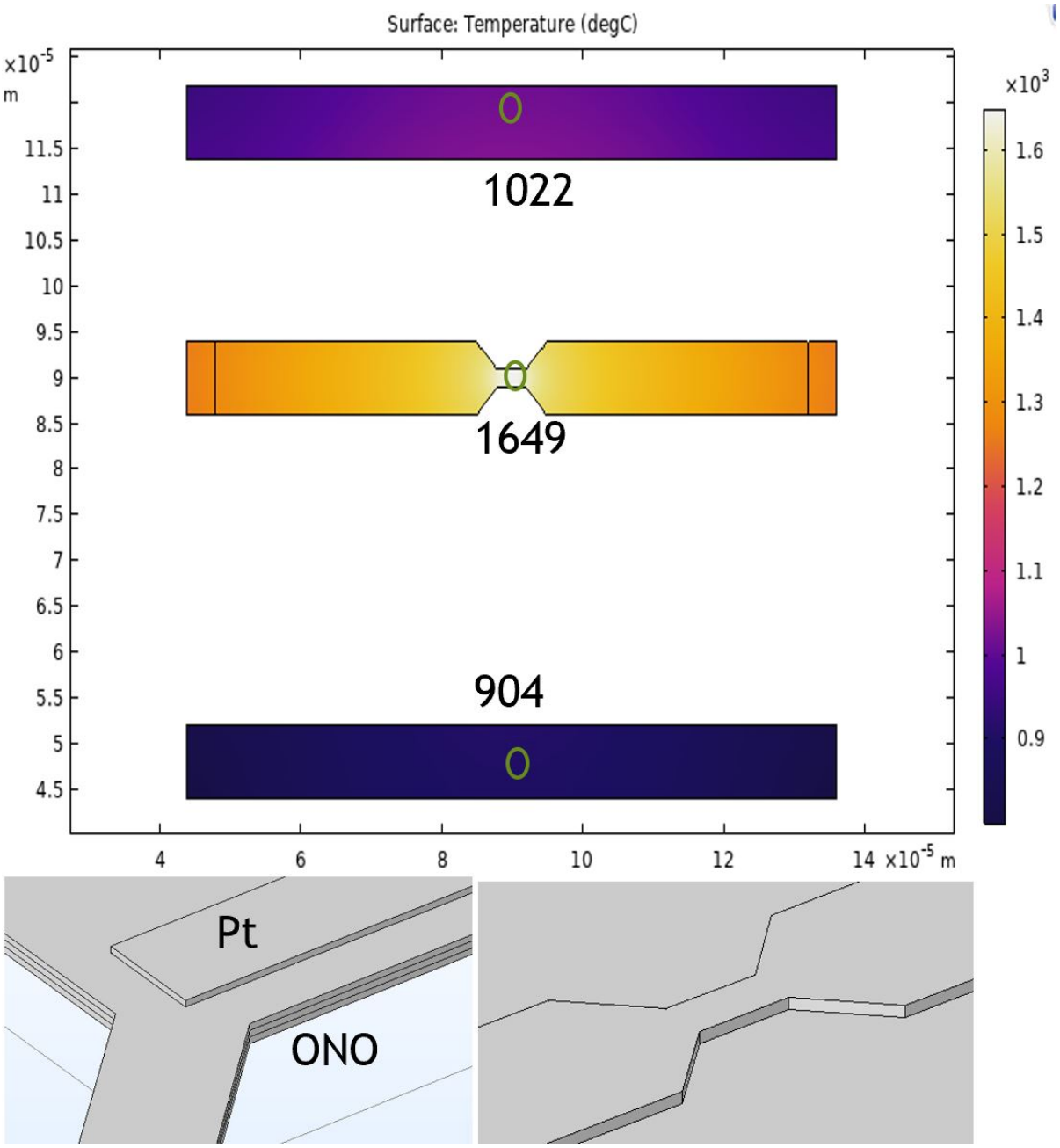

Figure 3.14: Design with asymmetrical strips and a just a center constriction with an unetched membrane

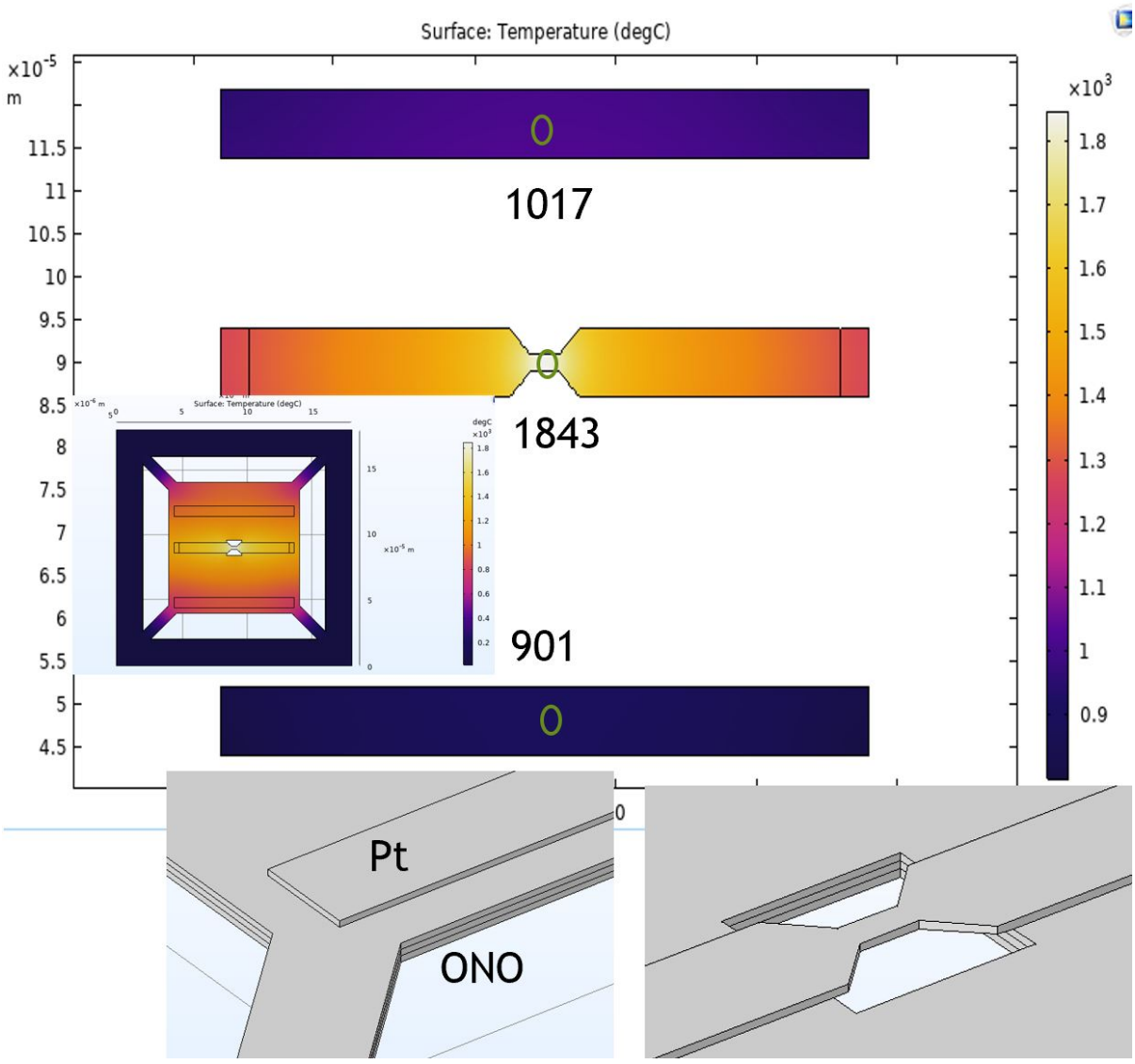

Figure 3.15: Design with just a center constriction with a rectangular hole etched around the constriction in the membrane

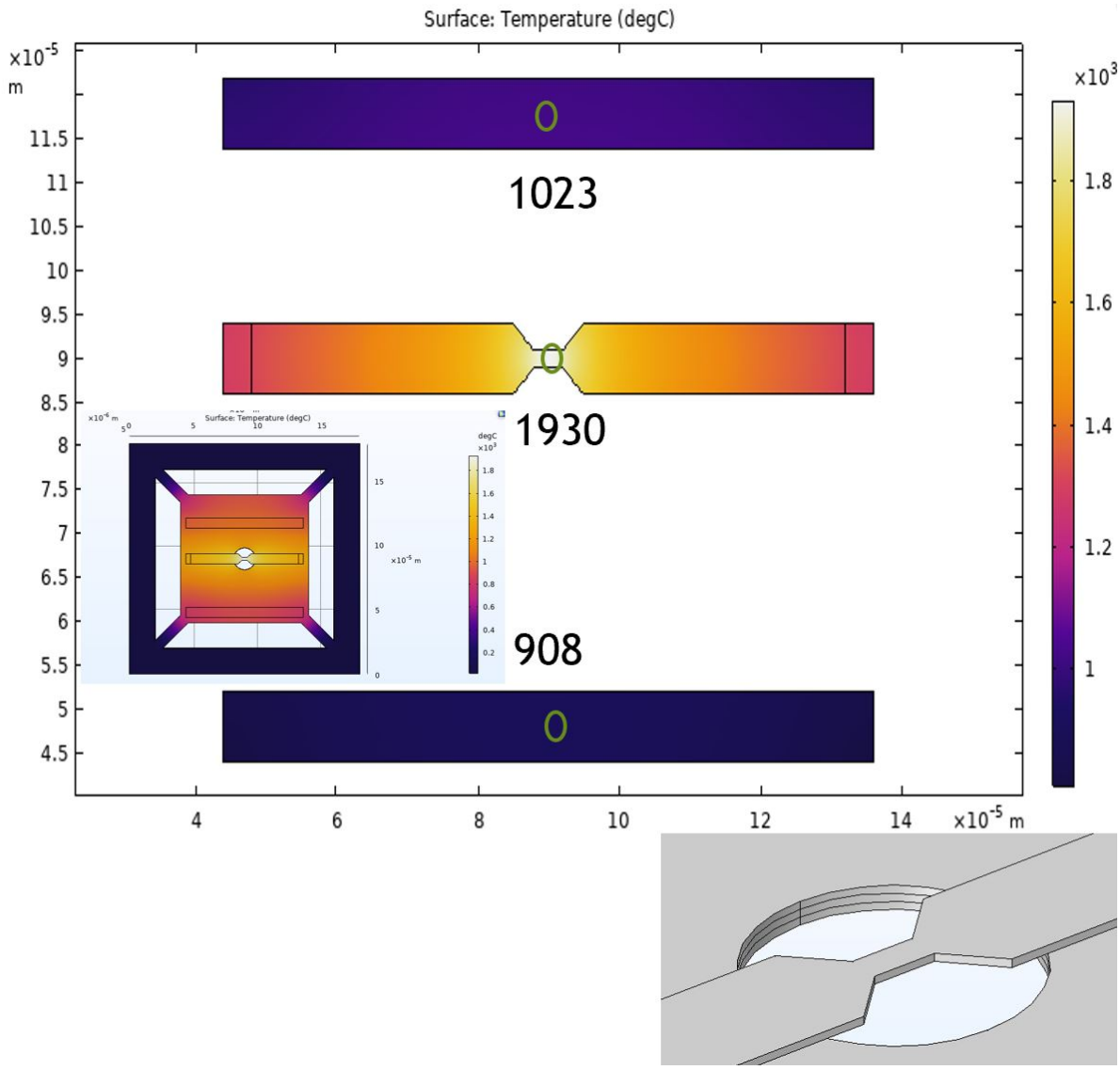

Figure 3.16: Design with just a center constriction with a circular hole etched around the constriction in the membrane

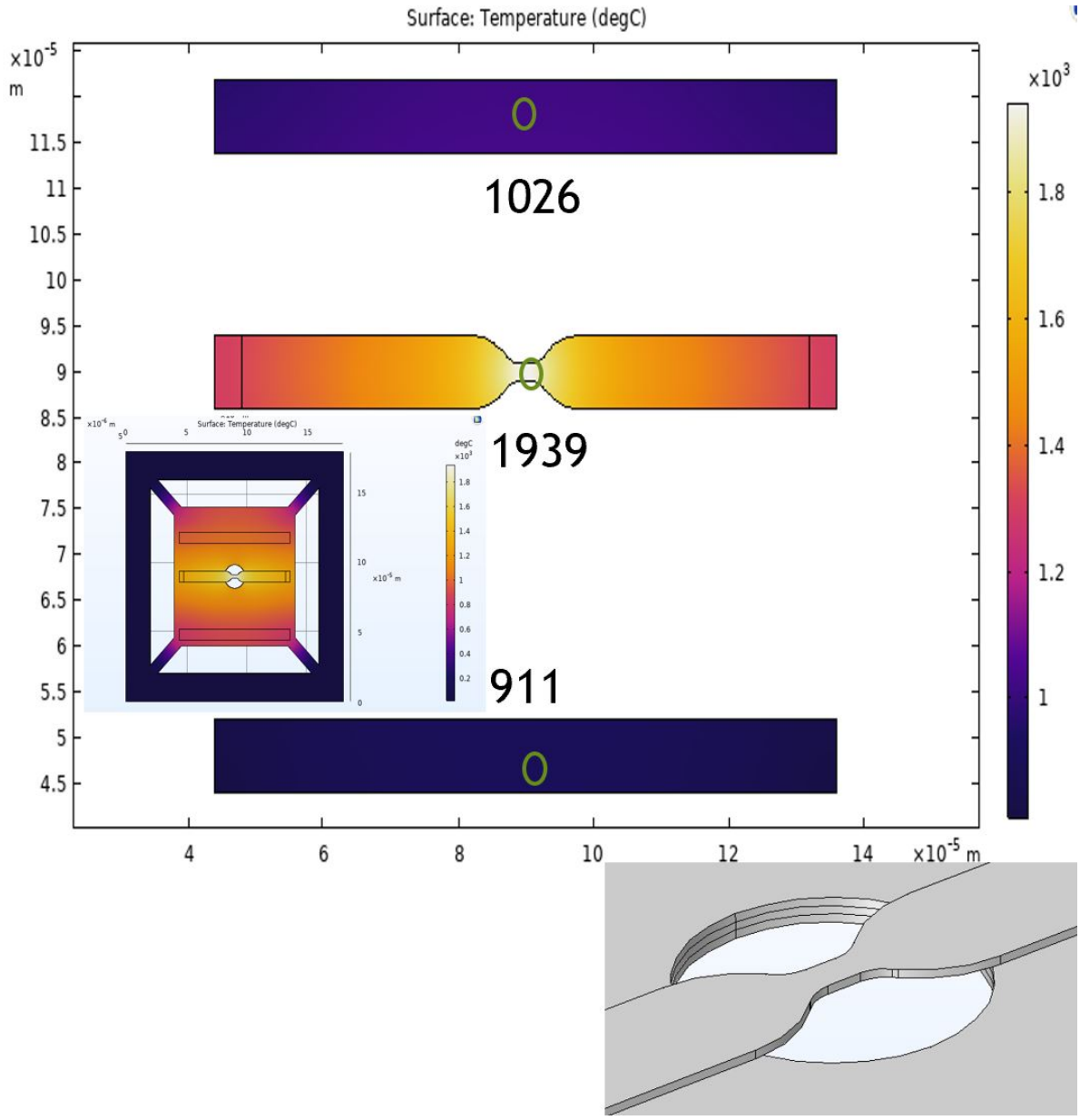

Figure 3.17: Design with just a center constriction with a circular hole etched around the constriction in the membrane, plus a tapered constriction

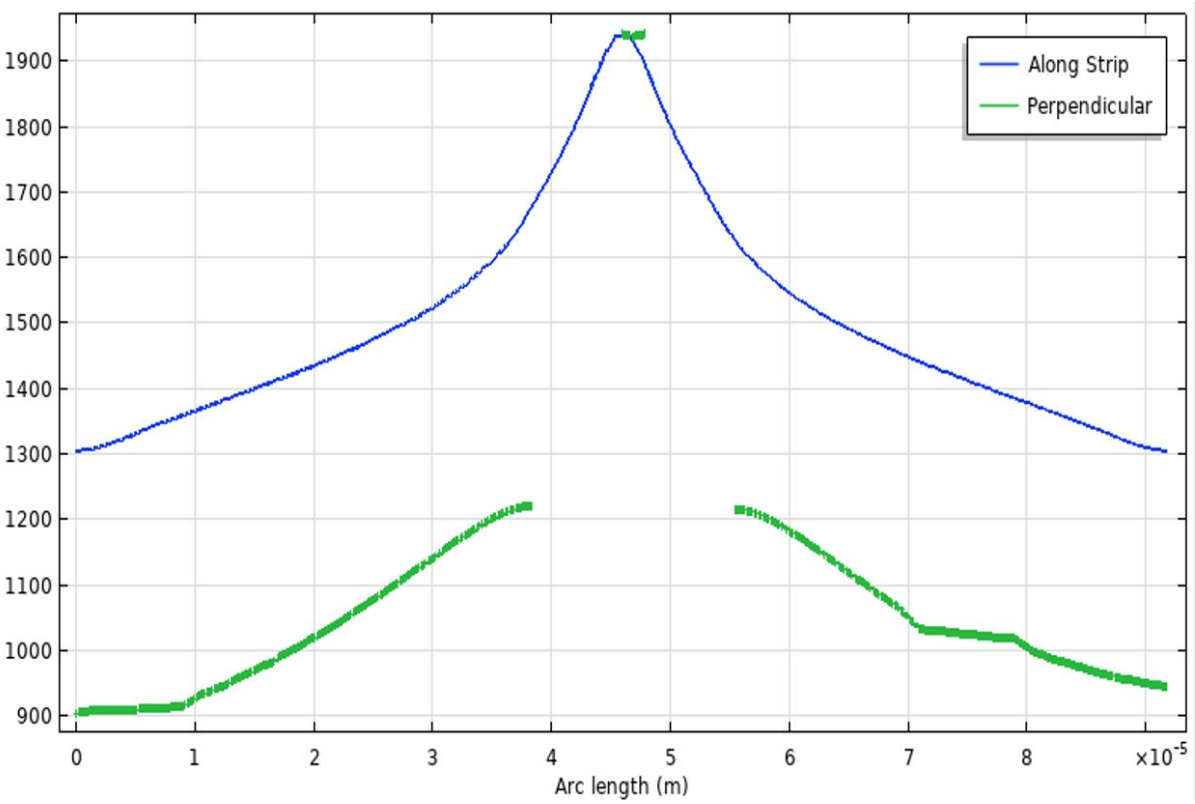

Figure 3.18: Horizontal and vertical temperature profile sweep across the membrane

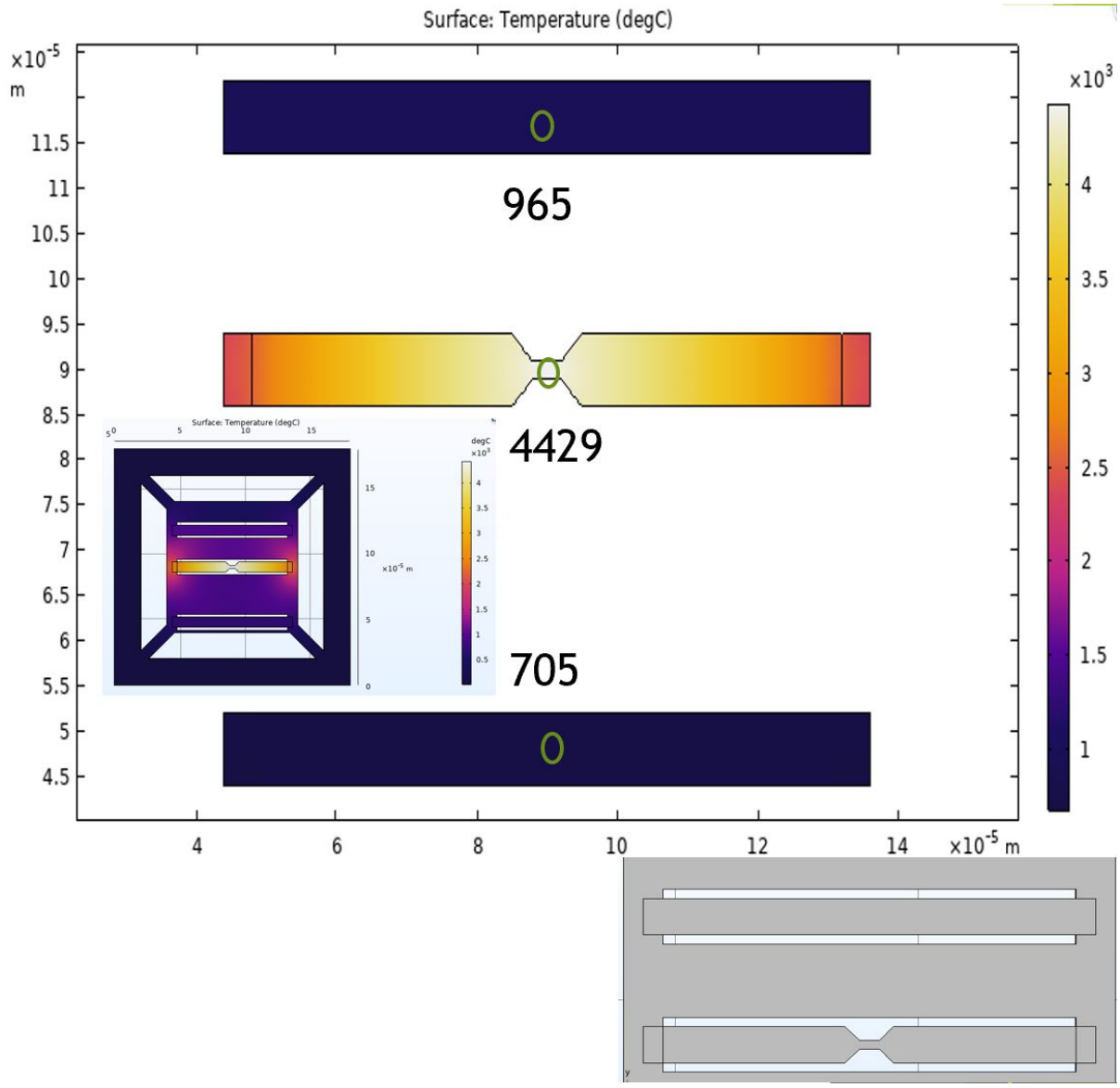

Figure 3.19: Design with membrane being rectangular sections etched around the entire heater strip, with central constriction

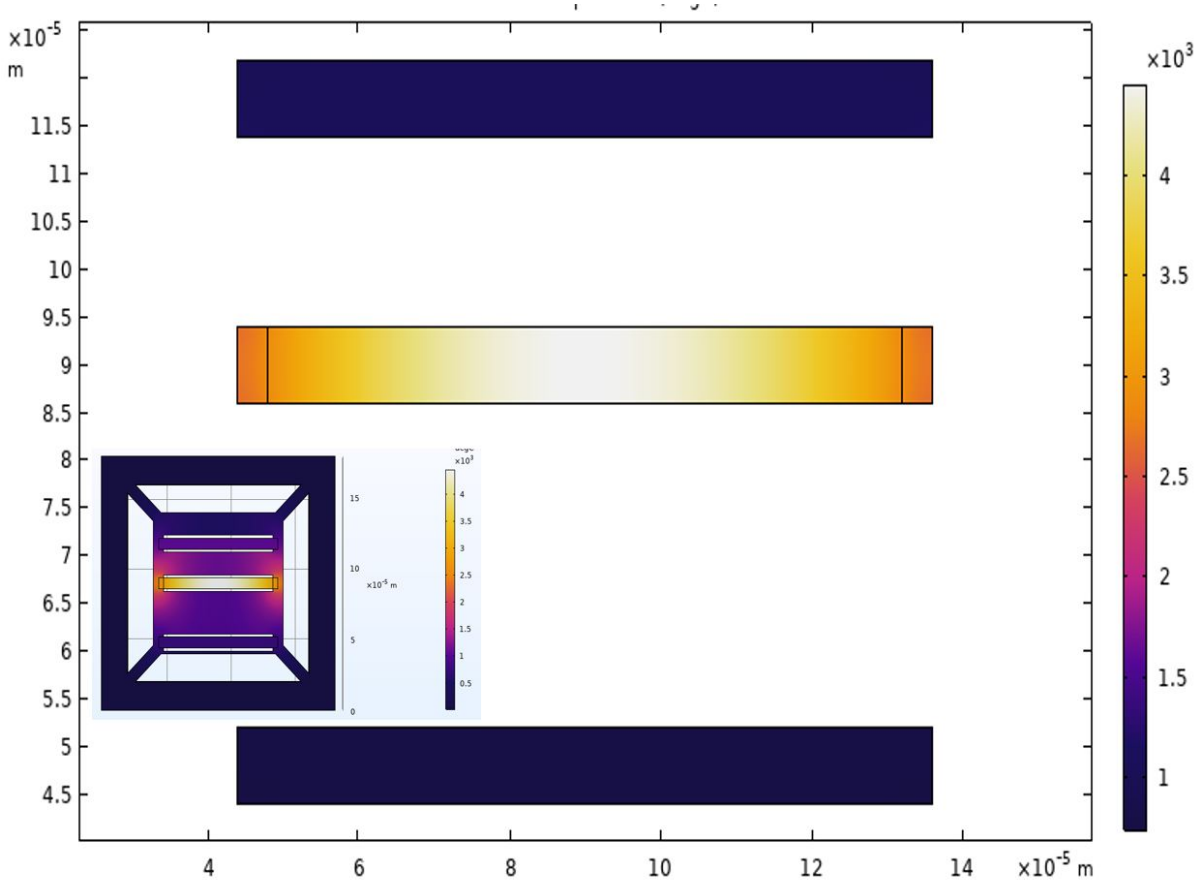

Figure 3.20: Design with membrane being rectangular sections etched around the entire heater strip, without central constriction

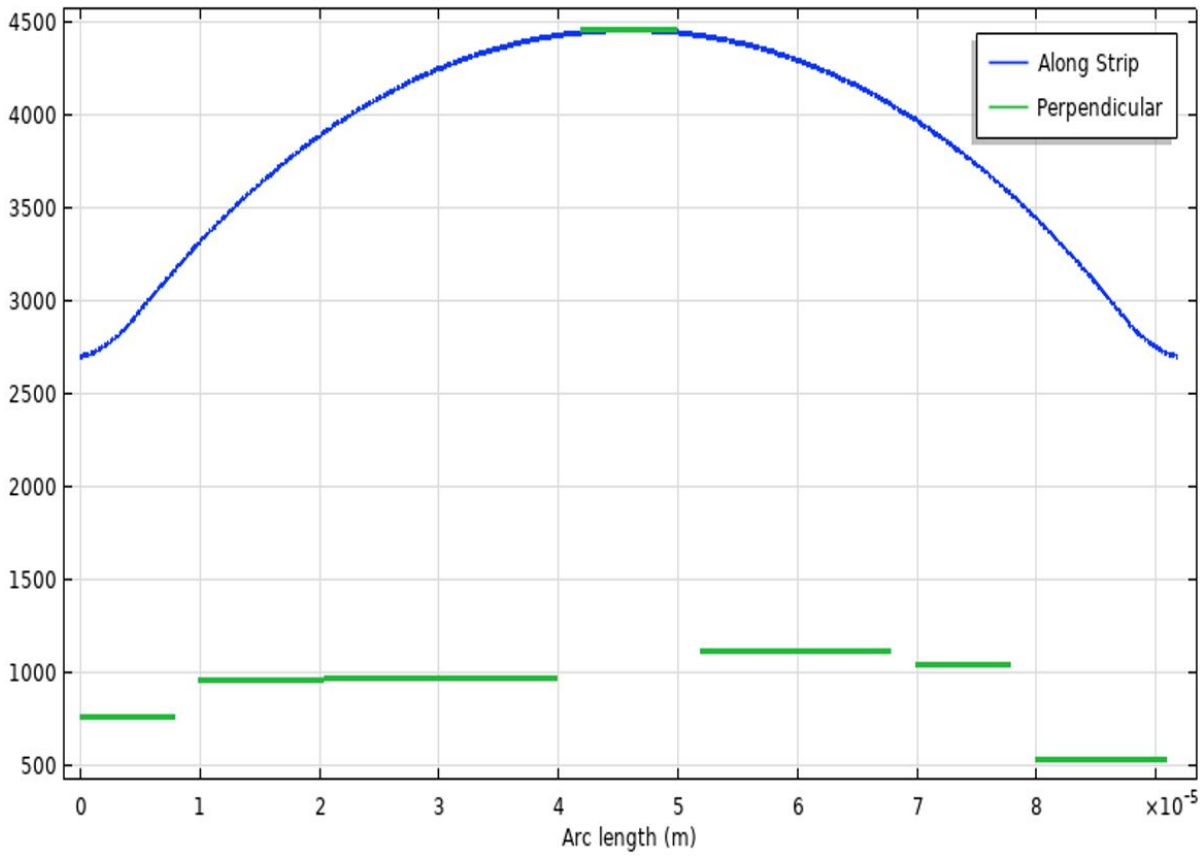

Figure 3.21: Horizontal and vertical temperature profile sweep across the membrane

Combining different elements we could see that design as in Fig.3.17 and a Fig.3.20 come closer to meeting the objectives laid out in the beginning. Fig.3.20 has been modified a bit in Fig.3.25 as constriction doesn't seem to have an effect when the strip is entirely isolated through etching. Though the simulations until here had a constant bias of 4V to draw comparisons between various design aspects, now the bias has now been reduced to reach annealing temperatures of upto 900°C.

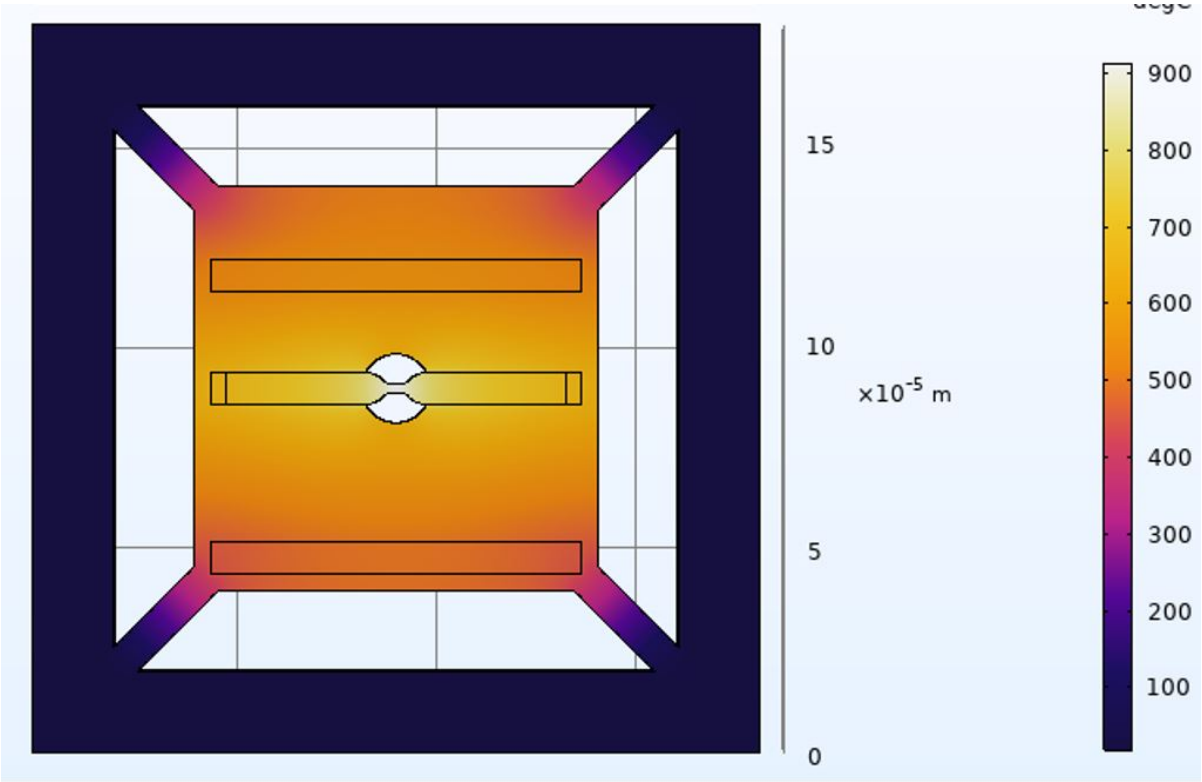

Figure 3.22: Reducing the voltage bias applied to 2.5 V instead of 4 V. The temperature at the center of strip reached upto 900°C as could be seen in 3.23 below

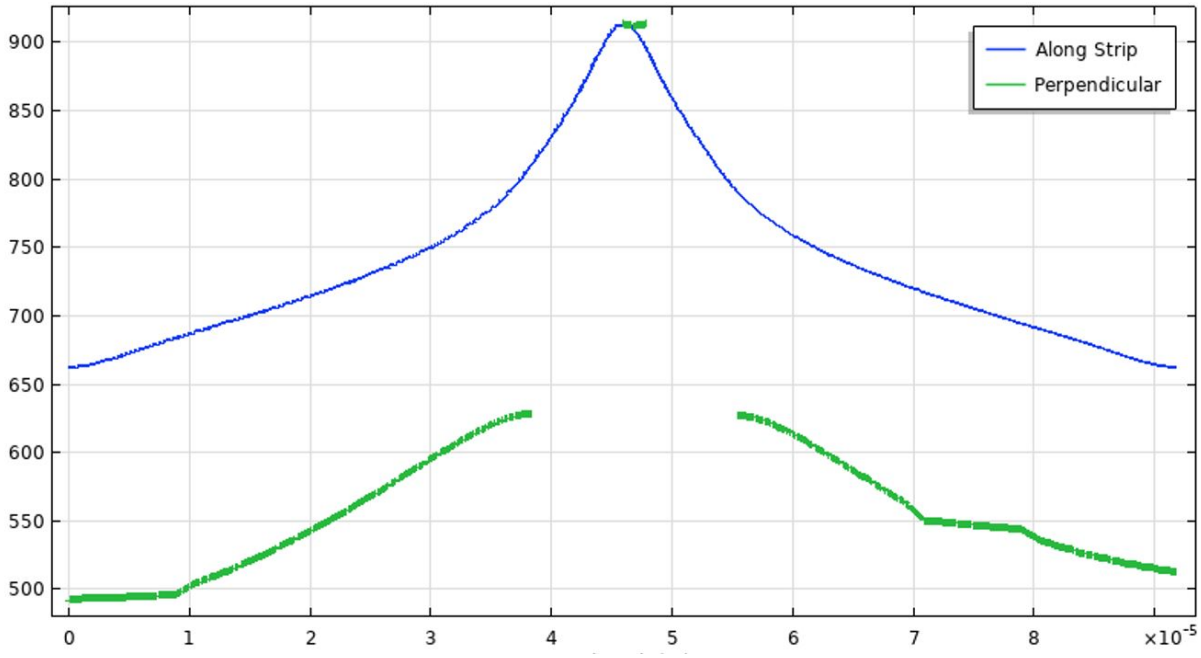

Figure 3.23: Horizontal and vertical temperature profile sweep across the membrane of 3.22

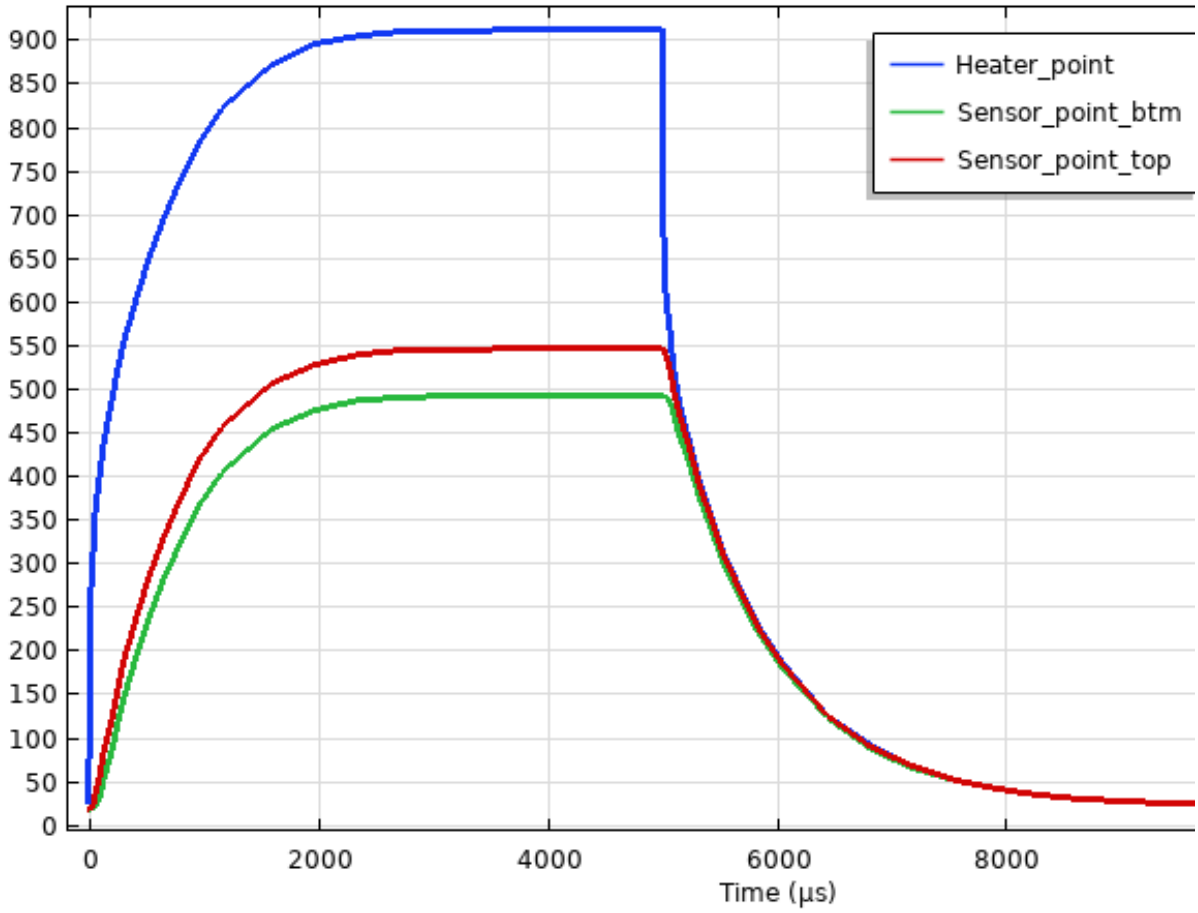

Figure 3.24: Heating and cooling times for various points across the membrane. The blue line is at the center of constriction on top of heater, green line is for the center of bottom strip and red line is for the center of bottom strip. We can see the heating an cooling times are under 5 ms.

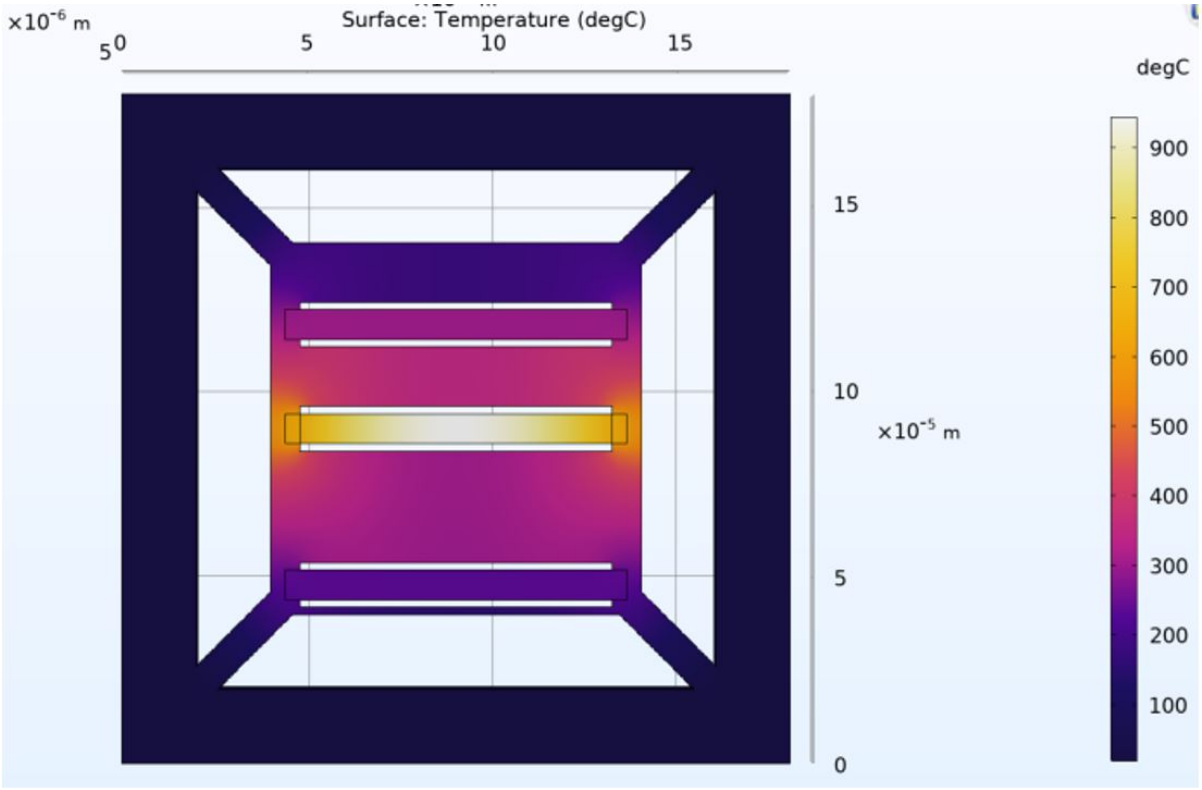

Figure 3.25: Reducing the voltage bias applied to 1.4 V instead of 4 V. The temperature at the center of strip reached upto 945°C as could be seen in 3.27 below

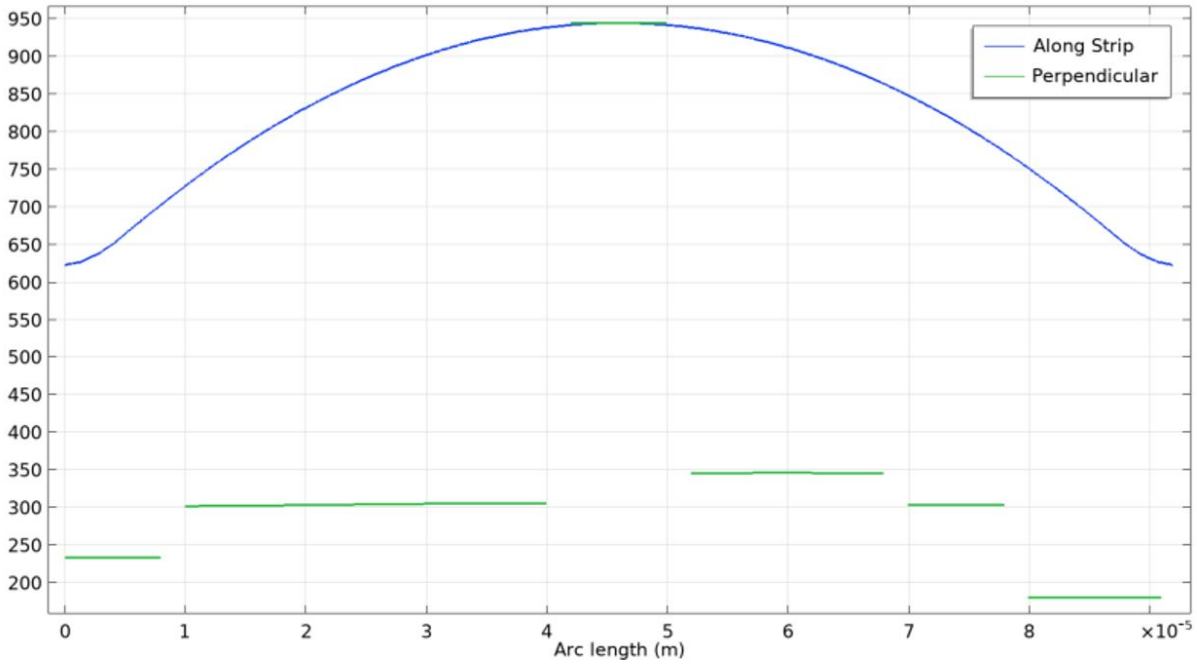

Figure 3.26: Horizontal and vertical temperature profile sweep across the membrane of 3.25

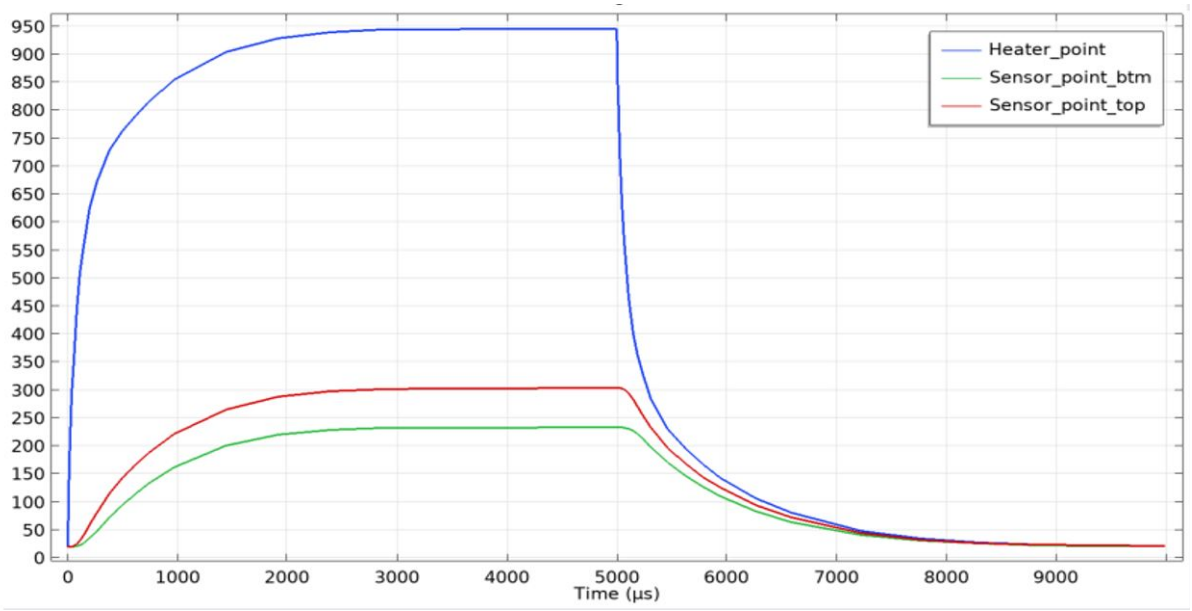

Figure 3.27: Heating and cooling times for various points across the membrane. The blue line is at the center of constriction on top of heater, green line is for the center of bottom strip and red line is for the center of bottom strip.

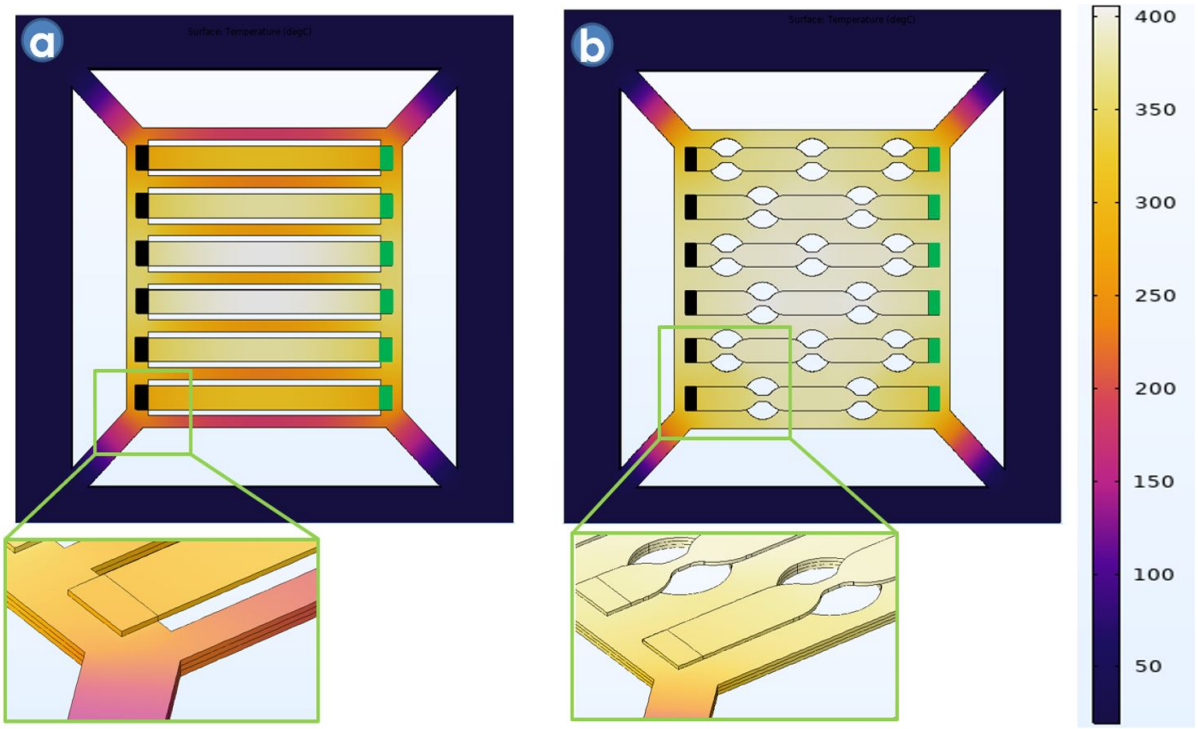

Figure 3.28: Fig.3.22 & Fig.3.25 have been modified to increase the number of sensors per membrane

The final designs bring the power of the microheaters to 6.3 mW and 11.7 mW for designs (a) and (b) respectively to reach a peak temperature of 400°C. While design (a) has a wider sensing area, wider ΔT between adjacent strips and lower power, design (b) has less variation, more localization of heat across a given strip. Both the designs give a good starting point for fabrication and the electrical characterization post that can help us evaluate the final design for the monolithic sensor array.

Table 3.6: Voltage applied and power consumed to reach 400°C for both microheater designs

	Design (a)	Design (b)
Voltage	0.5 V	0.85 V
Power consumption	6.3 mW	11.7 mW

Table 3.7: Temperature, Voltage and Power numbers comparison for microheater design (a)

Temperature	Voltage	Power
400°C	0.5 V	6.3 mW
100°C	0.25 V	1.58 mW

3.3 Microheater fabrication

In this section an additional contributing module to complete the picture of the design and development of monolithic sensor array is presented. A MEMS microheater is being fabricated by Yilu Zhou (fellow PhD student in our group) with final design parameters' input fed from the COMSOL simulations discussed in the previous section. While these fabrications are currently underway to get a generic microheater structure and the involved fabrications steps working, eventually these are intended to move towards the COMSOL simulations done above.

The fabrications steps are explained and arranged in order from Fig 3.29 through Fig 3.36. The fabrication first starts with a double side oxidized Si wafer, followed by evaporating Ti/Pt metal as a heater layer (Fig.3.29). The front side of heater layer is then masked with 400 nm of PECVD SiN (Fig.3.30). Photolithgraphy is now done on the backside to open the required window through SiO_2 hard mask, followed by a deep RIE to etch through Si (Fig.3.31). Most Si under the microheater is etched via this process while some of it is left to avoid overetching of SiO_2 on the front side . The left over etching is done by TMAH which has a very low etch rate with SiO_2 compared to Si (Fig.3.32). Contact holes were then etched on the front side of the wafer for electrical characterization of the heater (Fig.3.33 and Fig.**??**). And temperature readings were taken with an IR camera (Fig.3.35).

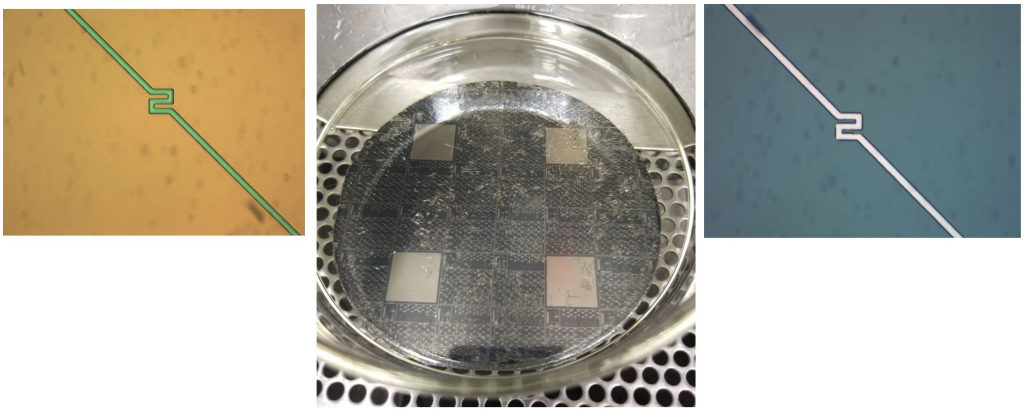

Figure 3.29: Heater Layer

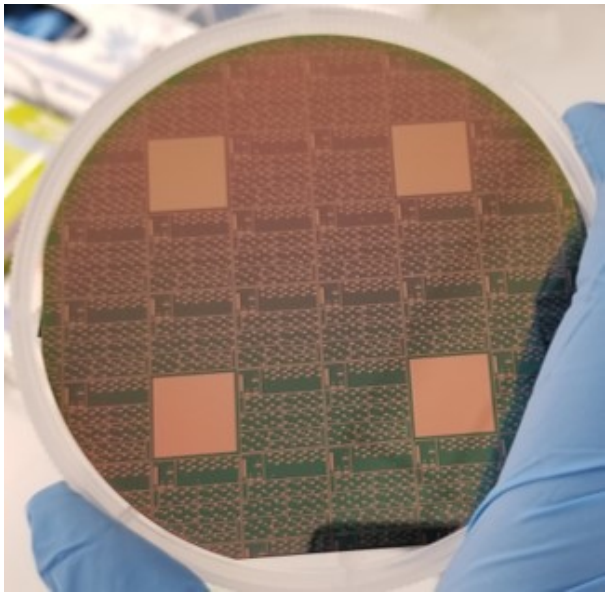

Figure 3.30: Protection Layer

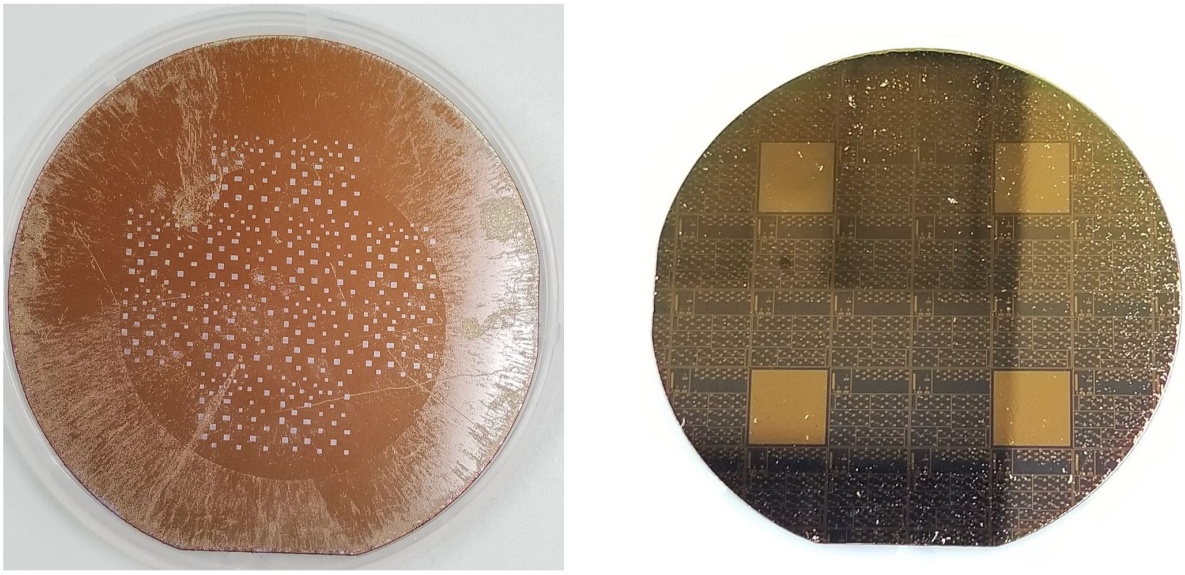

Figure 3.31: Etching Mask

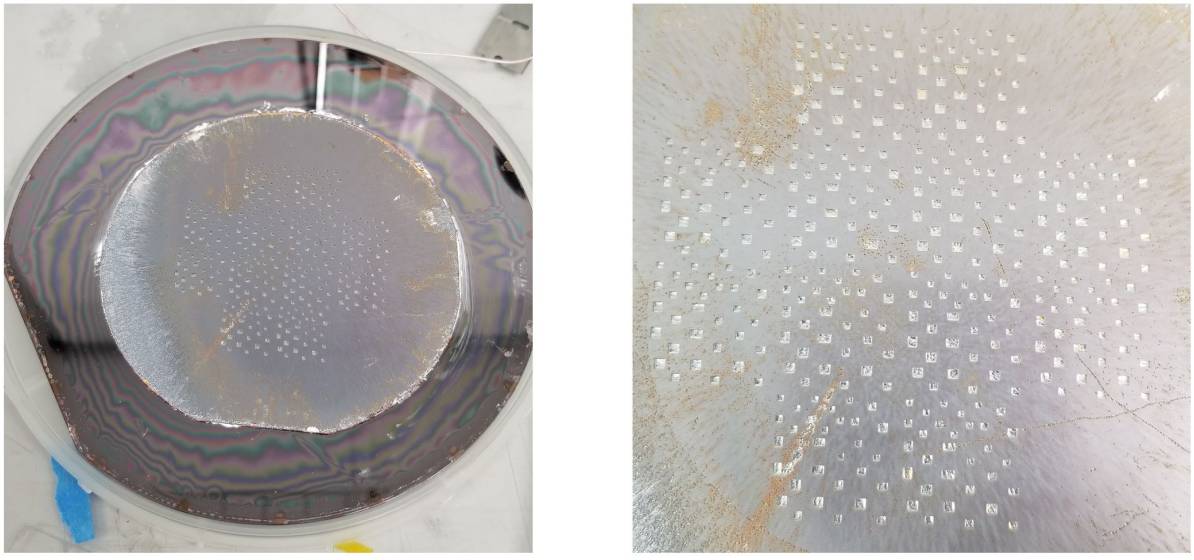

Figure 3.32: Etching process

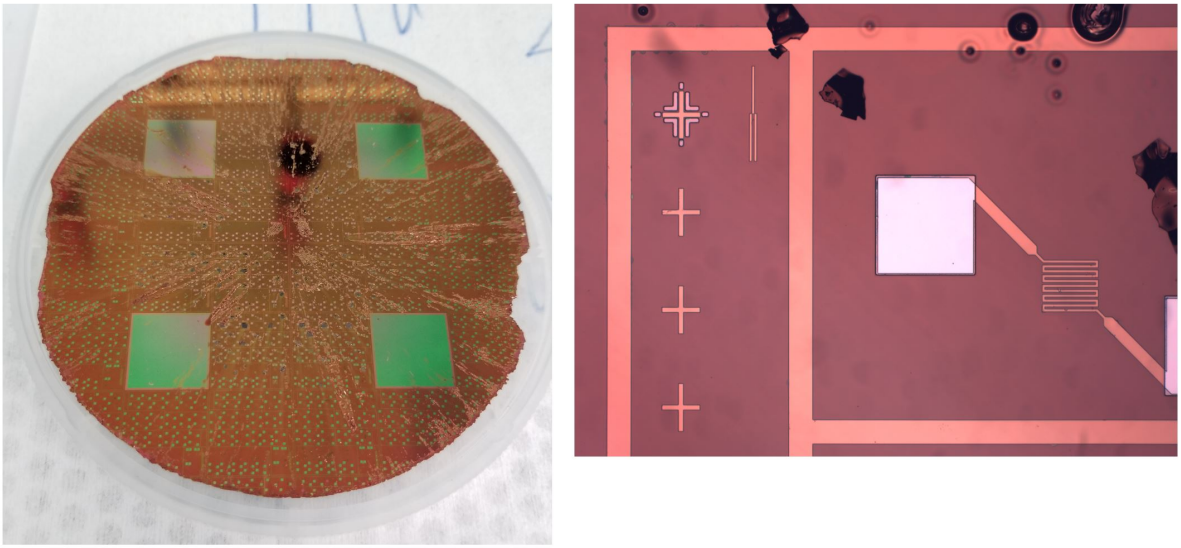

Figure 3.33: Heater electrode uncover

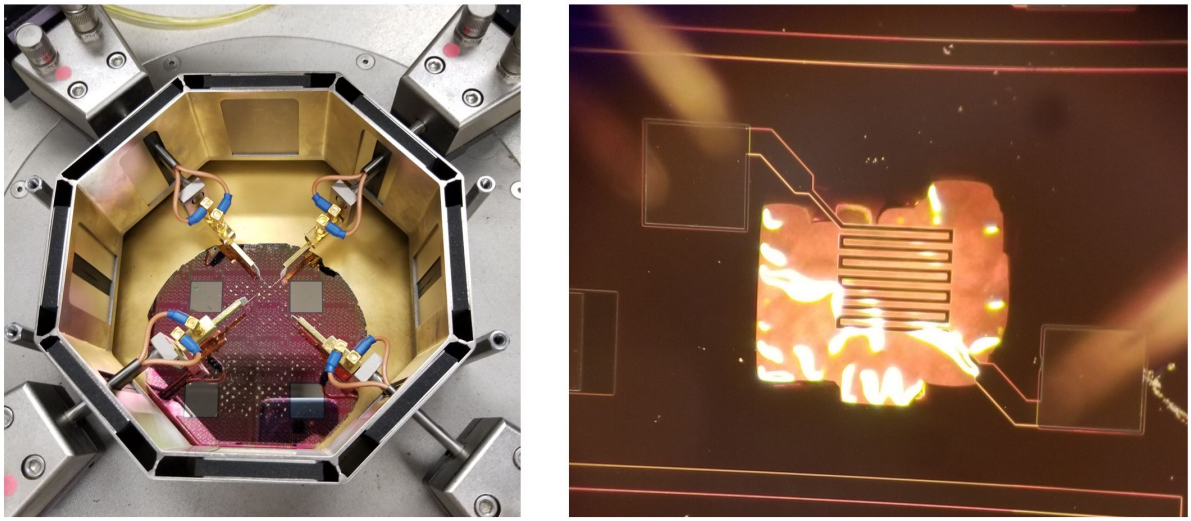

Figure 3.34: Characterization of sensor with microheater

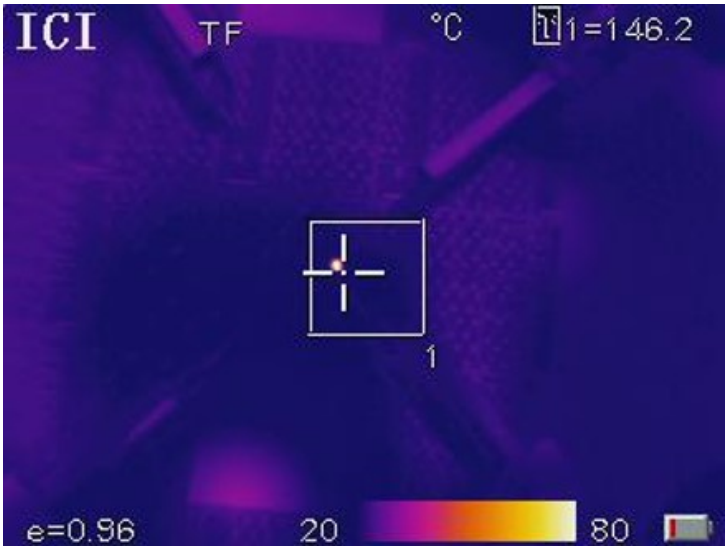

Figure 3.35: IR Camera image of microheater

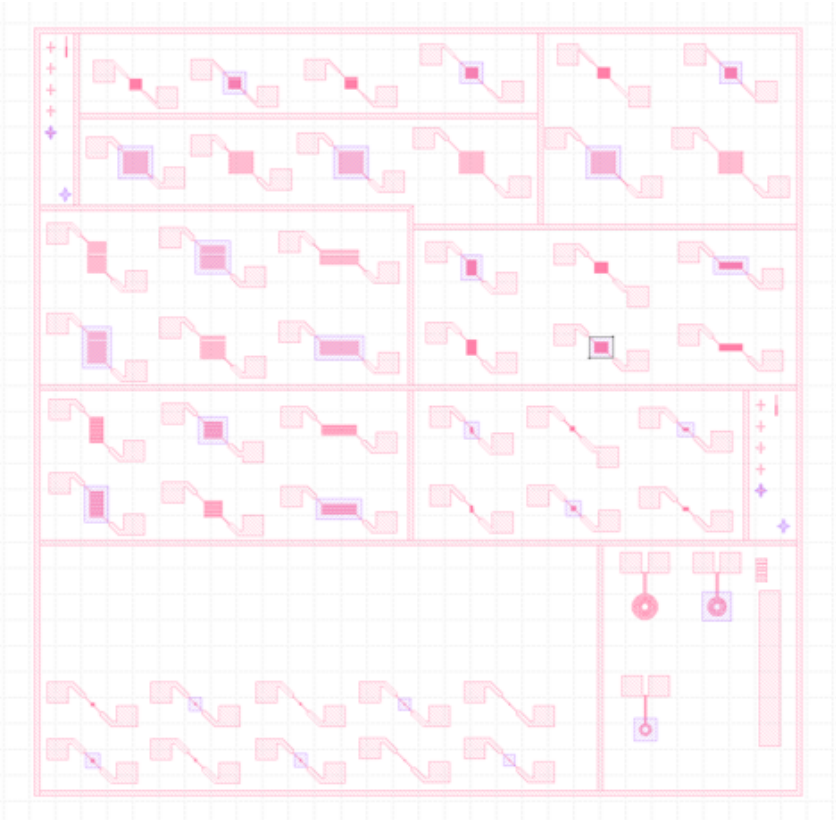

Figure 3.36: Design mask showing different heater designs currently being fabricated

Fig.3.36 shows the various heater designs currently being fabricated. Once the fabrication steps and procedure is sorted, this fabrication will converge with the FEM simulations done in Section 3.2.

3.4 Optimization and E-Nose performance of ALD sensors

This part of the work involved optimizing the sensor elements within the annealing range of the monolithic array concept. The goal here is to improve the response for a low temperature

operation of the sensing elements.

Towards this 3 different thickness combinations from 30 cycles to 100 cyles of ALD of both SnO_2 and ZnO sensing layers have been deposited. The thicknesses as measured from ellipsometer are 16 nm, 8 nm, 3.5 nm for 100, 50, 30 cycles of ZnO and 12 nm, 6 nm, 4.5 nm for 100, 50, 30 cycles of SnO_2. Then each of these composite sensing wafers have been diced and annealed at three different temperatures at 300°C, 600°C and 900 °C. Along with as-deposited diced, the three composite sensors at four annealing conditions produced a total of twelve sensors. All these four sensors were then operated at four operating temperatures - RT, 100°C, 150°C and 200°C with Ozone from 25 ppb to 100 ppb producing 48 data sets for all the four concentrations. The valuable features of these results are presented in Fig 3.37 and Fig 3.38

3.5 Optimization of constituent sensors

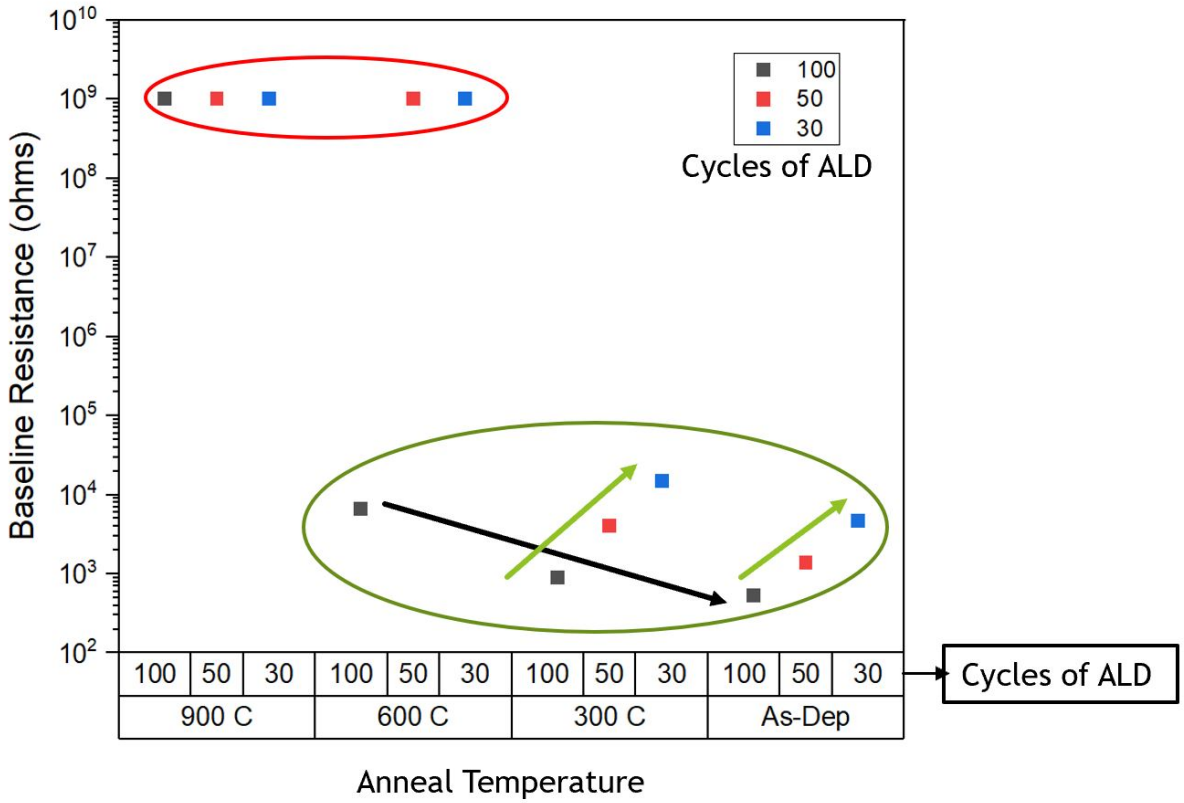

Figure 3.37: Baseline Resistance vs Anneal Temperature and Sensor Thickness, plotted for an operating temperature of 200°C

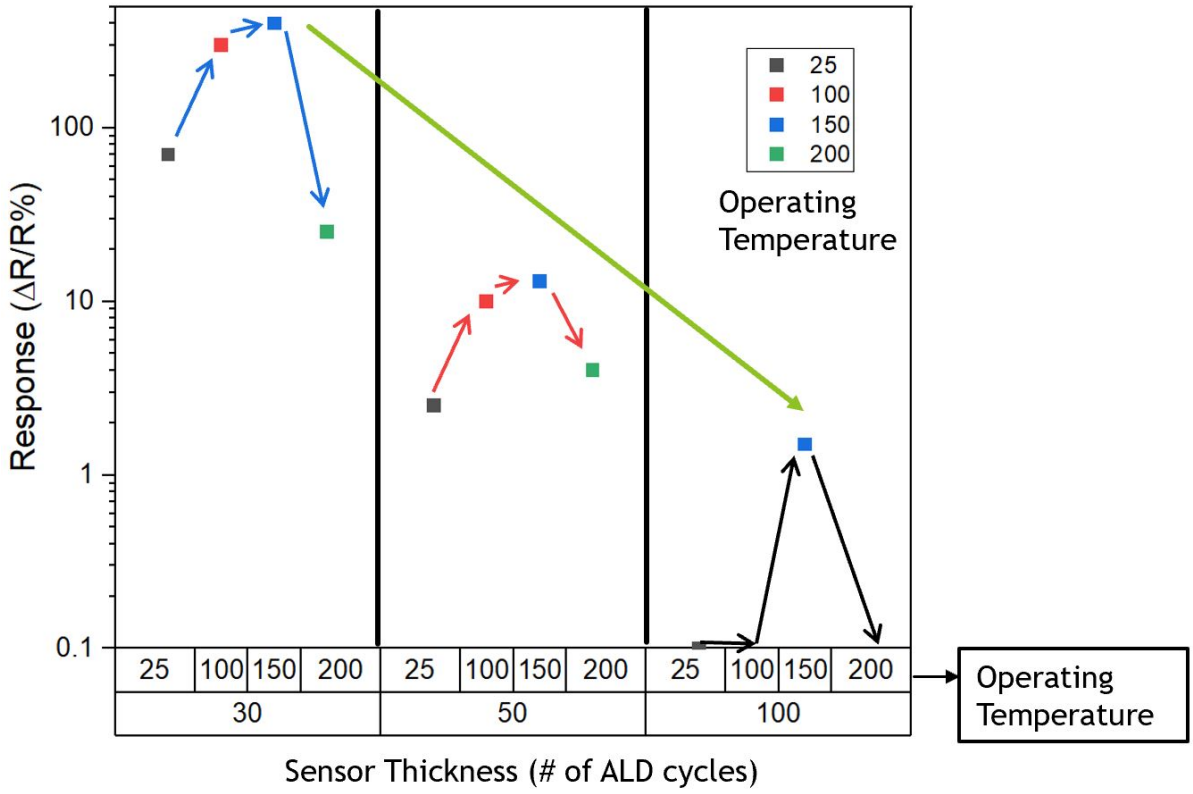

Figure 3.38: Response vs Operating Temperature and Sensor Thickness, plotted at an ozone conc. of 75 ppb and for all sensors annealed at 300°C

From Fig 3.38 we can see that these sensors show a higher response with lower sensor operating temperature at RT and 100 °C Response rises with temperature, peaks around 150°C and then falls as temperature increases further. Also, with lower thickness response amplifies, as seen with homogenous SnO_2 sensor.

From Fig 3.37 we can see that at 900°C anneal temperature all sensors have baseline resistances in $G\Omega$ range. The resistances are also higher at lower thickness. We can see that sensors also produced higher responses at lower operating temperatures meeting our objective. For this composition of Sn-Zn-O it was also found that sensors could be on-chip annealed at

lower temperatures instead of going until 900°C.

3.6 E-Nose Performance Testing

Testing sensors array with wider catalog of gases and with gas mixtures would both validate and help calibrate it for real-time use in environment and breath monitoring where multiple gases are present. Therefore here binary gas mixture of acetone and ethanol are introduced as a starting point, with six sensor elements to asses its E-Nose performance. Few interfering gases in breath and environment like the toluene and formaldehyde are also tested. Finally, qualitative tests with human breath under the influence of alcohol, post meals and fasting are done.

Gas testing setup (Dr. Omer Oralkan's lab) used for these experiments is shown in Fig 3.39, which could produce a mixture of gases. The flow rates and mixtures concentrations could be all electronically controlled with a Graphic user interface as shown in Fig 3.40.

Figure 3.39: Gas generation setup for simultaneous multiple gas generation

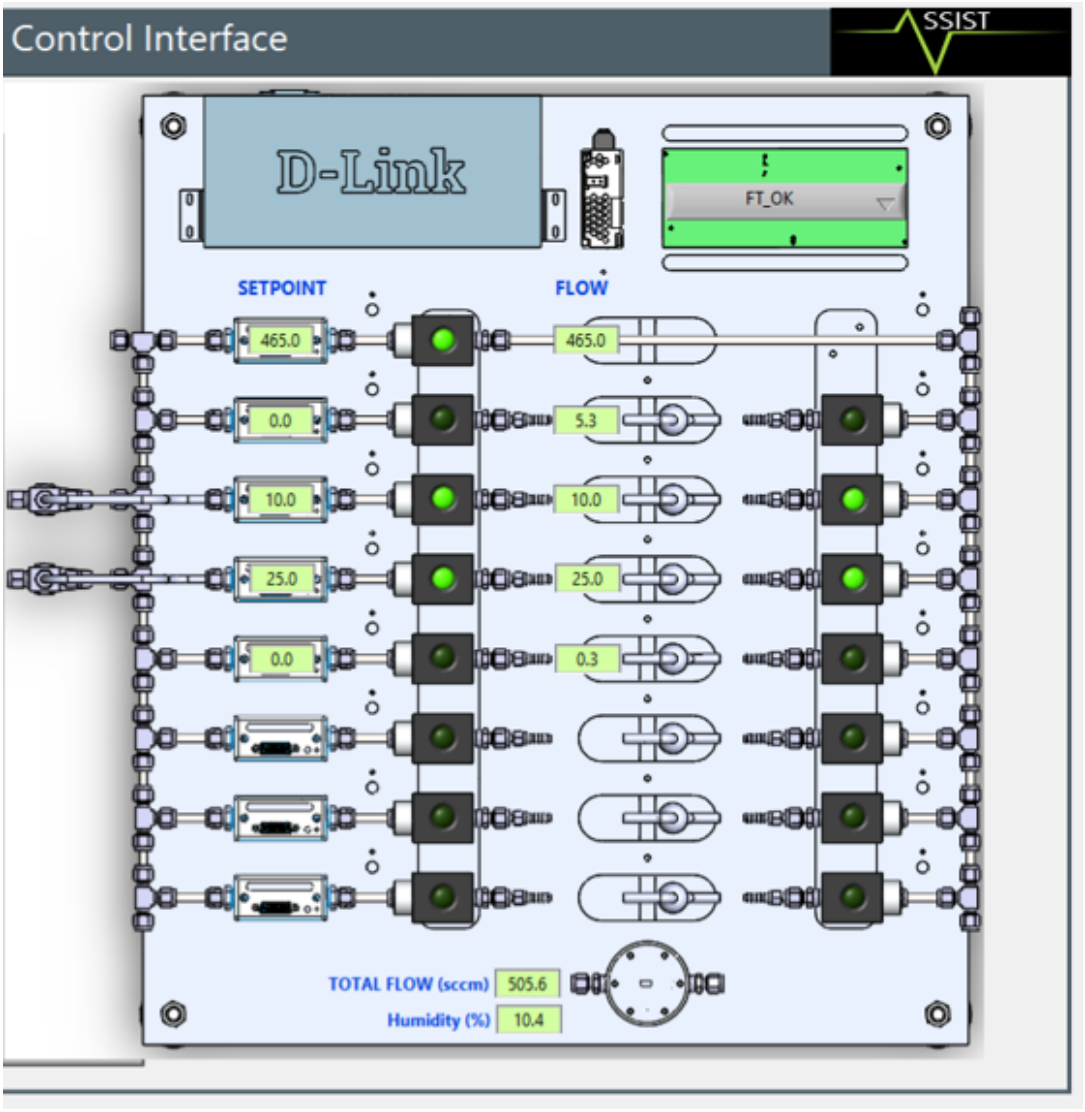

Figure 3.40: Control interface for Fig 3.39

3.6.1 Gas Mixtures - Acetone and Ethanol

Six sensors representative of all our building blocks of sensor array have been selected for this testing. n-type Sno_2 of two different thicknesses 30 cycles and 50 cycles of ALD, p-type sensor of 600 cycles and 1200 cycles of ALD and Sn-Zn-O composites deposited with 30 cycles of

SnO_2, 30 cycles of ZnO followed by annealing at 300C in Nitrogen for one minute along with an as-deposited sensor were used. The SnO_2, CuO homogeneous sensors were annealed at 600C for 2 hours in air.

Typical responses of acetone at 150 °C with acetone and ethanol. Acetone concentrations of 5, 10, 50, 100, 150 ppm, Ethanol Concentrations of 0.5, 1, 5, 10, 20, 40 ppm were used. The total flow rate was at 500 sccm.

For mixtures, below corresponding concentrations were mixed.

Table 3.8: Concentrations of gas mixtures used for testing

Segment #	Acetone conc. (ppm)	Ethanol conc. (ppm)
1	5	1
2	10	5
3	50	10
4	100	20
5	150	40

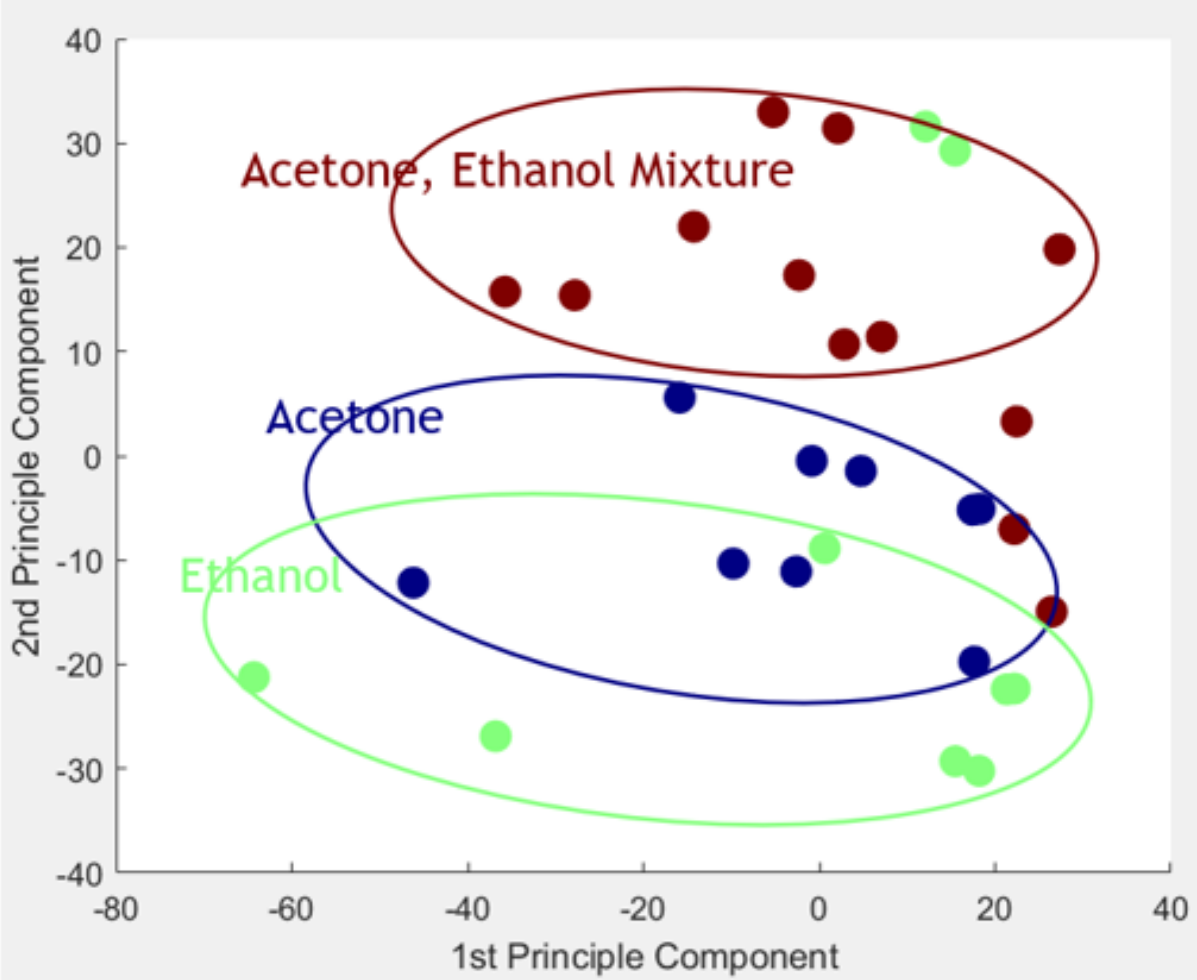

Figure 3.41: PCA response of acetone-ethanol gas mixture

Fig 3.41 shows the PCA for acetone, ethanol and its mixture. A separation of over 75% of the mixture with the constituent gases could be seen. Further separation could be gained by both optimizing sensor elements in the ways discussed before and with alternate machine learning algorithms.

3.6.2 Interference Tests - Toluene, Formaldehyde and Carbon monoxide

:

Interference of these six sensor elements was also tested with interfering gases like Toluene, Formaldehyde and carbon monoxide. The tests were done upto 250°C to check for any response.

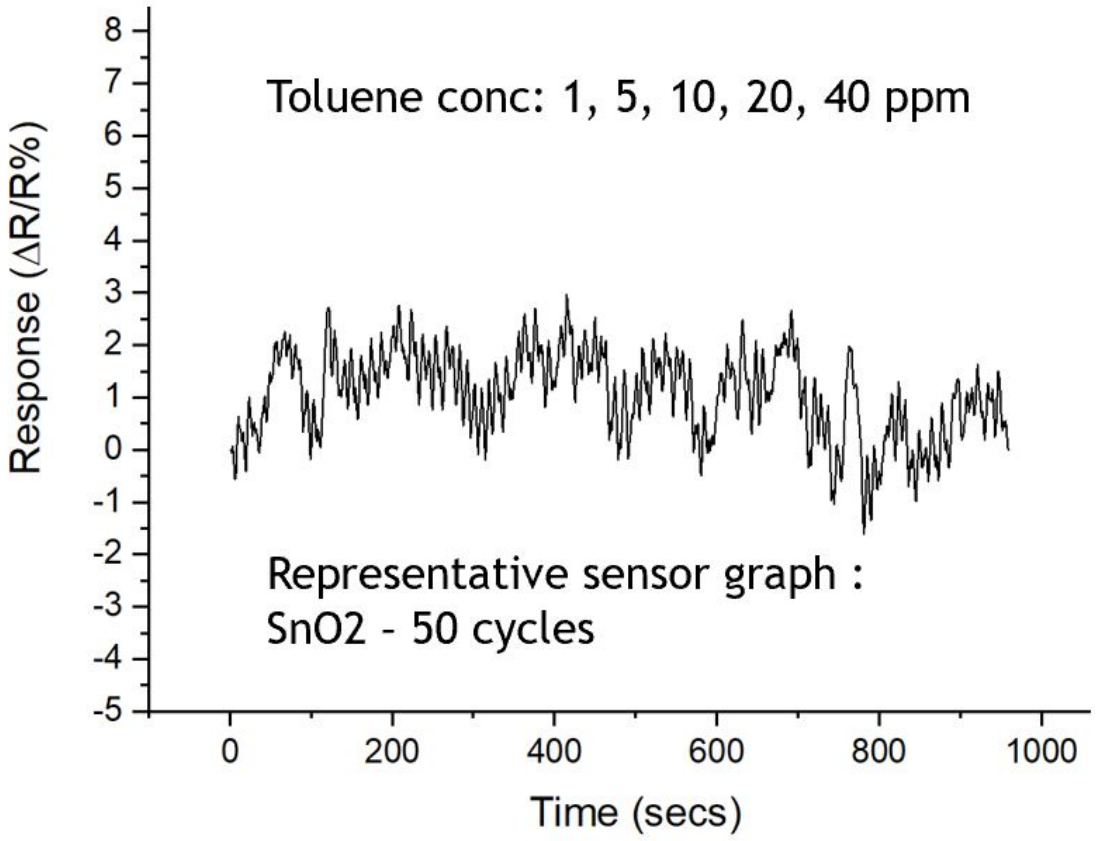

Figure 3.42: Representative response of sensor SnO_2 (50 cycles - 6 nm) with various concentrations of toluene

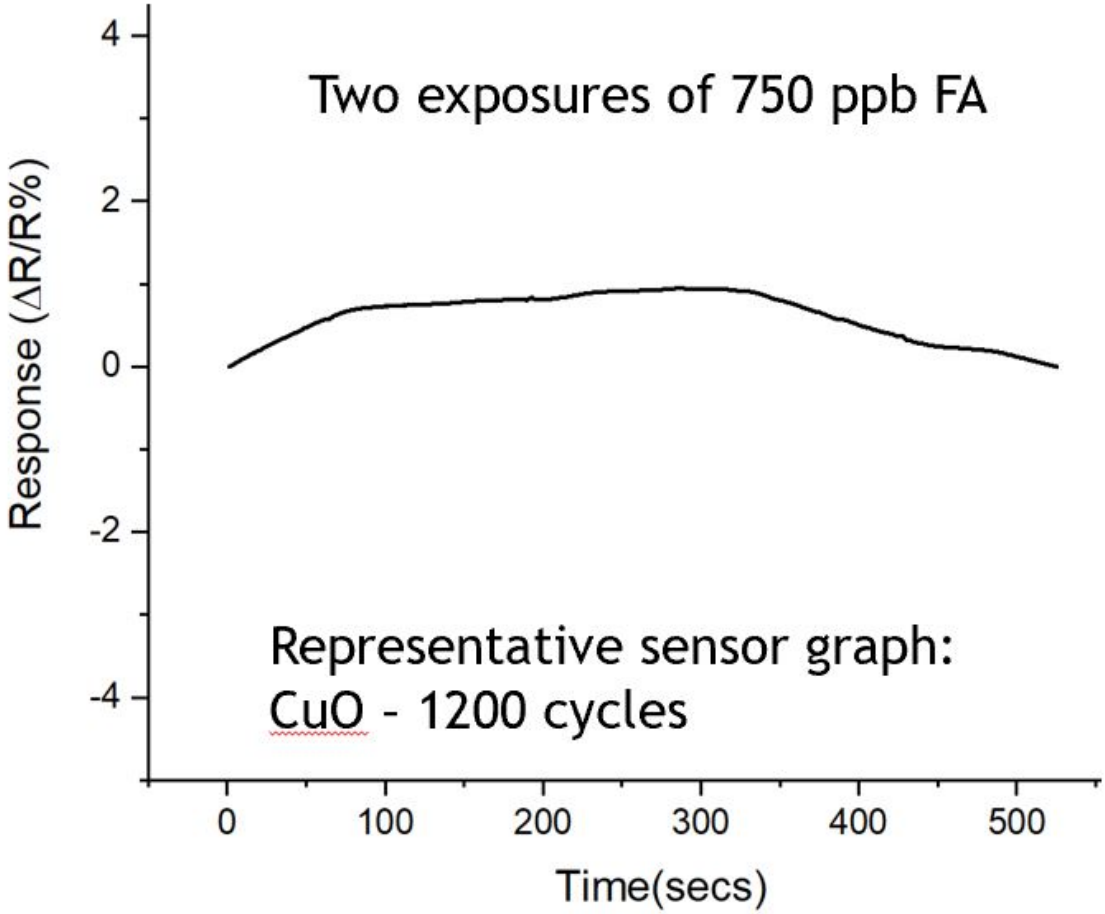

Figure 3.43: Representative response of CuO sensor (1200 cyles - 40 nm) with various concentrations of formaldehyde

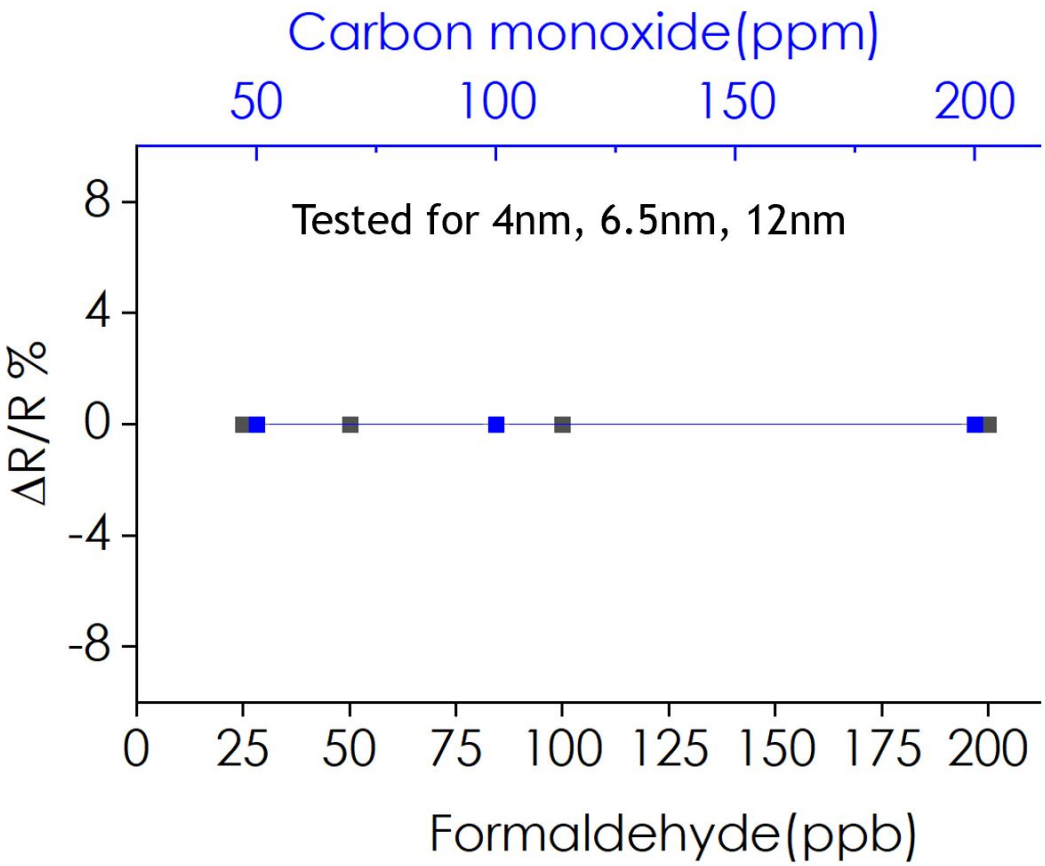

Figure 3.44: Representative response of SnO_2 sensor (4 nm, 6.5 nm and 12 nm) with various concentrations of carbon monoxide

We could see from Fig 3.42 and Fig 3.44, that there is little to no response with these gases across the tested range.

3.6.3 Breath Analysis - Acetone and Ethanol

To check yet another practical application with real life use cases, these gas sensors were qualitatively tested with gases with breath collected from the subject without fasting, after

fasting for 30 hours and post alcohol consumption. The sensors that were used for this test were homogenous 50 cycles SnO_2 (6 nm), annealed at 600°C and a composite SnO_2/ZnO 50/50 cycles (6 nm/8 nm) sensor.

Figure 3.45: Design mask showing different heater designs currently being fabricated

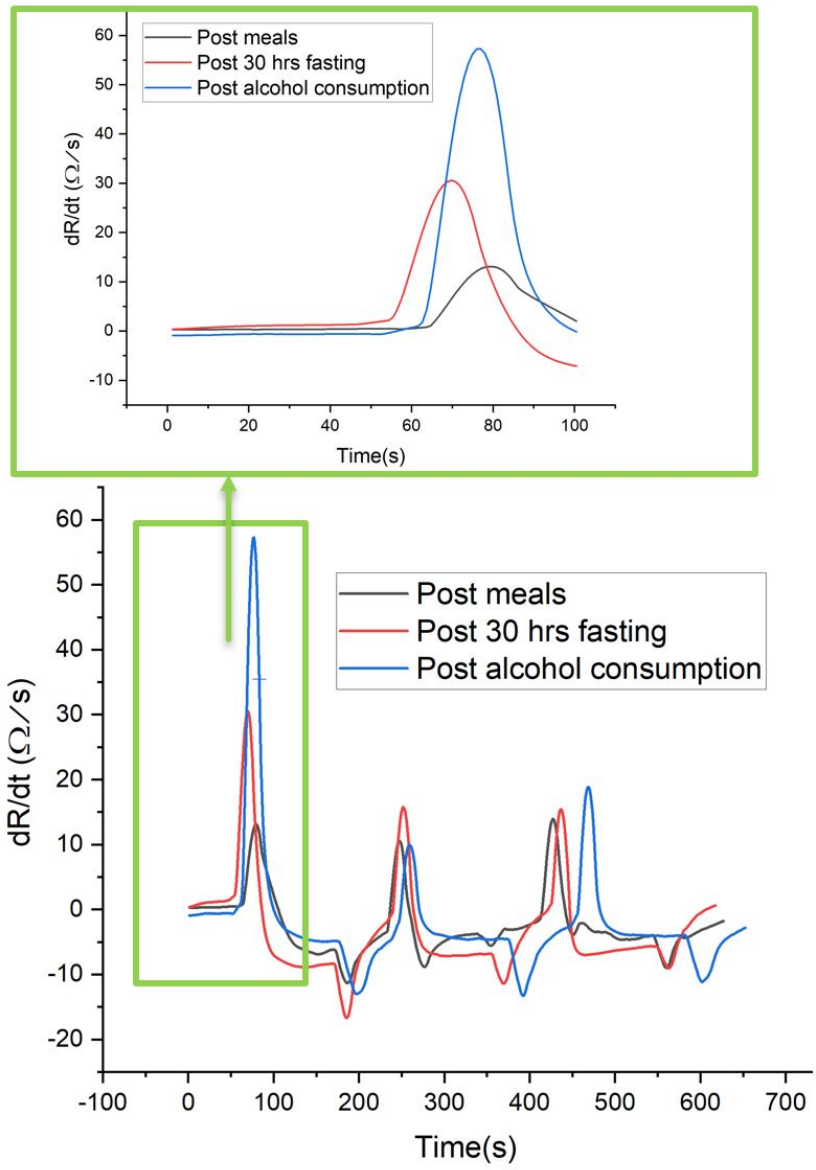

Figure 3.46: Design mask showing different heater designs currently being fabricated

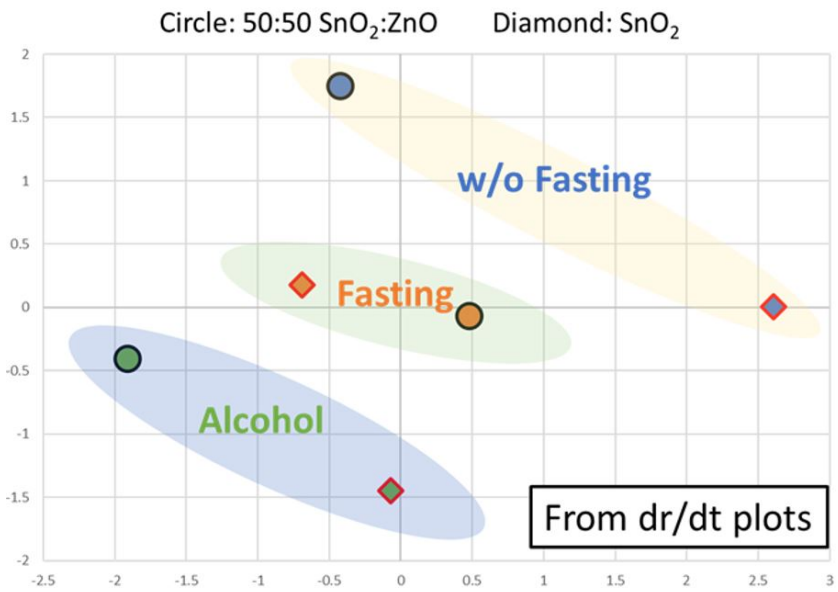

Figure 3.47: Design mask showing different heater designs currently being fabricated

The results as seen in Fig 3.45, Fig 3.46 and Fig 3.46 show the separation as between the three different conditions. This shows the practical applicability of a fully built monolithic E-Nose deployed in real-life situations.

3.7 Summary

The key features of our proposed novel approach towards building a monolithic array of multiple metal oxide sensors for E-Nose applications via selective on-chip annealing were demonstrated. Multiple sensor surfaces were obtained through annealing of multilayered ALD stacks to simulate on-chip selective annealing. The simplistic approach of fabrication can reduce the number of fabrication steps and production costs for faster adoption of the sensor technology into wearable space. The various components of the monolithic sensor array were developed and

tested in parallel. The FEM simulations for the micro-heater design Table.3.7 show that for one of the microheaters designs (Fig.3.28 (a)) power numbers as low as 6.3 mW for an operational temperature of 400°Cand a power of 1.58 mW for an operating temperature of 100°Ccould be reached. The average-power for 10% duty cycling at 400°Ccould therefore reach as low as 630 μW. The sensors were optimized after the initial run by varying thickness and composition of Sn-Zn-O film to achieve high responsiveness at lower operation temperatures. Response with ozone in the 100°C-150°Cwere seen. Characterization of sensors was done with gas mixtures of acetone and ethanol, with a separation of over 75% of the mixture with the constituent gases could be seen. While the sensors in the current make-up have seen to not respond to toluene, formaldehyde or carbon monoxide. Finally to test a real-time use case scenario of alcohol and acetone, sensors were tested with exhaled human breath post-fasting and alcohol consumption, showing distinguishable response with normal reference breath.

CHAPTER

FOUR

SYSTEM INTEGRATION AND FIELD TESTING

In this chapter, the integration of SnO_2 sensors at systems level is discussed. Our in-house fabricated SnO_2 sensors have been wire-bonded with wearable devices made by Dr. Alper Bozkurt group at NCSU and with low power data-acquisition systems made by Dr. Ben Calhoun's group at UVa.

4.1 Integration: HET

Parts of below sections originally appeared in Misra, Veena, et al. "Ultra-low power sensing platform for personal health and personal environmental monitoring." 2015 IEEE International Electron Devices Meeting (IEDM). IEEE, 2015. and in Mills, Steven Christopher. "Ultra-

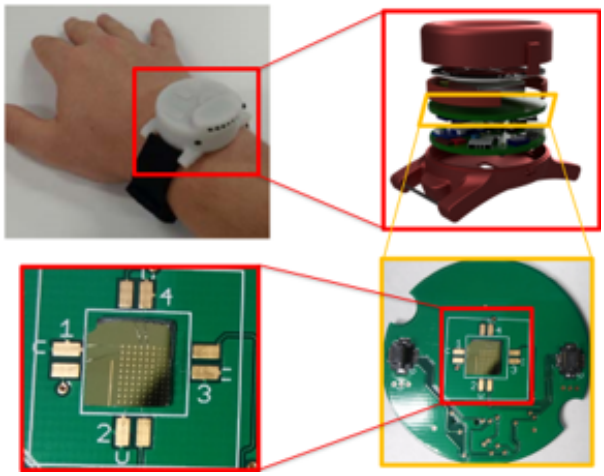

Figure 4.1: First Generation HET

low power room temperature metal oxide gas sensors: A study in sensitivity, selectivity and reliability." (2017).

The Health and Environmental Tracker (HET) testbed is the system designed to drive and support the development of sensor technologies produced by the ASSIST Center. The HET was designed and built primarily by Dr. Alper Bozkurt group at NCSU. This system incorporates an ultraviolet (UV) LED emitting a wavelength of 385 nm for sensor recovery. As described in previous chapters, the UV light excites the electrons trapped during ionosorption of ozone, which allows the oxidizing gas molecule to desorb and recover the sensor resistance to the starting reset resistance value. The UV LED is mounted face up on the main circuit motherboard while the sensor was mounted to the small, removable daughter board that faces downward. The sensor chip was secured directly to the daughter board using double sided tape and wire bonds were made from contact pads on the sensor to the contact pads on the circuit board.

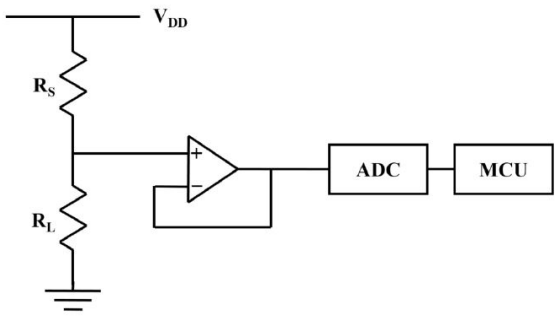

Figure 4.2: Voltage divider circuit designed to read out SnO_2 sensor data

4.1.1 Simulated Field Testing

Simulated field testing was done in EPA labs with our SnO_2 12 nm sensor wirebonded on the Health and Environmental Tracker(HET) (Fig.4.1). The flow through testing chamber used for the in-lab experiments in previous chapters was small and directed a gas stream directly onto the sensor. To more accurately simulate field testing conditions, a diffusion gas testing was done at the Environmental Protection Agency (EPA) which is a large ozone chamber which allows gas to come into contact with the sensor through a diffusion process rather than a directed flow. The chamber is show in Fig.4.3 and described briefly below:

EPA testing chamber LA75 has a floor area of 29.7 m2 with 3.2 m high ceilings. The chamber operates under a slight negative air pressure and incorporates temperature, humidity, and pollutant control systems. Ozone is generated by the silent arc discharge method using USP (United States Pharmacopeia) grade oxygen. The environmental conditions inside the chamber are recorded as two minute averages and stored in a database. The HET and the integrated gas sensor are placed on a table in the chamber for the duration of the experiment, which was typically 7-8 hours, and the data was transmitted in real time to a laptop outside of the chamber. The HET platform used in these experiments is programmed to record resistance and continuously

Figure 4.3: EPA Labs at UNC Chapel Hill

cycle through a response measurement and recovery cycle. The sensor measurement circuit is a voltage divider shown in Fig.4.2 where RS is the gas sensor resistance, RL is a load resistance, VDD is five volts, ADC is an analog to digital converter and MCU is a microcontroller that receives and transmits the digital data. The operational amplifier between the voltage divider and the ADC is configured for unity gain as a voltage buffer. During response measurement, the UV LED is off and the voltage across the load resistor is measured. From this measurement and the known value of RL, the sensing film resistance is calculated. After recording the increasing resistance values for a specified time (2 or 3 minutes), the recovery period begins and the UV LED turns on. During recovery, gas species desorb due to the energy of the UV light and the resistance drops. The tests were typically done for close to 10 hours and the results are shown in Fig.4.4. The first derivative curve as discussed in Chapter 2, is usually proportional to the concentration of the ozone gas. We can see in in Fig.4.4 that the derivative curve follows the trend of ambient ozone concentration in the EPA room.

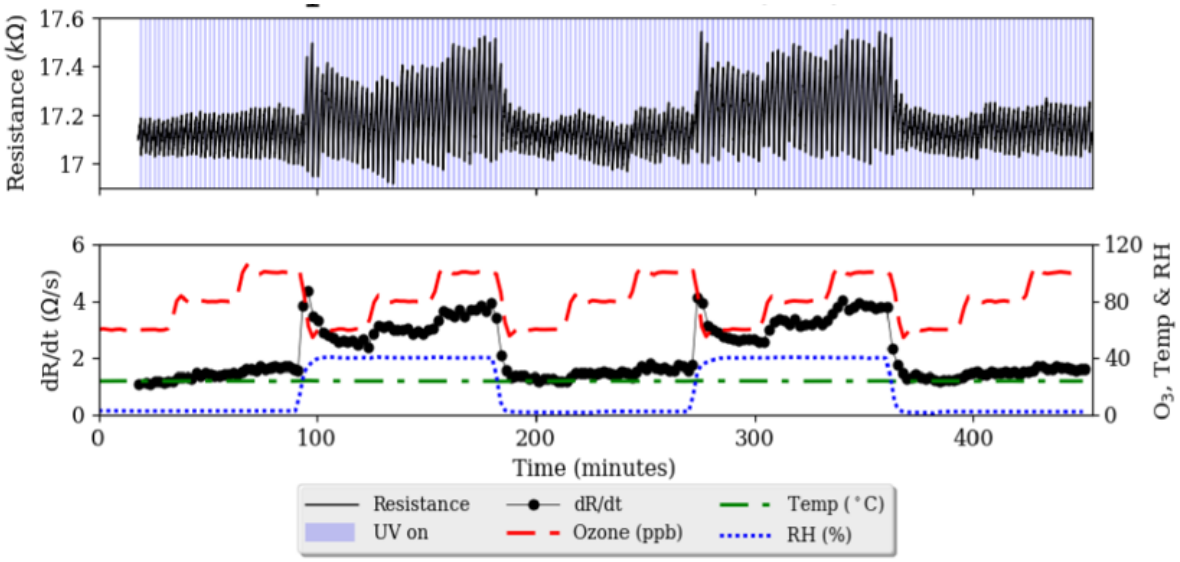

Figure 4.4: Ozone field testing at EPA labs

This real-time diffusion based test study validated the directed gas flow experiments done in the lab. In the humidity experiments we could see that the amplification of response in the presence of humidity also lead marked increase in resolution between the same concentrations of ozone as observed in lab.

4.2 An 88.6nW Ozone Pollutant Sensing Interface IC with a 159 dB Dynamic Range

This section originally appeared in Agarwala, Rishika, et al. "An 88.6 nW ozone pollutant sensing interface IC with a 159 dB dynamic range." Proceedings of the ACM/IEEE International Symposium on Low Power Electronics and Design. 2020.

This part of the work presents a low power resistive sensor interface IC designed at 0.6V for ozone pollutant sensing. The large resistance range of gas sensors poses challenges in designing a low power sensor interface. Exiting architectures are insufficient for achieving a high dynamic range while enabling low V_{DD} operation, resulting in high power consumption regardless of the adopted architecture. We present an adaptive architecture that provides baseline resistance cancellation and dynamic current control to enable low V_{DD} operation while maintaining a dynamic range of 159dB across 20kΩ-1MΩ. The sensor interface IC is fabricated in a 65nm bulk CMOS process and consumes 88.6nW of power which is 300x lower than the state-of-art. The full system power ranges between 116 nW - 1.09 μW which includes the proposed sensor interface IC, analog to digital converter and peripheral circuits. The sensor interface's performance was verified using custom resistive metal-oxide sensors for ozone concentrations from 50 ppb to 900 ppb.

4.2.1 Introduction

With increasing air pollution, prolonged exposure to air pollutants is known to have physiological effects. Ozone (O_3) in particular, when present in high concentrations, induces respiratory effects such as shortness of breath, wheezing, and exacerbation of asthma [37]. Since the ozone advisories issued by the government are based on predictions, the actual ozone concentration might differ from the forecasted value. This necessitates a portable ozone monitoring device to track personal exposure and indicate potentially unsafe surroundings. To realize a reliable system that could be either be powered by body-worn energy harvesters or require infrequent battery charging, the designed system must be compact and should consume low power.

$$R_{sen} = R_{base} + \Delta R_{gas} \tag{4.1}$$

R_{sen} ranges from several kΩto tens of MΩwhen exposed to the targeted gas, which in our case is O_3. Due to this a readout with high dynamic range is required. A generic sensor interface for resistive gas sensors consists of a current source (I_{bias}) to convert R_{sen} into voltage (V_{sen}) (2), followed by the readout.

$$V_{sen} = I_{bias} \times R_{sen} \tag{4.2}$$

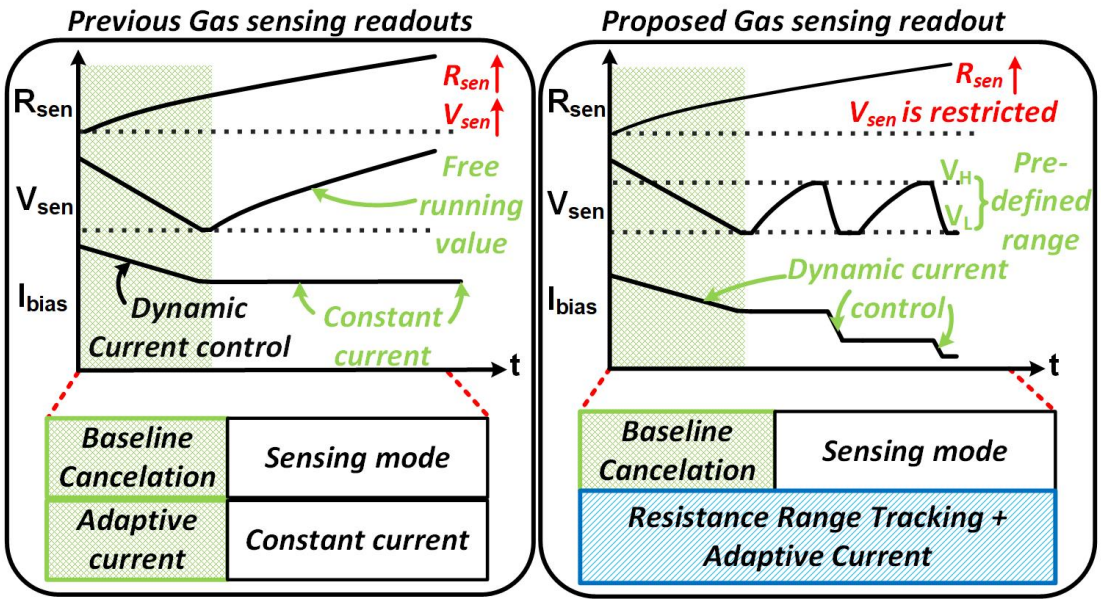

Figure 4.5: R-V conversion of the proposed sensor interface IC, compared to previous gas sensing interfaces [4],[5].

Past works have implemented gas sensing readouts using N-bit current-steering DACs (IDACs) [38]. However, their resolution is limited since they directly digitize R_{sen}. They also require a high-resolution ADC to achieve the required dynamic range which increases the power consumption. Interfaces using operational amplifiers (op-amps) before digitization have been proposed to boost the dynamic range[39]. However, due to the large range of R_{sen}, the op-amp must have a wide input common mode range, which requires high power consumption. The

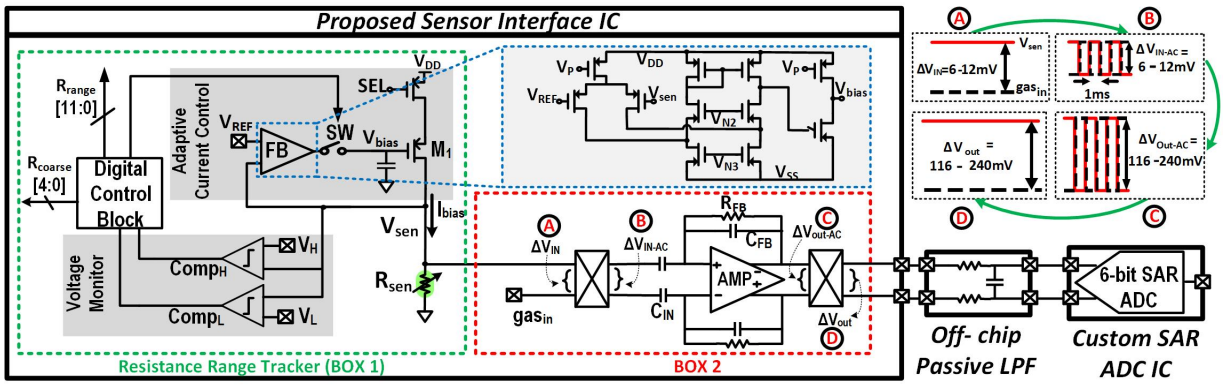

Figure 4.6: Proposed ozone sensing sensor interface IC along with the test setup.

need for large input common mode range also constrains V_{DD} scaling, which otherwise is an effective solution to reduce power. A baseline cancellation approach has been proposed to improve the dynamic range by isolating ΔR_{gas} from R_{sen} in baseline cancellation mode, and continue sampling ΔR_{gas} in sensing mode [40][37]. However, since during sensing mode, these authors use a constant I_{bias} to convert R_{sen} to V_{sen}, a wider input common mode range is required to ensure that V_{sen} lies within the operating range of the op-amp. This again makes low V_{DD} operation challenging. Additionally, keeping a constant I_{bias} across the entire resistance range decreases the energy efficiency as I_{bias} is a major contributor to power.

This paper adopts an opamp-based sensor interface which proposes a Resistance Range Tracker (RRT) to dynamically vary the current (I_{bias}) during both baseline cancellation and sensing mode, to balance the need for both low power operation and high dynamic range. In contrast to other works, the proposed method continues to limit V_{sen} to a predetermined voltage range by sourcing a dynamically varying current (I_{bias}) to the sensor during the sensing mode (Fig.4.5). This approach prevents the input at the op-amp from exceeding its input common mode range, thus enabling the design to work at a lower V_{DD} (0.6V). Additionally, the power consumed by I_{bias} generation is reduced by dynamically varying the current (I_{bias}). This approach also

relaxes the need for aggressive baseline cancellation and a high-resolution ADC. A more detailed explanation is provided in section II. Fabricated in 65 nm CMOS, this sensor interface achieves a 159dB dynamic range across 20kΩ-1MΩwhile consuming 88.6nW power. The sensor interface is also verified with two atomic layer deposited (ALD) SnO_2 metal oxide sensors previously fabricated at North Carolina State University [38].

4.2.2 System Architecture

The MOX sensor has a positive resistance change rate (ΔR_{sen}) with increasing O_3 concentration. The sensor R_{sen} at any given time can be represented by (3), where R_{base} is the sensor's initial baseline resistance, and $R_{gas}^{t_i}$ is the instantaneous resistance due to the ambient O_3 concentration. R_{base} is canceled during the initial baseline cancellation mode, which is followed by the sensing mode in which the readout proceeds to track the increase in resistance (ΔR_{sen}) over a fixed period of time (4). The proposed sensor interface divides the large resistance range of the sensor into multiple subranges, each spanning across an equal voltage step.

$$R_{sen}^{t_i} = R_{base} + R_{gas}^{t_i} \tag{4.3}$$

$$\Delta R_{sen} = R_{gas}^{t_2} - R_{gas}^{t_1} \equiv \Delta R_{gas} \tag{4.4}$$

$$R_{gas}^{t_i} = \frac{\Delta V_{out}}{A_v I_{bias}} \tag{4.5}$$

Fig.4.6 depicts the system architecture of the proposed sensor interface. The RRT (Box 1) is implemented by an adaptive current controller (ACC) assisted by a voltage monitor to regulate V_{sen} such that the input-voltage swing (ΔV_{IN} = V_{sen}- gas_{in}) at the amplifier's differential input is within the predefined range (6mV-12mV). It also gives a 5-bit digital output, R_{coarse},

that tracks the subrange in which R_{sen} can be mapped. Box 2 highlights a chopper-stabilised differential amplifier (AMP) with one of its inputs connected to the O_3 sensor, while the other is connected to an AC ground ($gas_{in} \equiv 30mV$). Choppers convert the near-DC signal (ΔV_{IN}) at the amplifier's input to a differential AC signal (ΔV_{IN-AC}). This signal is then amplified by the chopper-stabilised differential amplifier (AMP). After signal amplification, the amplifier's high frequency output (ΔV_{Out-AC}) is then chopped back to a near-DC baseband signal (ΔV_{OUT}). R^{ti}_{gas} can be computed using the amplifier's differential output voltage (ΔV_{OUT}), its voltage gain (A_V) and the I_{bias} current corresponding to R_{coarse} [41].

4.2.3 Resistance Range Tracking

The RRT comprises a PMOS transistor (M1) acting as a current source regulated by an ACC, a voltage monitor that tracks the voltage across the sensor (V_{sen}), and a digital control block. I_{bias} from the current source is used to convert R_{sen} into V_{sen} due to the IR drop. ACC is implemented by M1 acting as a voltage-controlled current source, which is regulated by using a negative feedback amplifier (FB) along with a switch (SW) connected to its gate. When SW is closed, the M1 current (I_{bias}) is controlled by driving its gate with an error signal (V_{bias}) between V_{sen} and a fixed input reference (V_{ref}). In this way V_{sen} is gradually driven to a predetermined value V_{ref} (36mV), keeping $\Delta\, V_{IN}$ within the predefined range (6mV-12mV). The voltage monitor uses a window comparator to detect if V_{sen} is within the limits of V_H(43 mV) or V_L(37 mV). The comparator outputs ($Comp_H$ and $Comp_L$) are fed into a digital control block that uses a 12-bit counter to track the change in the resistance subrange and also control SW, which connects ACC to M1.

Fig.4.7 shows the flow chart and timing diagram of the RRT. The RRT works in two operating

modes: 1) baseline cancellation mode and 2) sensing mode. The sensor interface starts with the RRT in baseline cancellation mode. In this mode, M1 is initially power gated by setting SEL to V_{DD}. SW is then closed, enabling the ACC to control I_{bias} to regulate V_{sen} to V_{ref} (36 mV). The voltage monitor tracks if V_{sen}> V_H while incrementing a 12-bit counter (R_{range}) to denote the time taken by ACC. This value maps R_{base} to its resistance subrange. Now, RRT enters the sensing mode by opening SW and holding I_{bias} constant. As the ambient O_3 changes, R_{sen} starts increasing which in turn increases V_{sen}. Once V_{sen} exceeds the limits of V_H and V_L, SW is toggled and the R_{coarse} counter value is increased to update the R_{sen} mapping. As SW is closed, I_{bias} is adjusted such that V_{sen} returns to V_{ref} (36 mV). This ensures that the input to the AMP is within the predefined range (6mV–12mV). After voltage monitor indicates that V_{sen} is below V_L, SW is opened again.

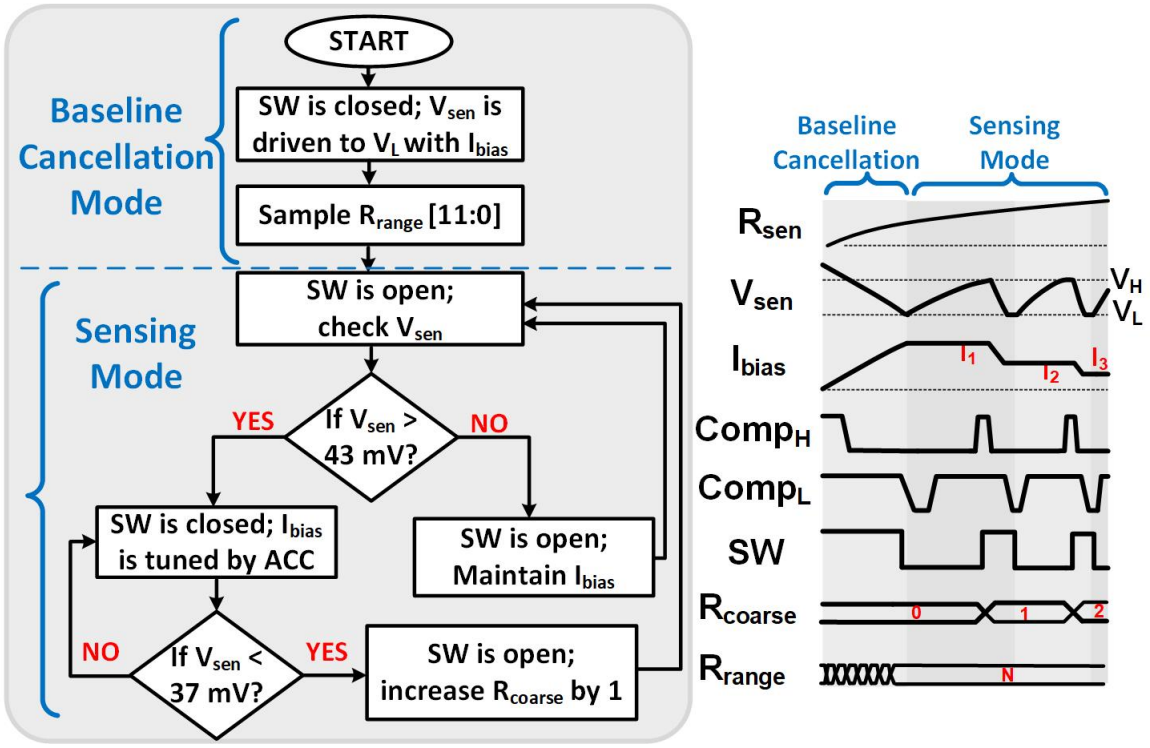

Figure 4.7: Flowchart of the RRT and associated timing diagram.

Resistance To Concentration Conversion

Fig.4.8 shows the flow chart of the resistance-to-O_3 concentration conversion. The proposed sensor interface starts with the RRT in baseline cancellation mode. Once V_{sen} is driven to 36mV, R_{range} is sampled, giving R_{base}. The sensor interface now enters the sensing mode in which the AMP's output (ΔV_{OUT}), M1's current (I_{bias}), and R_{coarse} are sampled and later used to compute R^{ti}_{gas}. Each sensing iteration lasts for 2 minutes, where R^{t1}_{gas} and R^{t2}_{gas} are obtained at the beginning and end of the iteration. At the end of 2 minutes, the difference between R^{t2}_{gas} and R^{t1}_{gas} is used to calculate the O_3 concentration during post-processing as given in (Eq.4.6). The sensor is characterized to obtain the value of α. For any subsequent sensing cycles, RRT remains in the sensing mode.

$$+\alpha C \propto \frac{\Delta R_{gas}}{\Delta time} \tag{4.6}$$

Circuit Implementation

Fig.4.9 shows the schematic of the chopper-stabilized differential amplifier used in the sensor interface. Owing to the small signal level, a fully differential amplifier is chosen to minimize the common mode noise. As the O_3 sensor's signal is a near-DC signal, flicker noise (1/f noise) becomes a major concern which degrades the signal-to-noise ratio and also reduces the sensor interface's input dynamic range. So chopping is used to remove the flicker noise from the baseband, leaving only thermal noise. The chopping frequency is set to 1kHz since it is high enough to sufficiently reduce the differential amplifier's input noise density and at the same time requires a relatively low bias current to achieve the resulting amplifier bandwidth.

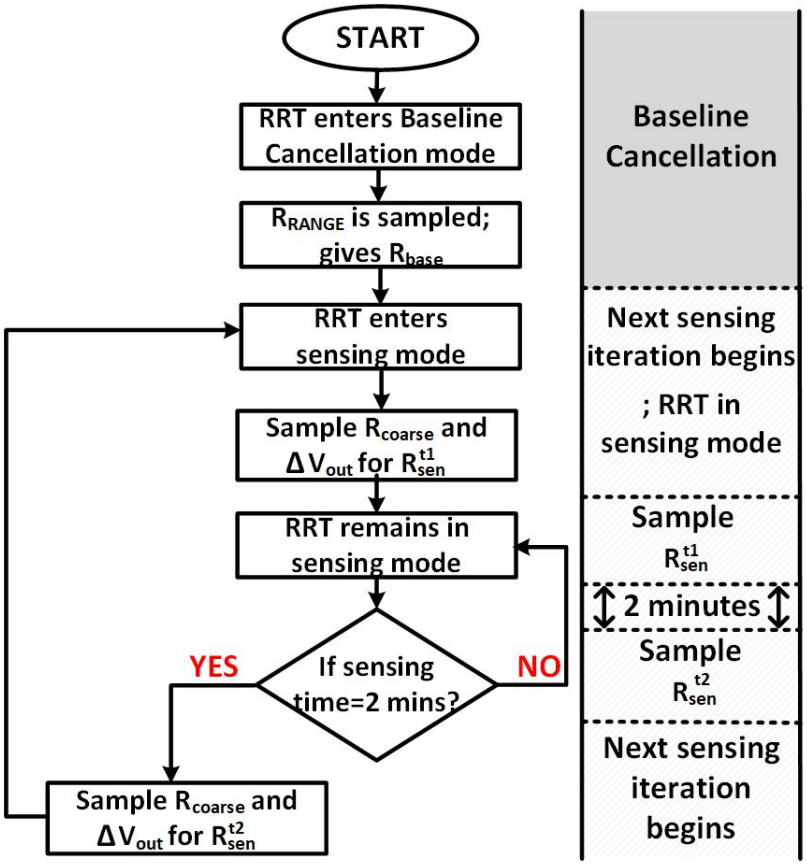

Figure 4.8: Flowchart of the conversion from resistance to ozone concentration.

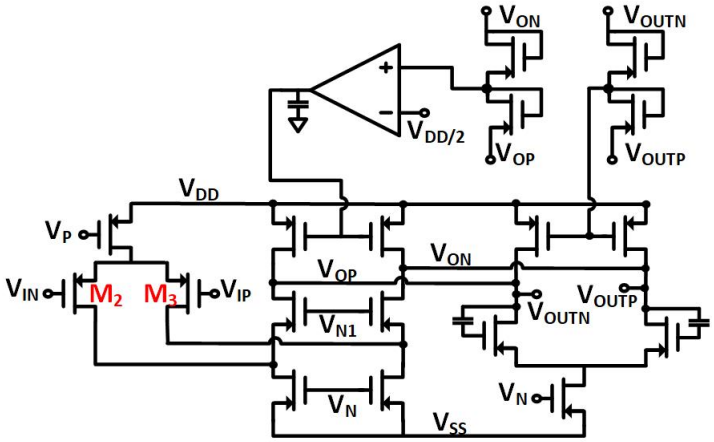

Figure 4.9: Transistor level schematic of the chopper-stabilized differential amplifier.

Additionally, PMOS transistors (M2, M3) are used as input devices and sized to further decrease the thermal noise. Pseudo-resistive feedback is used to provide DC biasing for the input pair, and the amplifier's voltage gain is set to 25.72dB. The current source M1 in ACC is sized such that it can source a sufficiently large I_{bias} to regulate V_{sen} to 36 mV over the entire range of R_{sen}. The required value of I_{bias} is maximum at the baseline resistance and decreases in subsequent subranges. To reduce the IDAC power consumption which otherwise is a major contributor, the value of gas_{in} is fixed at 30mV while V_{sen} is chosen to lie between 36mV-43mV. While this limits the input voltage swing (ΔV_{IN}) to 6mV-12mV, it also reduces the I_{bias} required to regulate V_{sen} to the desired value. The off-chip passive low-pass filter is used to reduce the chopping spikes at the ADC input.

4.2.4 Measurement Results

The proposed sensor interface IC was fabricated in a 65 nm CMOS process with an active area of 1.28 mm^2. Fig. 4.10 shows an annotated die micrograph of the fabricated chip. Fig. 4.11 shows the measured differential output voltage (ΔV_{OUT})(left) from the chopper-stabilized amplifier (AMP) and the associated current (I_{bias})(right) sourced from M1 across a resistance range of 20 kΩto 1 MΩ. It also represents the subrange division mapping over the entire resistance range. Fig. 4.12 shows the sensor interface's measured input-referred noise of 460 nV_{rms} across the frequency range of 0.1Hz to 1Hz. Finally, figs. 4.13(a) and 4.13(b) demonstrate the measurement results for evaluating the functionality of the sensor interface IC for O_3 sensors with thicknesses of 6.5 nm and 12 nm, respectively [38]. To facilitate this, a "Teledyne T700U" gas calibration system with a capability to generate O_3 with precise concentrations down to under 10 ppb was used. The gas was directed into a custom-built testing chamber where the sensor was placed for testing. The measurements were carried out at different O_3 concentrations. Each measurement

was followed by the sensor surface being exposed to a UV LED in order to prevent the sensor from saturating and also provide similar testing conditions at each concentration. The sensor interface's output is post-processed using equations (4.3)-(4.6) to successfully measure and map the resistance change (ΔR_{gas}) to O_3 concentrations. The sensor interface IC can reliably measure O_3 concentrations from 50 ppb to 900 ppb with a measured error of 0.01% while maintaining a measured dynamic range of 159 dB. Fig. 4.14 demonstrates the measured sensitivity and the sensor interface linearity, with R^2 values listed in the figure. The on-board passive low-pass filter is used to remove the chopping spikes in the readout's analog output before passing it to the ADC. The proposed sensor interface operates at 0.6V with a power consumption of 88.6 nW which is 300x lower than the state-of-art. The proposed readout was also verified together with a custom 6-bit SAR ADC chip fabricated in 65 nm CMOS. The power consumed by the custom ADC chip is 9 nW while that by the IDAC (M1) to drive the MOX sensor is measured to be within 19.2 nW to 997 nW, making the system-level power consumption to range in 116 nW - 1.09 μW which is at least 29X less than prior works.

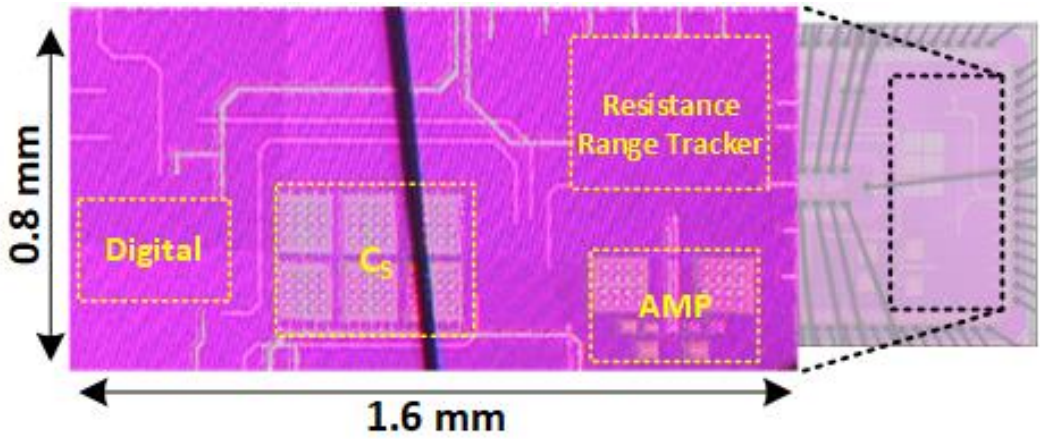

Figure 4.10: Annotated die photo of the proposed sensor interface IC.

Table.4.1 summarizes the performance of the proposed sensor interface, and figs. 4.15(a)

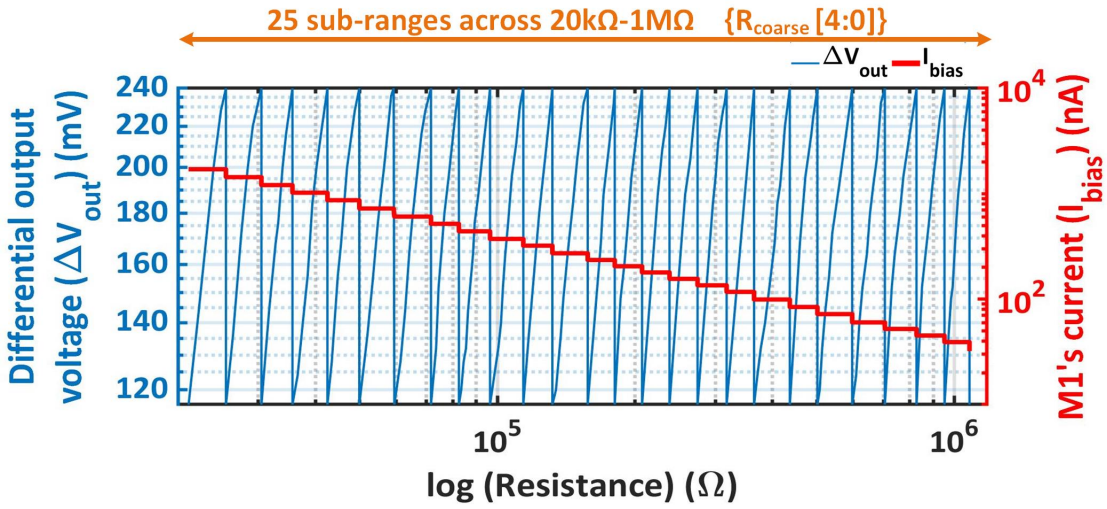

Figure 4.11: Measured analog output voltage (left) and IDAC current (right) of the sensor interface as a function of resistance (R_{sen}).

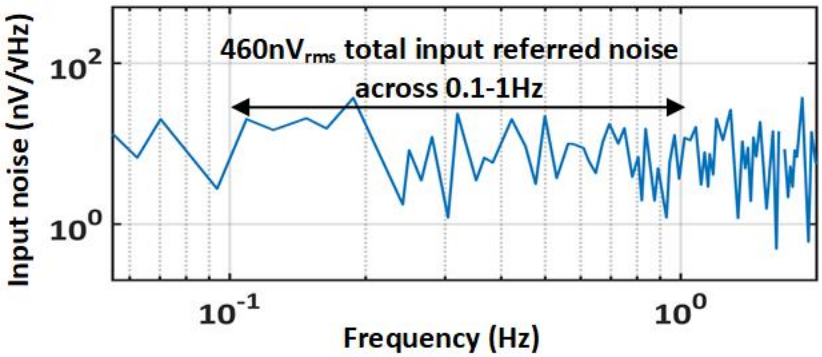

Figure 4.12: Measured input-referred noise density of the sensor interface.

Table 4.1: Performance Summary and State-of-Art Comparison

	This Work	[2] JSSC'09	[3] JSSC'07	[5] ISCAS'11	[7] TbioCAS'11	[8] JSSC'16	[9] CASME'11	[10] JSSC'07
Process	65 nm	180 nm	350 nm	500 nm	180 nm	350 nm	180 nm	350 nm
Supply Voltage	0.6 V	1.2 V	3.3 V	3.3 V	1.8 V	3 V	1.8 V	3.3 V
Area (mm²)	1.28	0.72	3.1	4.84	3.89	12	2.5	0.42
Readout Power	88.6 nW	32µW	2.3 mW	66µW	42.3µW-96.6µW	889µW	1.04mW	N/A
IDAC Power	19.2nW - 997nW	N/A	2.8 mW	N/A	N/A	N/A	93.6µW	3.3nW-3.3mW
Total power	116nW -1.09µW	32µW	6 mW	66µW	46µW-100µW	890.8µW	1.13 mW	15 mW
Resistance Range	20kΩ – 1MΩ	10kΩ–9MΩ	100Ω–20MΩ	60kΩ–10MΩ	1kΩ–1.5MΩ	1Ω–10MΩ	10kΩ–10MΩ	1kΩ–5MΩ
Dynamic Range	159 dB	N/A	160 dB	120 dB	N/A	N/A	N/A	128 dB

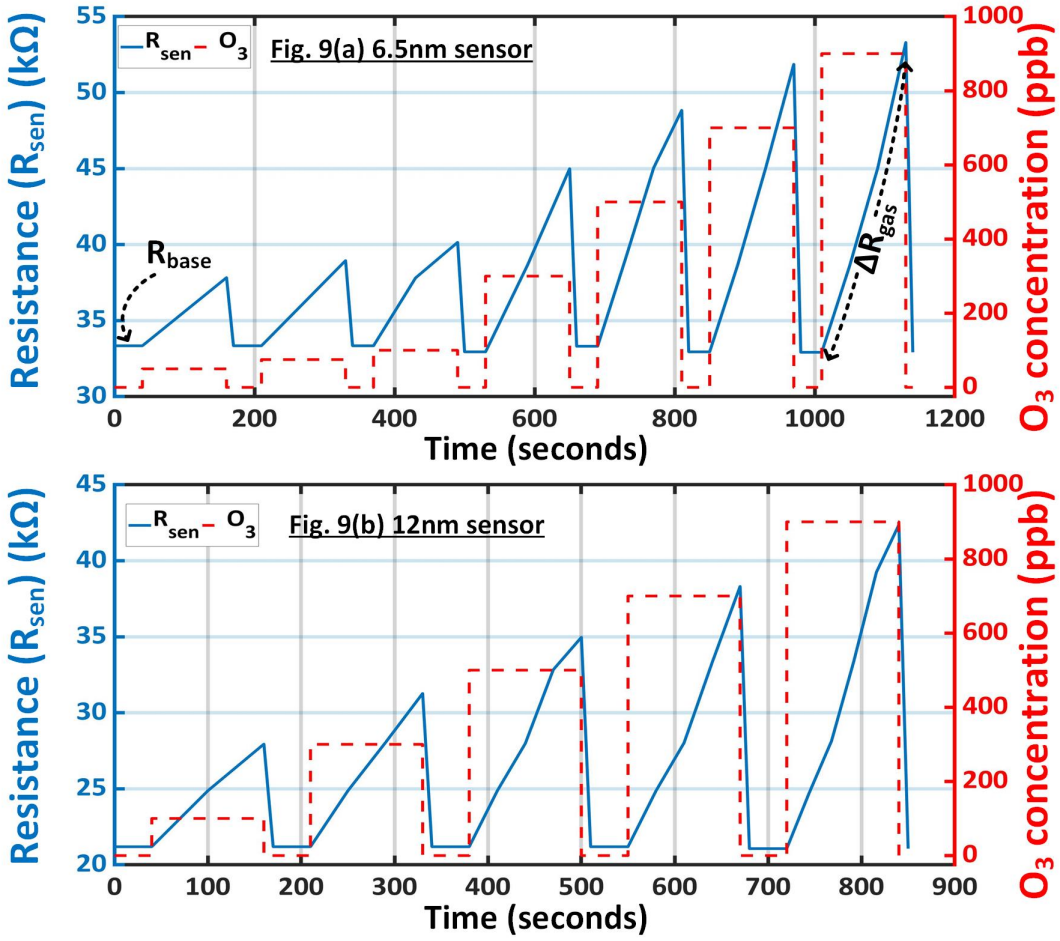

Figure 4.13: Measured resistance change (left) and corresponding O_3 concentration (right) observed by the sensor interface IC for O_3 sensors with thicknesses 6.5nm (a) and 12nm (b).

and 4.15(b) compare the dynamic range, resistance range and readout power of this work with other state-of-art gas sensing readouts, showing a 300X reduction in readout power. Here, dynamic range is calculated as a function of the largest measured resistance value and the noise floor, whereas resistance range is the absolute value of resistances that the readout can measure. The O_3 sensors used here show a drift within the range of 20 kΩto 1 MΩ, justifying that the resistance range this readout has been designed for, is sufficient. To the authors' knowledge, this is the lowest power consumption for a gas sensing readout, regardless of architecture, that

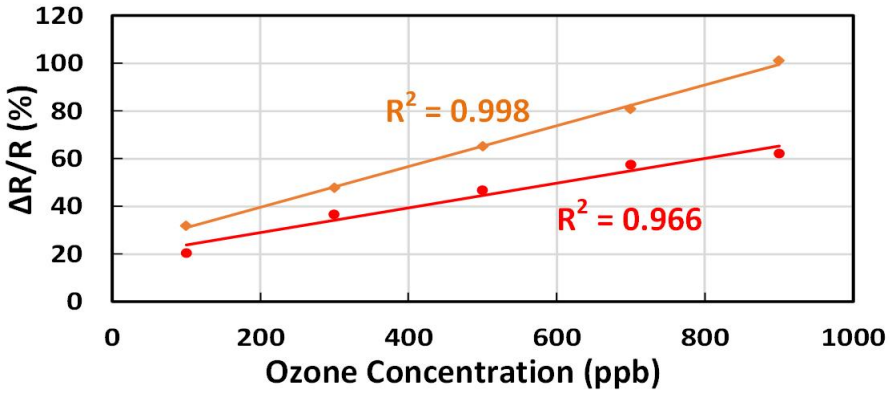

Figure 4.14: Measured sensitivity of the sensor interface IC when tested with O_3 sensors with thicknesses of 6.5 nm (diamond) and 12 nm (circle) across ozone concentrations from 100 ppb to 900 ppb. The R^2 values show the measured concentration linearity when tested with 6.5nm (orange) and 12 nm (red) sensors.

maintains a comparable dynamic range.

4.2.5 Conclusion

This part of the work presents a low-power sensor interface fabricated in a 65 nm bulk CMOS process that interfaces with custom MOX sensors to detect ozone concentrations varying from 50ppb to 900ppb. The sensor interface consumes 88.6nW of power while achieving a 159 dB dynamic range across a resistance range of 20 kOhm to 1 MOhm, and the system consumes a maximum of 1.09μW.

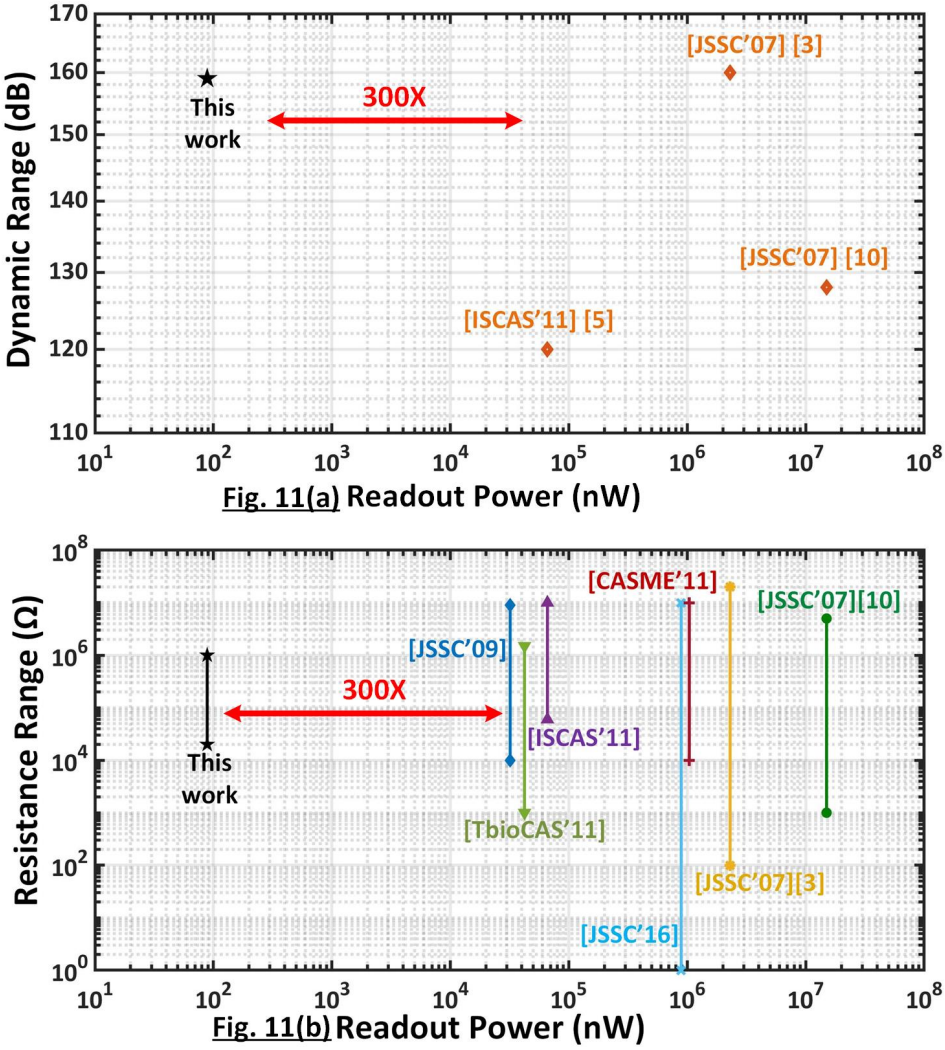

Figure 4.15: Comparison to the state of the art showing a 300x power reduction in sensor interfaces for gas sensing.

CHAPTER

FIVE

CONCLUSIONS AND FUTURE WORK

This chapter lists the key findings from this research and possible future directions to build an integrated energy efficient ALD E-Nose platform to sense both environment as well as breath biomarkers

5.1 Conclusions

5.1.1 Testing the power and sensitivity limits of ALD SnO_2 sensor

- Starting with a Debye length thickness of around 12 nm for SnO_2 sensor, baseline responses to Ozone and Acetone were evaluated from 25 ppb to 100 ppb and 50 pm to

300 ppm respectively.

- Thinner SnO_2 films, with thickness at two and twelve times lower than the Debye length i.e., at 6 nm and 4.5 nm were then deposited for improved sensitivity and to test the lowest achievable operating powers.
- Sensitivity improvements of atleast an order of magnitude with 6 nm and two orders of magnitude with 12 nm SnO2 sensor were seen with ozone.
- Without UV assisted recovery the highly sensitive SnO2 sensor could operate with power as low as 30 nW.

5.1.2 Building Blocks of E-Nose with ALD sensing layers

This part of research involved exploring all the available variables to improve sensitivity and variation in response as well as further lowering power budget for E-Nose operation.

- n-type SnO_2 and p-type CuO sensors were now deposited to build a cross-reactive ALD sensor array which can produce varying response to different analyte gases. PCA produced over 98% of variance with the just the first two components
- ALD SnO2 was deposited on substrates with different flexibility and surface area to explore its effect on sensitivity with nanocellulose substrate giving twice as much senstiivity with ozone before annealing.
- Composite sensors with SnO_2 -ZnO combinations were fabricated to create additional elements for E-Nose.

- Sensor deposition, anneal and operating temperatures, along with a varying molefraction, concentration of doped nano-particles were identified as additional variables to change the senstivity of the sensor elements.

5.1.3 Designing a novel monolithic sensor array

All commercially available sensor technologies suffer from drawbacks that limit their seamless implementation. Miniaturized form factors and high-volume production are essential to lower sensor costs. Towards this goal we designed a novel monolithic sensor array which would do away with integration of discrete sensors and creates different sensing surfaces using on-chip annealing techniques. The project was divided into a several modules aimed to be developed in parallel to cut-short on development time.

- Demonstrated the proof of concept of a novel approach to fabricate monolithically integrated single chip sensor array for high-volume manufacturing with SnO_2-ZnO composites with short anneal times
- 99.94% of variance accounted with first 3 components from PCA response of sensor array
- Novel microheater design was produced using COMSOL FEM simulations which targeted at producing a temperature difference between adjacent strips as much as 300°C.
- Power numbers as low as 6.3 mW for an operational temperature of 400°Cand a power of 1.58 mW for an operating temperature of 100°Ccould be reached. The average-power for 10% duty cycling at 400°Ccould reach as low as 630 μW.
- A MEMS microheater is being fabricated alongside in the group with a suspended heater bridge

- The sensors were optimized after the initial run by varying thickness and composition of Sn-Zn-O film to achieve high responsiveness at lower operation temperatures. Response with ozone in the 100°C-150°Cwere seen.

- Characterization of sensors was done with gas mixtures of acetone and ethanol, with a separation of over 75% of the mixture with the constituent gases could be seen. While the sensors in the current make-up have seen to not respond to toluene, formaldehyde or carbon monoxide.

- Finally to test a real-time use case scenario of alcohol and acetone, sensors were tested with exhaled human breath post-fasting and alcohol consumption, showing distinguishable response with normal reference breath.

5.1.4 System Integration

Integration of in-lab characterized sensors was done with HET testbed and with an adaptive current controlled AFE

- In-house fabricated SnO_2 sensors were wirebonded with an engineered system developed by Dr. Alper Bozkurt team at NCSU and was field tested at EPA labs at UNC Chapel Hill. The sensor with integrated UV operated with power under $150\mu W$ while the system itself operated in the mW range.

- SnO_2 sensors of different thicknesses were integrated with an adaptive current controlled AFE which operated at an ultra low system power 88.6 nW

5.2 Future Work

Short Term:

- In the short term the ALD sensing material could be deposited on Protochips' electro-thermal chips, which could then be used to wirebond to a system for automated testing and steady state tests
- Testing with mixtures of varying compositions could help to build a calibrated data sets for real-time sensing

Long Term:

- The system integration could be approached by combining with the adaptive current controlled AFE as mentioned in section 5.2 with it making a system consuming the lowest power (under 100 nW) and the E-Nose itself consuming a power of under 10 mW
- Expand testing with VOCs for other real-life use cases like gastro-intestinal diseases, cancer biomarkers
- First principles density functional theory (DFT) study to understand and categorize the mechanisms of metal oxides with gas-mixtures, which can help to understand and optimize sensors for a future targeted use-cases.

REFERENCES

[1] World Health Organization. *Ambient Air Pollution*. Available online:https://www.who.int/airpollution/ambient/pollutants/en/.

[2] Tao Wang et al. "Air quality during the 2008 Beijing Olympics: secondary pollutants and regional impact". In: *Atmospheric Chemistry and Physics* 10.16 (2010), pp. 7603–7615.

[3] Veronika Eyring et al. "Transport impacts on atmosphere and climate: Shipping". In: *Atmospheric Environment* 44.37 (2010), pp. 4735–4771.

[4] United States Environmental Protection Agency. *NAAQS Table*. Available online:https://www.epa.gov/criteria-air-pollutants/naaqs-table.

[5] Anthony J Guarascio et al. "The clinical and economic burden of chronic obstructive pulmonary disease in the USA". In: *ClinicoEconomics and outcomes research: CEOR* 5 (2013), p. 235.

[6] ID Kim et al. *Exhaled Breath Sensors. In Smart Sensors for Health and Environment Monitoring*. 2015.

[7] World Health Organization. *Diabetes Infographic*. Available online:http://www.who.int/diabetes/global-report/WHD2016_Diabetes_Infographic_v2.pdf.

[8] World Health Organization. *Diabetes*. Available online:http://www.who.int/mediacentre/factsheets/fs312/en/.

[9] ASSIST. *Vision and Mission*. Available online:https://assistcenter.org/about/.

[10] Jacek Ostrowski et al. "Mutagenesis of the beta2-adrenergic receptor: how structure elucidates function". In: *Annual review of pharmacology and toxicology* 32.1 (1992), pp. 167–183.

[11] Bettina Malnic et al. "Combinatorial receptor codes for odors". In: *Cell* 96.5 (1999), pp. 713–723.

[12] Keith J Albert et al. "Cross-reactive chemical sensor arrays". In: *Chemical reviews* 100.7 (2000), pp. 2595–2626.

[13] Sensigent. *Cyranose Electronic Nose*. Available online:http://www.sensigent.com/products/cyranose.html.

[14] NASA. *JPL ENose*. Available online:https://enose.jpl.nasa.gov/.

[15] Syeda Erfana Zohora, AM Khan, and Nisar Hundewale. “Chemical sensors employed in electronic noses: A review”. In: *Advances in computing and information technology* (2013), pp. 177–184.

[16] David James et al. “Chemical sensors for electronic nose systems”. In: *Microchimica Acta* 149.1-2 (2005), pp. 1–17.

[17] Steven Christopher Mills et al. “Ultra-low power room temperature metal oxide gas sensors: A study in sensitivity, selectivity and reliability”. In: (2017).

[18] Elisabetta Comini. “Integration of metal oxide nanowires in flexible gas sensing devices”. In: *Sensors* 13.8 (2013), pp. 10659–10673.

[19] David C Brock and Gordon E Moore. *Understanding Moore’s law: four decades of innovation*. Chemical Heritage Foundation, 2006.

[20] Zainab Yunusa et al. “Gas sensors: a review”. In: *Sensors and transducers* 168.4 (2014), pp. 61–75.

[21] Inkyu Park, Daejong Yang, and Kyungnam Kang. “MEMS/Nano-technologies for Smart Air Environmental Monitoring Sensors”. In: *Journal of Sensor Science and Technology* 24.5 (2015), pp. 281–286.

[22] Riikka L Puurunen. “Surface chemistry of atomic layer deposition: A case study for the trimethylaluminum/water process”. In: *Journal of applied physics* 97.12 (2005), p. 9.

[23] Chong-Min Kyung. *Smart sensors for health and environment monitoring*. Springer, 2015.

[24] Veena Misra et al. “Ultra-low power sensing platform for personal health and personal environmental monitoring”. In: *2015 IEEE International Electron Devices Meeting (IEDM)*. IEEE. 2015, pp. 13–1.

[25] Yu-Feng Sun et al. “Metal oxide nanostructures and their gas sensing properties: a review”. In: *Sensors* 12.3 (2012), pp. 2610–2631.

[26] Steven Mills et al. “Atomic layer deposition of SnO2 for selective room temperature low ppb level O3 sensing”. In: *ECS journal of solid state science and technology* 4.10 (2015), S3059.

[27] Michael Lim et al. “Application of AlGaN/GaN heterostructures for ultra-low power nitrogen dioxide sensing”. In: *ECS Journal of Solid State Science and Technology* 4.10 (2015), S3034.

[28] Hisahito Ogawa, Masahiro Nishikawa, and Atsushi Abe. “Hall measurement studies and an electrical conduction model of tin oxide ultrafine particle films”. In: *Journal of Applied Physics* 53.6 (1982), pp. 4448–4455.

[29] Elisabetta Comini. “Metal oxide nano-crystals for gas sensing”. In: *Analytica chimica acta* 568.1-2 (2006), pp. 28–40.

[30] Akhilesh Tanneeru et al. “Room temperature sensing of VOCs by atomic layer deposition of metal oxide”. In: *2016 IEEE SENSORS*. IEEE. 2016, pp. 1–3.

[31] Steven Mills, Bongmook Lee, and Veena Misra. “Room temperature ozone and humidity response evolution of atomic layer deposited SnO 2 sensors”. In: *2017 IEEE SENSORS*. IEEE. 2017, pp. 1–3.

[32] Chiu-Hsien Wu et al. “Fast gas concentration sensing by analyzing the rate of resistance change”. In: *Sensors and Actuators B: Chemical* 209 (2015), pp. 906–910.

[33] Lucy Chambers et al. “Effects of personal air pollution exposure on asthma symptoms, lung function and airway inflammation”. In: *Clinical & Experimental Allergy* 48.7 (2018), pp. 798–805.

[34] I Elmi et al. “Development of ultra-low-power consumption MOX sensors with ppb-level VOC detection capabilities for emerging applications”. In: *Sensors and Actuators B: Chemical* 135.1 (2008), pp. 342–351.

[35] Akhilesh Tanneeru et al. “Highly Sensitive ALD SnO2 Sensors and the Role of its Thickness in Gas Sensing Capabilities”. In: *2018 IEEE SENSORS*. IEEE. 2018, pp. 1–3.

[36] Akhilesh Tanneeru, Bongmook Lee, and Veena Misra. “Building Blocks of a New ALD E-Nose-A First Step: N-Type and P-Type ALD Sensors”. In: *2018 IEEE SENSORS*. IEEE. 2018, pp. 1–3.

[37] John R Balmes. “The role of ozone exposure in the epidemiology of asthma.” In: *Environmental health perspectives* 101.suppl 4 (1993), pp. 219–224.

[38] Taeg Sang Cho et al. “A 32-*mu* W 1.83-kS/s Carbon Nanotube Chemical Sensor System”. In: *IEEE Journal of Solid-State Circuits* 44.2 (2009), pp. 659–669.

[39] Marco Grassi, Piero Malcovati, and Andrea Baschirotto. “A 160 dB equivalent dynamic range auto-scaling interface for resistive gas sensors arrays”. In: *IEEE Journal of Solid-State Circuits* 42.3 (2007), pp. 518–528.

[40] Daniel J Rairigh et al. “CMOS baseline tracking and cancellation instrumentation for nanoparticle-coated chemiresistors”. In: *IEEE transactions on biomedical circuits and systems* 3.5 (2009), pp. 267–276.

[41] Xiaoyi Mu, Daniel Rairigh, and Andrew J Mason. “125ppm resolution and 120dB dynamic range nanoparticle chemiresistor array readout circuit”. In: *2011 IEEE International Symposium of Circuits and Systems (ISCAS)*. IEEE. 2011, pp. 2213–2216.

[42] John Allen. “Photoplethysmography and its application in clinical physiological measurement”. In: *Physiological measurement* 28.3 (2007), R1.

[43] Yu Sun and Nitish Thakor. “Photoplethysmography revisited: from contact to noncontact, from point to imaging”. In: *IEEE transactions on biomedical engineering* 63.3 (2015), pp. 463–477.

[44] Kil-sang Yoo and Won-Hyung Lee. “Mental stress assessment based on pulse photoplethysmography”. In: *2011 IEEE 15th International Symposium on Consumer Electronics (ISCE)*. IEEE. 2011, pp. 323–326.

[45] Empatica. *E4 wristband, Real-time physiological data streaming and visualization*. Available online:`https://www.empatica.com/e4-wristband/`.

[46] Elisabetta De Giovanni et al. “Ultra-low power estimation of heart rate under physical activity using a wearable photoplethysmographic system”. In: *2016 Euromicro Conference on Digital System Design (DSD)*. IEEE. 2016, pp. 553–560.

[47] Giulio Valenti and Klaas R Westerterp. “Optical heart rate monitoring module validation study”. In: *2013 IEEE International Conference on Consumer Electronics (ICCE)*. IEEE. 2013, pp. 195–196.

[48] Ernesto F Treo, Myriam C Herrera, and Max E Valentinuzzi. “Algorithm for identifying and separating beats from arterial pulse records”. In: *Biomedical engineering online* 4.1 (2005), pp. 1–9.

[49] TY Abay and PA Kyriacou. “Photoplethysmography for blood volumes and oxygenation changes during intermittent vascular occlusions”. In: *Journal of clinical monitoring and computing* 32.3 (2018), pp. 447–455.

[50] Diego Martın-Martınez et al. “Ppg beat reconstruction based on shape models and probabilistic templates for signals acquired with conventional smartphones”. In: *Iberian Conference on Pattern Recognition and Image Analysis*. Springer. 2015, pp. 595–602.

[51] Seyed Salehizadeh et al. “A novel time-varying spectral filtering algorithm for reconstruction of motion artifact corrupted heart rate signals during intense physical activities using a wearable photoplethysmogram sensor”. In: *Sensors* 16.1 (2016), p. 10.

[52] Martin Gjoreski et al. “Monitoring stress with a wrist device using context”. In: *Journal of biomedical informatics* 73 (2017), pp. 159–170.

[53] U.S. Bureau of Economic Analysis. *Gross Domestic Product | Fourth Quarter and Annual 2018 (Initial Estimate)*. Available online:https://www.bea.gov/news/2019/initial-gross-domestic-product-4th-quarter-and-annual-2018.

[54] Center of Medicare and Medicaid Services. *NHE-Fact-Sheet*. Available online:https://www.cms.gov/research-statistics-data-and-systems/statistics-trends-and-reports/nationalhealthexpenddata/nhe-fact-sheet.html.

[55] Medical Technology Industry Spotlight. Available online:https://www.selectusa.gov/medical-technology-industry-united-states.

[56] Centers for Disease Control and Prevention. *Heart Disease Fact Sheet*. Available online:https://www.cdc.gov/dhdsp/data_statistics/fact_sheets/fs_heart_disease.html.

[57] Majd AlGhatrif and Joseph Lindsay. "A brief review: history to understand fundamentals of electrocardiography". In: *Journal of community hospital internal medicine perspectives* 2.1 (2012), p. 14383.

[58] Riyo Ogura et al. "Specific Findings of the Standard 12-Lead ECG in Patients WithTakotsubo'Cardiomyopathy Comparison With the Findings of Acute Anterior Myocardial Infarction". In: *Circulation journal* 67.8 (2003), pp. 687–690.

[59] P Klootwijk et al. "Comparison of usefulness of computer assisted continuous 48-h 3-lead with 12-lead ECG ischaemia monitoring for detection and quantitation of ischaemia in patients with unstable angina". In: *European heart journal* 18.6 (1997), pp. 931–940.

[60] George B Moody and Roger G Mark. "Development and evaluation of a 2-lead ECG analysis program". In: *Computers in cardiology* 9 (1982), pp. 39–44.

[61] Emmanuel Skordalakis. "Syntactic ECG processing: A review". In: *Pattern recognition* 19.4 (1986), pp. 305–313.

[62] Peter Sam Raj and Dimitrios Hatzinakos. "Feasibility of single-arm single-lead ECG biometrics". In: *2014 22nd European Signal Processing Conference (EUSIPCO)*. IEEE. 2014, pp. 2525–2529.

[63] Angel Villegas, David McEneaney, and Omar Escalona. "Arm-ECG wireless sensor system for wearable long-term surveillance of heart arrhythmias". In: *Electronics* 8.11 (2019), p. 1300.

APPENDICES

APPENDIX

A

ESTIMATION OF BEAT-TO-BEAT INTERVAL FROM WEARABLE PHOTOPLETHYSMOGRAPHY SENSOR ON DIFFERENT MEASUREMENT SITES DURING DAILY ACTIVITIES

The material in Appendix-A originally appeared as Akbulut FP, Lawless K, Tanneeru A, Rao S, Lee B, Misra V. Estimation of Beat-to-Beat Interval from Wearable Photoplethysmography Sensor on Different Measurement Sites During Daily Activities. In2018 IEEE SENSORS 2018 Oct 28 (pp. 1-4). IEEE.

In this study, we present an algorithm to detect beat-to-beat interval from PPG in the presence of motion artifacts. Our approach includes splitting slowly varying DC components, statistical

detrending, and Bessel filtering and Fast Fourier Transform with square window to reduce motion artifacts dependent on spectrum analysis. The algorithm segments beat intervals with a spectrogram to find the characteristic points of the waveform such as systolic and diastolic points. Interbeat intervals (IBI) are determined from these characteristic points to calculate heart rate. The PPG IBI algorithm is validated against ECG RR intervals from five different measurement sites during three daily activities. The results show that the most accurate IBI and HR detection from a wearable PPG device during regular user activity is from the upper arm or finger.

A.1 Introduction

Photoplethysmography (PPG) is a noninvasive method of assessing the human cardiovascular system using optical technology at the skin's surface. When an illumination source is applied to the tissue, fluctuations in intensity of reflected or transmitted light can be measured that result from blood volume changes in the microvascular bed of tissue [42]. The captured response is the PPG waveform which consists of a slowly varying baseline DC component and a pulsating AC component corresponding to heartbeats; both can be analyzed to reveal information about a wide variety of physiological parameters, including heart rate (HR), blood oxygen saturation, blood pressure, respiration, and sympathetic nervous system activities [43].

In addition to analysis of PPG for HR detection, this study gives particular interest to the application of PPG for measurement of the variation of interbeat interval (IBI), called pulse rate variability (PRV) for PPG, as an analog of heart rate variability (HRV) commonly obtained by electrocardiography (ECG). Both PRV and HRV are indicatives of several autonomic nervous system (ANS) activities, notably emotional arousal and stress [44].

In our study, we used the commercially available Empatica E4 wristband [45] to collect PPG data. Using the integrated PPG sensor, the E4 is capable of determining multiple parameters, including HR and IBI. The E4 is a wrist-worn device and includes a motion artifact removal algorithm, but a large variation from user to user was reported [46][47].

In this paper, we propose an automated algorithm for extracting HR and beat-to-beat interval from PPG signals with motion artifacts present. Even a poor-quality signal with motion artifacts present can yield a limited amount of valuable information after analysis - such as HR and PRV - given a robust detection algorithm is employed. The main contributions of this paper can be summarized as follows:

A beat-to-beat interval detection algorithm was developed which is accurate for PPG signals collected from different locations of the body, compared with ECG signal measured from chest to validate with the RR intervals the point- to- point and average interbeat intervals of PPG. Since wearable sensors are mostly known to be used while on the move, our algorithm is designed for reducing motion artifacts and analyzing the characteristic points in order to improve the measurement quality.

For wearable system manufacturers, the highest accuracy of the sensors is achieved by operating the system on the ideal location on the body. For this reason, determining the measurement site is one of the most critical architectural decisions. Within the scope of this research, the most ideal places for positioning wearable systems were investigated.

A.2 Method

This study aims to develop an beat-to-beat interval detection algorithm called b2bINT for PPG in common wearable system. PPG signals were measured through an Empatica E4 wearable device [45]. The algorithm for interval segmentation and finding of local minima points that we propose is based on work by Treo et al. [48]. The PPG signal tends to be nonstationary and carries slowly varying DC content along with the AC content [49]. So, as a first step, it is segmented into fixed length to extract the stationary part.

To remove baseline wander such as depth breath and movement, statistical detrending [50] is used by removing the mean and the variance trends as follows;

$$x_d(t) = \frac{x(t) - n_x(t)}{\sigma_x^2(t)} \tag{1}$$

where x(t) and xd(t) are the input and detrended output signals, respectively, and $n_x(t)$ and $\sigma_x^2(t)$ are the mean and variance at time t estimated over a 30 second window.

Since the PPG signal is primarily produced by the heart rhythm, it is presumed that its spectral content will be predominantly found in the range from 0.5 Hz-3 Hz [51]. For this reason, we limit the range to 0.6 Hz-2.9 Hz and take the power and frequency information of the first three peaks in the power spectral density (PSD) at each window. Then, we select the characteristic point that is higher than the highest peak of the spectrum divided by a specified cut-off factor to estimate the interval.

The PPG signal is differentiated twice by applying iterative series of subtractions, that is,

$$x'(t) = x(t+1) - x(t) \tag{2}$$

$$x''(t) = x''(t+1) - x'(t) \tag{3}$$

Determination of IBI was made by analyzing points of interest (Fig. A.1) in three subsets derived from the noisy PPG signal, x(t). The first subset comprises the first characteristic point is the systolic point present for every pulse in the maximum of PPG. The second subset is the local maxima points of the first derivative, x'(t), which is located near the 50% point on the ascending slope before the systolic peak.

The first derivative initially identifies all local maxima, both small and large ones; so, filtering is required to remove the small spikes and preserve the large peaks. Then, the second derivative x"(t) is found with maxima which also correspond to diastolic points, creating a third subset. We use that result to obtain sets of two successive local minima points. The difference between the two successive minima points is found and if the value does not exceed the given threshold then second minima points are removed.

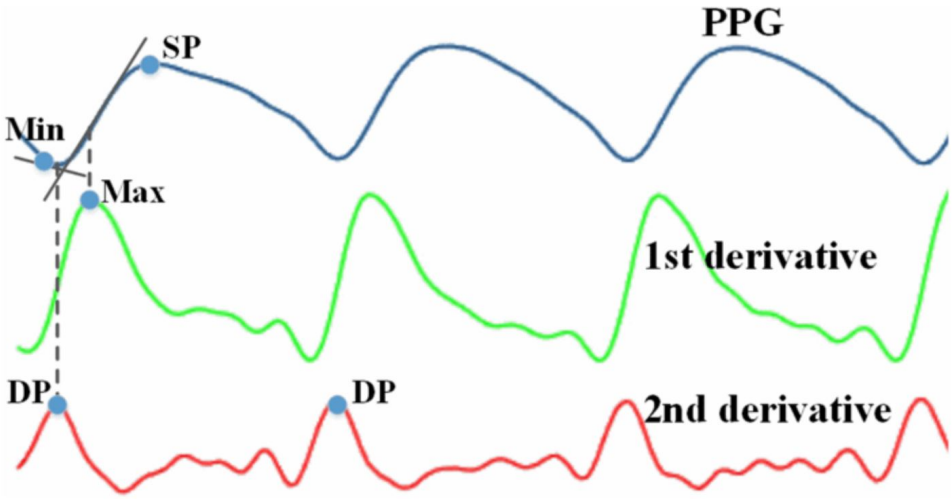

Figure A.1: Characteristic points of PPG with 1st and 2nd derivatives, showing typical time-points of systolic points (sp) at maxima of PPG, maxima of 1st derivative, and diastolic points (dp) at minima of PPG and maxima of 2nd derivative

After obtaining location of maxima peaks, the corresponding heart rate (ρ_t) is calculated. If ρ_t is inside a determined range of the calculated heart rate acquired in the prior time window ($\rho_t - 1$) then a next peak selected, for finding frequency and location of the prior time window $\omega(t-1)$ are utilized and a search area $S_a = [\omega(t-1) - \Delta s, ..., \omega(t-1) + \Delta s]$, that is $\pm\Delta s$ frequencies inside the around of the reference $\omega(t-1)$ is applied. The location of the peak in x_{DP} is selected from that search area ($x_{DP} \in S_a$) and then the heart rate in BPM is calculated as

$$\rho_t = \frac{f_s \times L_{x_{DP}}}{N} \times 60 \tag{4}$$

where N is the total number of points, L is the number of peaks, and fs is the sampling

frequency. After that, if heart rate within the expected region, the peak is located in estimated PP.

We compared our results with the Empatica E4 that provides heartbeats extracted from the PPG data which contain the location of detected peaks and time intervals between peaks recorded as a tuple [45]. However, continuous data for IBI in high-movement periods [52] are not provided causing error in the number of intervals for the detected IBI using frequency analysis and the quality of the spectrum used for the frequency analysis. This is only useful if average heart rate is needed, but is not appropriate for looking at variations in heart rate.

The b2bINT algorithm does not correlate the PPG data with any certain frequencies that may correspond to regular body movements, which is often done in conjunction with accelerometer measurements in wearable systems to detect motion artifacts. This study shows the accuracy of this algorithm without increasing the complexity of hardware or software by including these.

A.3 Results

We collected PPG data from five different body sites (Fig. A.2) including the finger, wrist, upper arm, ankle, and behind the ear, using the Empatica E4 wristband to determine the accuracy and functionality of the proposed b2bINT detection algorithm. Raw PPG measurements were captured at the different sites on the body with the Empatica E4 wristband and processed for IBI and HR with the proposed algorithm. Simultaneously, the wearable 3-lead ECG measurement system developed by NCSU ASSIST Center was used to compare PPG performance against ECG.

The PPG data was collected within two-and-a-half minutes durations at fs=64Hz. The

performance of the proposed algorithm was evaluated during three different activities; resting, walking, and speaking. During these three activities, five readings were recorded for each discrete body location (5 locations x 3 activities x 5 repeat = 75 records). When we compared the measurements made in these five different locations, we found that the measurements made at the wrist and upper arm were slightly more accurate than the other sites.

We compared the results of our proposed algorithm with the results determined by Empatica E4 platform. The number of IBIs determined from Empaticas algorithm was 34% lower on average as compared to the number of IBIs by the reference ECG system. Comparatively, the average IBI error determined by our proposed algorithm was only 9%, an acceptable value for wearable sensors in systems not used for diagnostic purposes. Table A.1 depicts that our proposed model gives better accuracy in terms of IBI error when compared with the processing done by the Empatica E4 wristband.

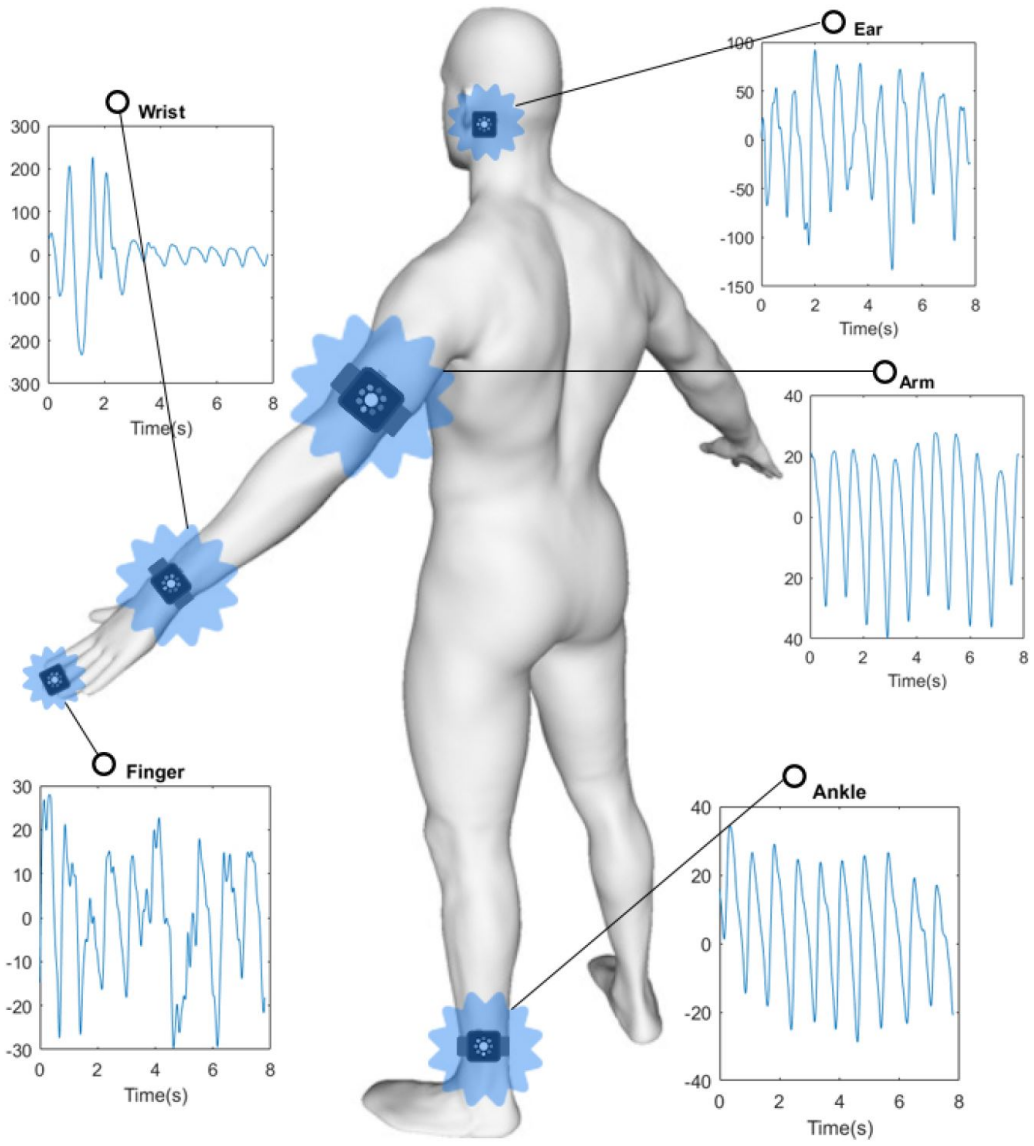

Figure A.2: Measurement site of PPG signal on human body (measured in resting position)

In order to confirm the calculated interbeat intervals using the proposed algorithm from the PPG, we compared them with the RR intervals of the ECG measurements. With reference to the highly accurate ECG measurements, which had an average RR interval count of 199 and HR of 79.9 BPM, the validity of the proposed method and the accuracy of the measurement site was

Table A.1: Means and standard deviations of proposed beat-to-beat interval algorithm (b2bint) and empatica's (emp.). hr in bpm and ibi counts (rest position) where fs=64Hz

	b2bINT HR	b2bINT IBI	Emp. HR	Emp. IBI
Wrist	78.4 ±1.9	189 ±0.6	65.5 ±0.12	150 ±0.23
Finger	77.5 ±1.3	170 ±1.6	40.80 ±5.3	90 ±17.6
Behind ear	78.98 ±0.9	180 ±1.01	52.4 ±0.32	120 ±0.24
Upper arm	79.5 ±0.56	182 ±0.21	65.5 ±0.2	150 ±0.23
Ankle	74.8 ±1.34	177 ±0.41	65.5 ±0.36	150 ±0.3

demonstrated. The readings given by b2bINT, evaluated against the ECG measurements, show that the proposed system gives a stable response at nearly all tested points on the body.

Table A.2 shows the accuracy of the metrics computed by Empatica E4 wristband compared with the proposed algorithm and the reference ECG. Based on this, the proposed system seems to have a higher degree of accuracy in all activities. In particular, the mean square error (MSE) of measurements made during resting and speaking is better than the average value of measurements made during walking. The measurements of the Empatica remain very inaccurate, especially during the walking activity. The error for the other two activities is also nearly twice that of the algorithm we recommend. The measurements made for the three activities show that the upper arm is the site where the PPG sensor works with the highest accuracy. Considering a typical use case for a wearable device when multiple activities are performed, the alternative place is the finger.

The overall MSE of the proposed algorithm for resting, walking, and speaking are 0.14±0.01 ms, 0.192±0.25 ms, 0.17±0.01 ms respectively. The overall MSE of Empatica's algorithm results are 0.41±0.03 ms, 0.83±0.65 ms, 0.51±0.16 ms. In all these results, it is seen that we developed a method which operates with high accuracy independent of motion artifacts introduced by physical activity.

Table A.2: Proposed algorithm (b2bint) and empatica's (emp.) means and standard deviations of mse between ecg and ppg

	Resting $\mu \pm \sigma$ ms		Walking $\mu \pm \sigma$ ms		Speaking $\mu \pm \sigma$ ms	
	b2bINT	**Emp.**	**b2bINT**	**Emp.**	**b2bINT**	**Emp.**
S1	0.1481 ± 0.008	0.3105 ± 0.006	0.1931 ±0.3	0.9167 ±0.82	0.1415 ±0.02	0.3429 ±0.041
S2	**0.1223 ± 0.017**	0.6444 ± 0.12	**0.1428 ±0.26**	0.6435 ±0.61	0.2427 ±0.028	0.8536 ±0.36
S3	0.1356 ± 0.007	0.4214 ± 0.009	0.1972 ±0.21	0.8018 ±0.56	0.1635 ±0.026	0.4858 ±0.14
S4	**0.1256 ± 0.007**	0.3431 ± 0.009	0.1928 ±0.22	0.8135 ±0.6	**0.1344 ±0.008**	0.3448 ±0.256
S5	0.1574 ± 0.01	0.3205 ± 0.026	0.2172 ±0.3	0.9718 ±0.7	0.1464 ±0.002	0.5367 ±0.003

Measurement Site: S1-Wrist, S2-Finger, S3-Behind the ear, S4-Upper Arm, S5-Ankle.

A.4 Conclusion

Our proposed b2bINT algorithm can effectively reduce slowly-varying periodic motion artifacts from PPG waveforms that are measured during different site activities. The validity of the proposed algorithm is evaluated by comparing the results obtained by the algorithm of the commercial device that has been used to capture the PPG data. The average MSE using b2bINT method from the three different daily activities of resting, speaking and walking are 0.14, 0.16 and 0.19 respectively. The measured values of resting and speaking activities are close to each other and MSE is slightly increased in walking-based scenarios. In terms of the measurement sites, we observed that the ideal locations for a PPG-based wearable system are the arm and the finger.

APPENDIX

B

MEASUREMENT OF ECG SIGNAL FROM LEFT-ARM

Mohaddes F, da Silva RL, Akbulut FP, Zhou Y, Tanneeru A, Lobaton E, Lee B, Misra V. A Pipeline for Adaptive Filtering and Transformation of Noisy Left-Arm ECG to Its Surrogate Chest Signal. Electronics. 2020 May;9(5):866.

B.1 Introduction

U.S. national health expenditure accounts for 17.9% of the GDP with a projected annual growth of 5.5% per year between 2018 and 2027, reaching $6.0 trillion by 2027 [53][54]. Only in 2017, the share of the U.S. medical devices market was $156 billion, accounting for 40% of the global market [55]. The main reason for this boom is the high demand for portable, affordable,

and IoT-compatible health monitoring devices capable of preventing the U.S. number one killer, cardiovascular diseases [56]. Electrocardiogram (ECG) is a reliable reference for the evaluation of cardiac activity and has been adopted by the health industry as a standard method since 1954 [57]. Common types of ECG include 12-lead [58], 3-lead [59], 2-lead [60], and single-lead systems. Due to the close vicinity to the heart, the chest is the most conventional location for ECG evaluations, enabling ECG mapping with high precision and signal-to-noise ratio (SNR) [61]. However, conventional one-off chest-ECG (C-ECG) tests are cumbersome, costly, interrupted, and non-user friendly, making it an unattractive option for both intermittent and continual cardiac monitoring. Located in the proximity to the heart, left arm is a good candidate for ECG measurements, providing further comfort for continual cardiac monitoring compared to chest-wearable devices. However, there is little information on left-arm ECG (LA-ECG) characteristics, which may be due to its lower SNR compared to the chest and its higher vulnerability to different ambient noises [62]. Villegas et al. [63] managed to obtain a high-quality ECG from the arm, employing both analog and digital filtering, which, along with the used front-end amplification (AFE) resulted in a clear ECG with its major waves.

B.2 Hardware

The multi-sensor system was entirely developed with commercial off-the-shelf (COTS) components and a custom printed circuit board (PCB) design. The hardware provides signal acquisition of integrated sensors on the body including ECG, electro-dermal activity (EDA), and photoplethysmography (PPG). The microcontroller interfaces with an external 16-bit analog-to-digital converter (ADC), which samples the ECG signal. An AD8232 specialized analog frontend was chosen for ECG readings due to its capability of providing high gain (1000), high output impedance (10 GΩ), and filter customization. The AD8232 has two input electrodes (RA and

LA) and a driven electrode that senses the common mode noise at the inputs and attempts to cancel it by injecting the signal back into the user. To reduce motion artifacts, a narrow band-pass characteristic is required to separate the heart signal from the interferers. Therefore, the customized filter network for the ECG frontend is implemented such that a two-pole low-pass filter and a two-pole high-pass filter are set to 27 Hz and 7 Hz, respectively. The analog output of the AD8232 is connected to an ADC (ADS1114). The ADS114 chip is a 16-bit ADC to sample the analog signal and feed it into a Nordic NRF51822 microcontroller via inter-integrated circuit (I2C) communication. The internal ADC in the microcontroller samples an analog signal from electro-dermal activity sensing. The microcontroller unit (MCU, Nordic nRF51822, Nordic Semiconductor, Trondheim, Norway) incorporates an ARM Cortex M0 (ARM Developer, Cambridge, UK) with 32 KB of RAM, 256 KB of non-volatile flash memory, and an internal ADC. The unit also has an integrated BLE radio. In order to increase the antenna performance and the BLE range, a Raytac MDBT40 carrier board comprising a microcontroller, antenna, balun, and high-frequency crystal was used. The nRF51822 (Nordic Semiconductor, Trondheim, Norway) has flexible General Purpose Input/Output (GPIO) ports that support communication protocols including I2C, Synchronous Peripheral Interface (SPI), and Universal Asynchronous Receiver/Transmitter (UART). An ADXL345 accelerometer is interfaced over SPI to the nRF51822. The ADXL345 (Analog Devices, Norwood, MA, USA) is an ultra-low-powered tri-axial accelerometer with 13-bit resolution and supports measurement ranges up to ±16 g. In order to store the sensor data for continuous measurement, a high-volume external flash memory (128 Mb) was also implemented. The Winbond W25Q128 SpiFlash series (Winbond, Taichung City, Taiwan) is also communicated through SPI to the MCU. The entire system is powered with a 3.3 V supply regulated from a battery. A JST-type connector is used for connecting to a typical lithium polymer battery. The Microchip MCP73831 (Microchip Technology, Chandler, AZ, USA) charge management controller is implemented for charging the battery via microUSB. The TI TLV710 dual-voltage low-dropout (LDO) regulator (Texas

Instruments, Dallas, TX, USA) is used to provide both 3.3 V and 1.8 V supplies. The final footprint of the design is 1.0" x 1.5". The images of the developed armband, the system hardware, and the positions of the electrodes LA (+), RA (-) , and ground that resulted in the closest match to the C-ECG obtained from an ISO1001-certified BIOPAC MP160 benchtop system are shown in Fig. B.1

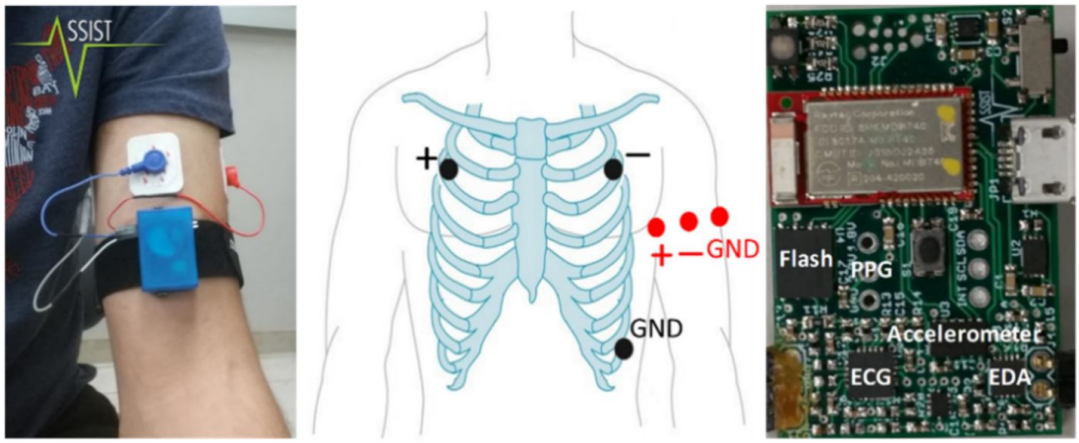

Figure B.1: ECG armband (left); arm and chest electrode positions (middle); system hardware (right).

Fig. B.2 shows a block diagram of our wearable system with data transmission. The ECG signal can be transmitted through a wire to the computer or through a BLE communication, as seen in Fig. B.2. Minimal power consumption is expected with serial communication between the wearable device and a computer with the BLE off, and the flash has become inaccessible. The total power consumption for this case is calculated to be 3 mW. The system can also be used for wireless transmission through BLE. When the continuous BLE mode is engaged, the total power consumption is to be 57 mW. For extended measurement, on-chip storing of the data is required while the BLE is off. For this scenario, the maximum power consumption is about 70 mW. It should be noted that these power consumptions can be greatly reduced with data compression

and optimization of data transmission time. The 150 mAh, 3.7 V lithium-ion polymer battery cell used in this can run the ECG module of the armband system for 7 h continuously.

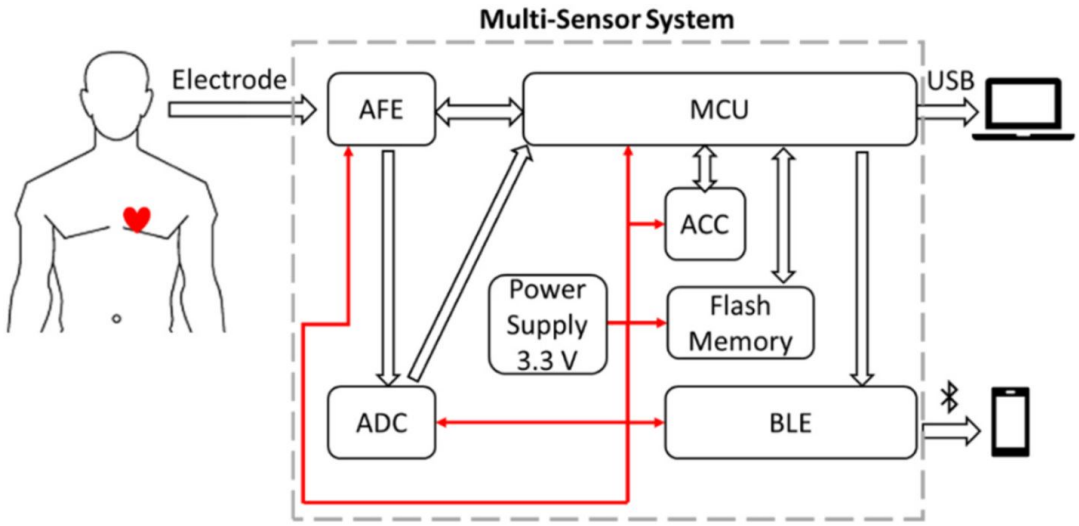

Figure B.2: Block diagram of the biometric armband.

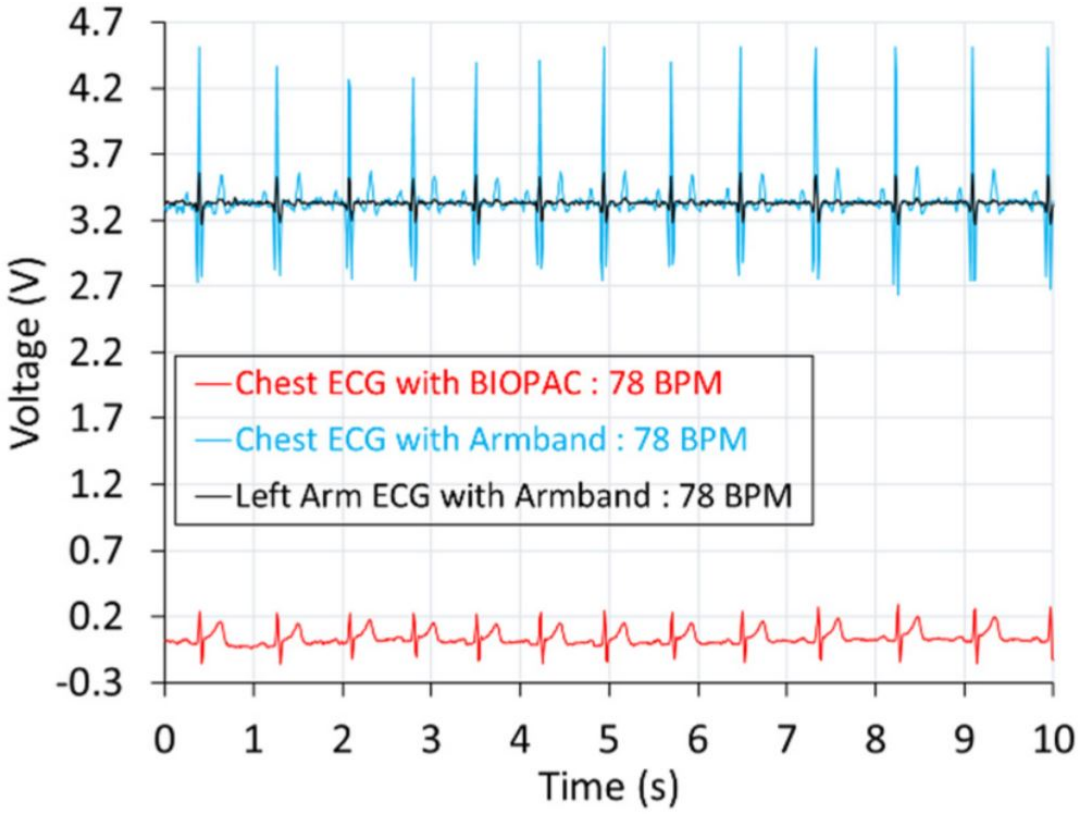

Figure B.3: ECG signals simultaneously obtained from the chest and left arm.

B.3 ECG Data Acquisitions and Conclusions

The accuracy of the armband LA-ECG and C-ECG signals was tested against the C-ECG signals obtained by a bench-top MP160 BIOPAC system at the same sampling frequency (100 Hz) and in real-time. As shown in Fig. B.3, both the position of the PQRST complex and the heart rate (65 bpm) of the ECG signals collected by the armband systems matched those of the BIOPAC system. Though the amplitude of the signal obtained from the left-arm signal is lower, a good quaility signal that preserves the actual waveform could be noise filtered and amplified. ECG data collected from an arm can be a convenient way to continuously gather real-time accurate

physiological data and correlate it eventually to the mild to acute psychological/environmental stress across all age groups.